Title	The structural and functional properties of the human visual pathway
Author(s)	大石, 浩輝
Citation	大阪大学, 2021, 博士論文
Version Type	VoR
URL	https://doi.org/10.18910/82340
rights	
Note	

The structural and functional properties of the human visual pathway

(ヒト視覚系の機能と構造)

A DOCTORAL DISSERTATION
SUBMITTED TO THE GRADUATE SCHOOL
OF FRONTIER BIOSCIENCES OF OSAKA UNIVERSITY

Hiroki Oishi

March, 2021

Abstract

Our visual perception is based on the process in the visual pathway. For the last decades, many neuroimaging studies using functional magnetic resonance imaging (fMRI) have elucidated the functional organization of the human visual pathway and its relationship to visual perception. Because the anatomical structure of the human visual pathway has been mostly studied in the postmortem human brain, little is known about how the anatomical structure relates to functional organization and visual perception. The reason is it is only recently that the non-invasive quantitative structure imaging of living human brains has become available.

This dissertation includes two studies, which quantified the structure of the human visual pathway, primarily using a macromolecular tissue volume (MTV) mapping. MTV is a recently proposed quantitative structural MRI method, which is sensitive to a fraction of non-water macromolecules.

In the first study, I attempted to non-invasively identify subdivisions of the lateral geniculate nucleus (LGN), a key thalamic nucleus that receives projections from retinal neurons and in turn projects to the cortex. The LGN is composed of two main subdivisions, magnocellular and parvocellular subdivisions. The non-invasive identification of these subdivisions has been difficult because the in vivo structural neuroimaging method for quantifying the properties of LGN subdivisions has not yet been established. Here, I measured MTV in the living human brain and found the gradual MTV changes within LGN, which enabled us to identify the LGN subdivisions. An fMRI experiment further revealed that the subdivisions showed different sensitivities to visual stimuli. This study provides a novel method for non-invasively investigating the structural properties of LGN subdivisions in living human brains, which can be combined with functional or behavioral experiments.

In the second study, I investigated the neuroanatomical basis of individual differences in stereopsis, one of the fundamental visual functions. There are huge inter-individual differences in the ability to discriminate depth from binocular disparity (stereoacuity). Here, I investigated the neuroanatomical basis of the inter-individual differences in stereoacuity. Based on the previous studies showing that several areas in both dorsal and ventral visual pathways are involved in stereopsis, I hypothesized that the white matter tract connecting those areas is the crucial anatomical substrate for stereopsis. I investigated how the human stereoacuity relates to white matter properties by combining psychophysics, diffusion MRI and MTV. As a result, I found that the MTV along the right vertical occipital fasciculus (VOF), a major tract connecting dorsal and ventral visual areas, was highly correlated with stereoacuity. By fMRI experiment, I further found that binocular disparity stimuli activated the

dorsal and ventral visual regions near VOF endpoints. These results suggest that stereo perception is associated with dorso-ventral communication through the VOF.

These two studies have provided an important foundation for future studies that investigate the relationship between perception, function and structure in the human visual pathway.

Table of Contents

Chapter 3.
Structural properties of the vertical occipital fasciculus correlates with the variability in human stereoacuity. 58

Chapter 4.
General discussion and conclusion 87

Chapter 1.

General introduction about human visual pathway and brain imaging

How the brain produces perception in humans is a fundamental question of cognitive neuroscience. Vision and neuroscience studies have extensively studied the relationship between visual perception and activity in brain areas, resulting in elucidating the neural circuits which contribute to the visual perception, which is called visual pathway (Livingstone and Hubel, 1988). In humans, functional magnetic resonance imaging (fMRI) have elucidated the functional organization of the human visual pathway, including retinotopic organization (Wandell et al., 2007; Dumoulin and Wandell, 2008; Amano et al., 2009). Human fMRI studies also clarified the perceptually correlated brain activity in the visual pathway (Heeger, 1999; Haynes et al., 2005; Preston et al., 2008).

While the relationship between function and perception has been extensively studied over the past decades, it should be remembered that the visual pathway is the anatomical architecture made up of neural tissue. Little is known about the anatomical relationship to function and perception in the human visual pathways, though these investigations are important to unravelling the organization principle of the human visual pathway. Also, the investigation of the relationship between the visual perception and structural properties gives a promising clue to understand the relationship between mind and matter in humans, which has been debated throughout history (e.g. dualism v.s. monism) (Zalta et al., 1995).

Previous studies have attempted to investigate the anatomy of the human visual pathway and test the relationship between visual perception and structural properties of the human visual pathway by using different approaches. Anatomical inspection studies on postmortem human brains have elucidated the structural organization of the human visual pathway (De Moraes, 2013; Amunts and Zilles, 2015), but this approach cannot test the relationship to visual perception because of using postmortem brain. Visual experiments on living humans with lesions of visual pathways have provided a rough insight into the relationship between visual perception and approximate brain regions (Goodale et al., 1991; Goodale and Milner, 1992), but structural imaging of living human brains is necessary to test the relationship between structural properties and subject perceptions. In around 2000, two structural property measurements for living humans were developed. The voxel based morphometry (VBM) can measure the volume of brain areas (Ashburner and Friston, 2000). The cortical thickness literally measures the thickness of brain areas in gray matter (Fischl and Dale, 2000). These two measures have been used to test the structural relationship to visual perception (Kanai and Rees, 2011) but they have limitations about quantitativeness. For example, defining the boundary of the gray and white matter is crucial to assess the cortical thickness, but it depends on how clear the boundary is. Thus, the segmentation quality is affected by the resolution of the imaging. For the limitation of these approaches, it has been difficult to quantitatively test the relationship between visual perception and the structural properties of the human visual pathway.

Recently, Mezer and colleagues developed a non-invasive quantitative structural imaging method (Mezer et al., 2013). The measure, macromolecular tissue volume (MTV) quantifies the neural tissue density of the brain in a resolution of 1 mm^3. Although cortical thickness can be used only for the measure of gray matter, the MTV can be applied to any brain areas, including gray and white matter. This measure has been used to detect the diseases-related structural degenerations (e.g. multiple sclerosis (Mezer et al., 2013) and Leber's hereditary optic neuropathy, which is a kind of eye disease (Takemura et al., 2019)). Here I measured the MTV in the living human brain and attempted to quantify the structure of the areas in the visual pathway of living humans and test the relationship between a visual perception and structural properties of the human visual pathway.

In my dissertation I addressed two main questions:

1. Is it possible to noninvasively mapping the areas of the human visual pathway in a sub-divisional scale? How different the structure and function are between the identified subdivisions? In the first study (Chapter 2), I attempted to identify subdivisions in the lateral geniculate nucleus (LGN) in living humans by testing the microstructural difference, primarily using MTV. LGN is an area which has been well studied in non-human primates, while not much in humans. I further tested the functional difference between the LGN subdivisions using fMRI with visual stimuli, which have complementary visual features.

2. Are there any neural bases for the individual variability of the stereoacuity? The stereoacuity is defined as the smallest detectable step of binocular disparity. There are huge inter-individual differences in human stereoacuity. In the second study (Chapter 3), I attempted to identify its neural basis by investigating the correlation between the stereoacuity and the structural properties of the human visual pathways, using a psychophysiological measurement, diffusion MRI and MTV.

In the rest of the introduction, I give a broad overview of backgrounds and methods of the first and second studies of this dissertation. This overview includes (1) the visual pathway and (2) the neuroimaging methods and analyses for investigating the human visual pathway. I end this dissertation with a general discussion and conclusion across the two studies as well as future directions.

1.1 Visual pathway

The visual pathway can be broadly divided into two stages. One is the geniculo-cortical pathway, which runs from the retina via the lateral geniculate nucleus (LGN) to the primary visual cortex (V1). The next one is the cortical pathway, which runs from occipital visual areas including V1 to the anterior cortical areas. These pathways have two main features of processing. The one is a parallel stream processing (Fig. 1.1.1). Different and complementary aspects of visual information are processed in the parallel streams in both geniculo-cortical and cortical pathways. The other one is a hierarchical processing. Higher areas receive multiple inputs of neurons in the lower areas and integrate the inputted visual information. In this section, I describe the findings of the anatomy and function of the visual pathway in humans as well as non-human primates. The subsections, “Geniculo-cortical pathway” and “Cortical pathway” are the backgrounds of the first and second studies, respectively.

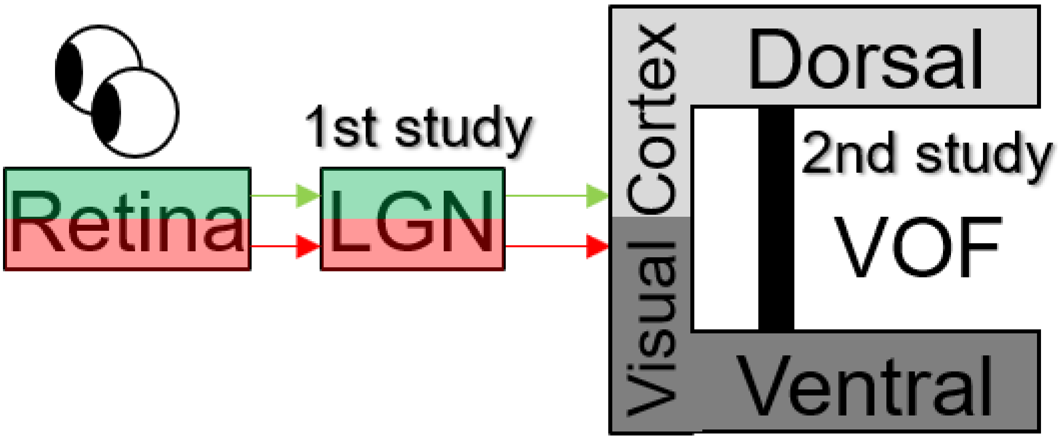

Figure 1.1.1 Schematic depiction of the human visual pathway. The information projected onto the retina is first processed by the neurons in the retina, then processed by the neurons in the LGN. The processed information in the LGN is then transmitted to the visual cortex including V1. This series of the process is the geniculo-cortical pathway. The visual information is processed at visual cortex, from occipital areas including V1 to anterior visual areas in both dorsal and ventral locations. This process is the cortical pathway. The visual information is processed hierarchically in both pathways. The both pathways compromise parallel processing streams. In the geniculo-cortical pathway, the red and green streams

represent magnocellular and parvocellular streams, respectively. In the cortical pathway, the light and dark gray streams represent dorsal and ventral streams, respectively. The dorsal and ventral streams are connected by the white matter tract, vertical occipital fasciculus (VOF). The first (Chapter 2) and second (Chapter 3) studies relate the LGN and VOF, respectively.

1.1.1 Geniculo-cortical pathway

The parallel processing in the geniculo-cortical pathway is composed of magnocellular (M) and parvocellular (P) streams. These M and P streams are derived from the morphological difference of M and P subdivisions of LGN. In this pathway, chromatic and achromatic luminance and their contrast information are detected (Mante et al., 2005). Here I describe the characteristics of the geniculo-cortical pathway.

Retinal ganglion cells

The parallel processing starts from the retinal ganglion cells (RGC). Different features of visual information are processed by the morphologically and functionally different types of RGCs. The RGC terminates mostly in the LGN, and the morphological and functional properties of RGC are preserved in the neurons in the LGN (Callaway, 2005). Since I describe the anatomy and function of the LGN in the next paragraph, I skip the description of those of RGC. Note that there is one more stream, named koniocellular (K) stream but here I also skip the description about the K stream for simplification.

Anatomy of LGN

The LGN can be divided into six layers, which are clearly visible in histological ex-vivo sections (Fig. 1.1.2). LGN is a part of thalamus located deep in the brain and the volume is around 100 - 170 mm^3 (Andrews et al., 1997; Mcketton et al., 2014; Giraldo-Chica and Schneider, 2018). The LGN is surrounded by ventricles and white matter. As mentioned above, the LGN is composed mainly of M and P subdivisions. The M subdivision is composed of lower two layers and the P subdivisions is composed of upper four layers. M neurons are larger than P neurons. The cross-sectional area of a M neuron is around 230 - 273 μm^2 and that of a P neuron is around 129 μm^2 - 177 μm^2 (Yücel et al., 2003). The morphological properties of axons projected from RGC are also different. RGC axons terminating M subdivisions are thicker and more myelinated than those terminating P subdivisions (Yoonessi and Yoonessi, 2011). In a subdivision scale, the P subdivisions is roughly four times larger than M subdivisions (Andrews et al., 1997). The neuronal cell and myelin densities of P subdivisions are larger than those of M subdivisions (Hassler, 1966;

Yücel et al., 2000, 2003; Pistorio et al., 2006). Taken together, M neurons are larger cell bodies and are more sparsely distributed while P neurons are smaller and densely packed (Fig. 1.1.3).

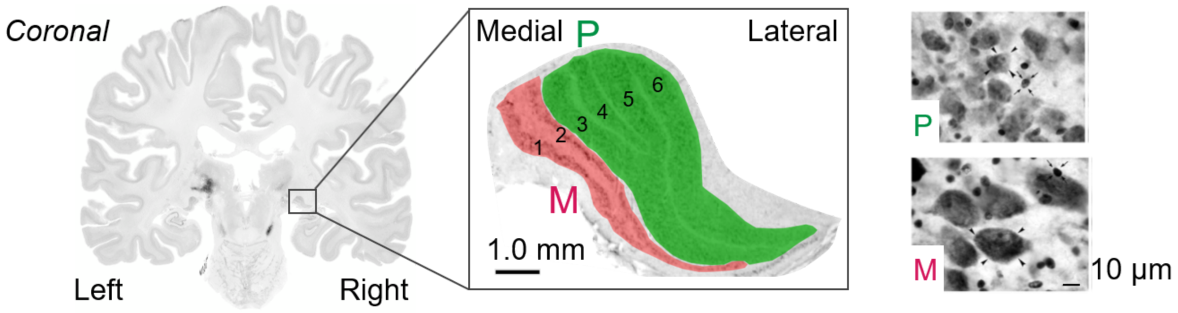

Figure 1.1.2 LGN of the post-mortem human brain. *Left panel.* A coronal section of a post-mortem human brain which includes LGN. LGN is a part of thalamus located deep in the brain. *Middle panel.* The enlarged view of the left panel around the LGN. Six layers are visible in the LGN. The lower two layers are M subdivisions and the upper four layers are P subdivisions, overlaid by translucent red and green colors, respectively. This picture of the postmortem human brain is from the dataset of the BigBrain (Amunts et al., 2013). *Right panel.* The neurons in human M and P subdivisions. The arrows depict the neurons in each subdivision. M neurons are larger than P neurons. This figure was adapted from (Selemon and Begovic, 2007).

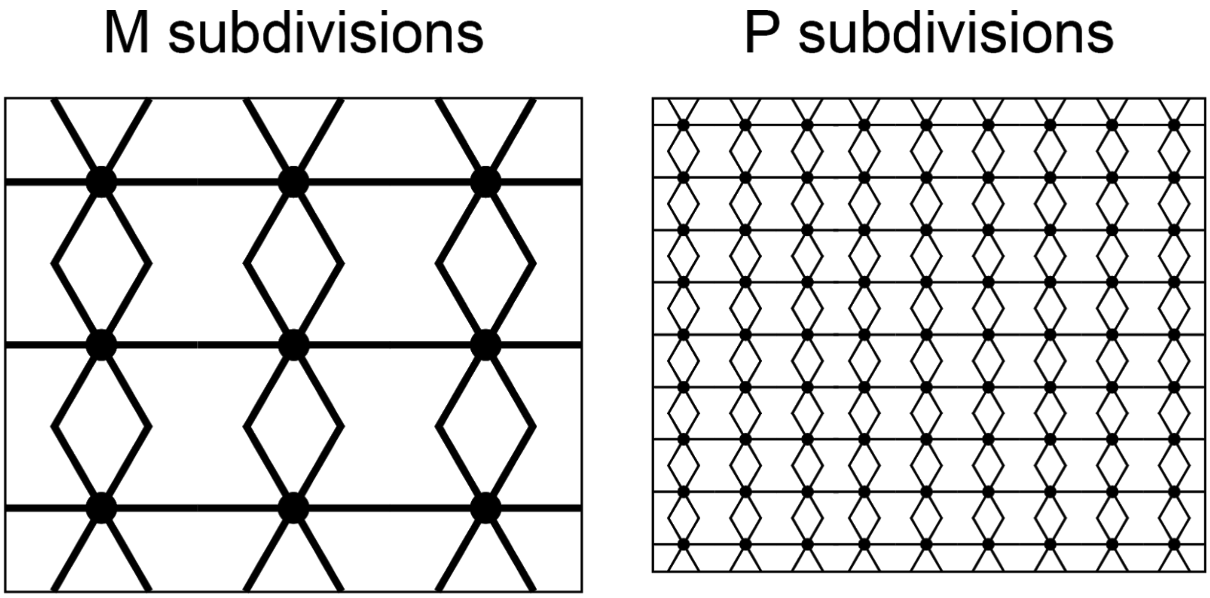

Figure 1.1.3 Schematic depictions of neurons in M and P subdivisions of LGN. The filled circles and connected lines represent cell bodies and axons, respectively. M neurons (left panel) are larger cell bodies and are more sparsely distributed while P neurons (right panel) are smaller and densely packed.

Function of LGN

Neurons in the LGN have ON-OFF or OFF-ON center-surround receptive fields in common, enabling detect luminance and contrast. On the other hand, non-human primate (NHP) studies have reported that the neurons in M and P subdivisions have complementary roles for visual processing. These two neurons have distinct spatial, temporal, luminance, and chromatic stimulus preferences. M neurons have large receptive fields, are more sensitive to luminance contrast but less to wavelength of color, and prefer low spatial and high temporal frequencies. In contrast, P neurons have small receptive fields, are less sensitive to luminance contrast but sensitive to red-green color, and prefer high spatial and low temporal frequencies (see (Derrington and Lennie, 1984; Schiller et al., 1990; Usrey and Reid, 2000; Shapley and Hawken, 2011). Also, M neurons have faster conduction velocities than P neurons (Maunsell et al., 1999). How many neurons in an area codes a visual location is called cortical magnification. The cortical magnification of LGN neurons in the foveal area is larger than that in the peripheral, but this foveal bias is greater in the P subdivision than in the M subdivision (Azzopardi et al., 1999).

Recently, human high resolution fMRI studies attempted to measure the M and P neuronal responses in LGN using the stimuli adjusted to the parameter of NHP physiological literature (Denison et al., 2014; Zhang et al., 2015). These studies showed that the M and P neuronal selective responses are represented in topologically different locations in LGN. However, these studies did not compare the topological functions of M and P subdivisions to the anatomical location of M and P subdivisions in the same single subjects. While the functional definition of these subdivisions have been tested (Schneider et al., 2004; Denison et al., 2014), the 3D configuration of these subdivisions were less-accurate compared with the real configuration of these subdivisions. The structural definition method of the M and P subdivisions in the same subject is important to test the functional imaging of M and P activities. This is the topic of Chapter 2.

Connection of LGN

In the geniculo-cortical pathway, the visual information projected onto the left and right retinae are not integrated till V1. In terms of connection between RGC and LGN, crossed and uncrossed axon bundles from RGC terminate in different layers of the LGN, layer 1, 4 and 6 receive axons from the contralateral eye and 2, 3 and 5 from the ipsilateral eye. In terms of connection between LGN and V1, M and P subdivisions connect to layer 4 in V1, but the projection areas are slightly different. M and P subdivisions project to layer 4Cα and 4Cβ respectively. The projected information is then conveyed to the upper layers in V1.

1.1.2 Cortical pathway

In the cortical pathway, different modalities of visual information (orientation, motion, color and binocular disparity) are hieratically processed. Basically, while the receptive field size of V1 is small, the receptive field size becomes gradually larger along the cortical pathway. Local visual features are detected in V1 and global or complex visual features are detected in higher visual areas. Orientation information is detected in V1, by combining inputs of LGN neurons. The V1 combines the either ON-OFF or OFF-ON center-surround receptive fields of LGN, which extends in one orientation, resulting in forming the oriented receptive fields (Hubel and Wiesel, 1959, 1962). This oriented receptive field enables the detection of an orientation of visual stimulus. Direction of motion is detected in V1 by integrating the representations of neurons that have the same preferred spatial and temporal frequency but have different preferred phases of receptive fields (Adelson and Bergen, 1985). The global motion is detected in MT by integrating the signals of these neuronal representations (Simoncelli and Heeger, 1998). In terms of color processing, while red and green colors are detected in LGN, the spatial and temporal color contrasts are detected in V1 by double-opponent wavelength selective neurons (Conway et al., 2002), then hue information is detected in V2 and V4 (Heywood and Cowey, 1987; Conway, 2003; Xiao et al., 2003). These color processes contribute to the detection of texture information of object surfaces in V4 and IT areas (Kornblith et al., 2013; Okazawa et al., 2015).

Visual information of the cortical pathway is processed in parallel and then integrated (Felleman and Van Essen, 1991; Van Essen et al., 1992). The parallel processing in the cortical pathway is composed of dorsal and ventral streams. The dorsal stream processes visual information for visually guided movement, e.g. localizing objects in space and grasping objects. Thick stripes in V2, V3d, V3A,V3B, MT and IPS belong to dorsal streams. The ventral stream processes for object recognition (e.g. identifying object categories or faces). Thin stripes in V2, V4, LO, IT belongs to ventral streams. Dorsal and ventral streams are reciprocally connected (Felleman and Van Essen, 1991; Ungerleider et al., 2008), which connection is crucial for global perception of object location and identity at once (Farivar, 2009).

In the rest of the subsection, I describe the binocular disparity processing in the cortical pathway because this modality relates to the second study in this dissertation. I first describe the relationship between binocular disparity and depth perception. I next describe how the cortical pathway processes the binocular disparity and transforms into perceptually corresponding depth information in the cortical pathway. I finally describe the unsolved question about the relationship between the depth perception and the human cortical pathway.

The relationship between binocular disparity and depth perception

binocular disparity and depth

Humans see the external world using two eyes. What visual information can we obtain using two eyes? Fig. 1.2.1A describes the geometry of binocular vision viewed in the horizontal plane. When an observer keeps fixation on a point (F), the image of F is projected onto the center of left and right retinae (F'L for left retina and F'R for right retina). At that time, a point (S) is projected onto the left side of the center of each retina (S'L for left retina and S'R for right retina). The positional difference between F'L and S'L is the same as that between F'R and S'R. All points on the circle passing through the fixation point F is projected to geometrically corresponding points in the two retinae. This circle is called the Vieth-Muller or geometrical/theoretical horopter. Any point on the theoretical horopter is seen as single. The single vision using both eyes is called binocular fusion. However, our binocular fusion area is larger than the theoretical horopter (Fig. 1.2.1B), which is called Panum's fusional area or empirical horopter. The empirical horopter has a width in front and behind of the theoretical horopter. Our two eyes receive the same image if a target object is located on the both horopters. In other words, our two eyes receive different images if a target object is located outside of the both horopters. If a target point (P) is farther than a fixation point, a target image is projected onto the right side of left retina and the left side of right retina (Fig. 1.2.1A). The positional difference between both retinal images is called binocular disparity. Binocular disparity is defined using a visual angle difference between fixation and target (α - β). The angle difference (α - β) is the same as DL + DR. If a target is located farther than a fixation point, α is larger than β and its binocular disparity is thus positive. The binocular disparity in this case is called uncrossed disparity. If a target is located nearer than a fixation point, the visual angle of the target is smaller than that of the fixation point and its binocular disparity is thus negative. The binocular disparity in this case is called crossed disparity. If a target is on the horopter (e.g. the point of F), the binocular disparity is zero, which is called zero disparity. The geometrical relationship between the binocular disparity (α - β) and distance difference between fixation point and target is below.

$$\alpha - \beta \cong \frac{dE}{D^2}$$

Where “D” is distance of fixation, “d” is distance difference between target and fixation and “E” is the inter eye pupil distance. This is an approximation formula on the assumption that E is very smaller than D. There is a positive correlation between binocular disparity (α - β) and d. This formula means that if binocular disparity is known, the distance is calculable.

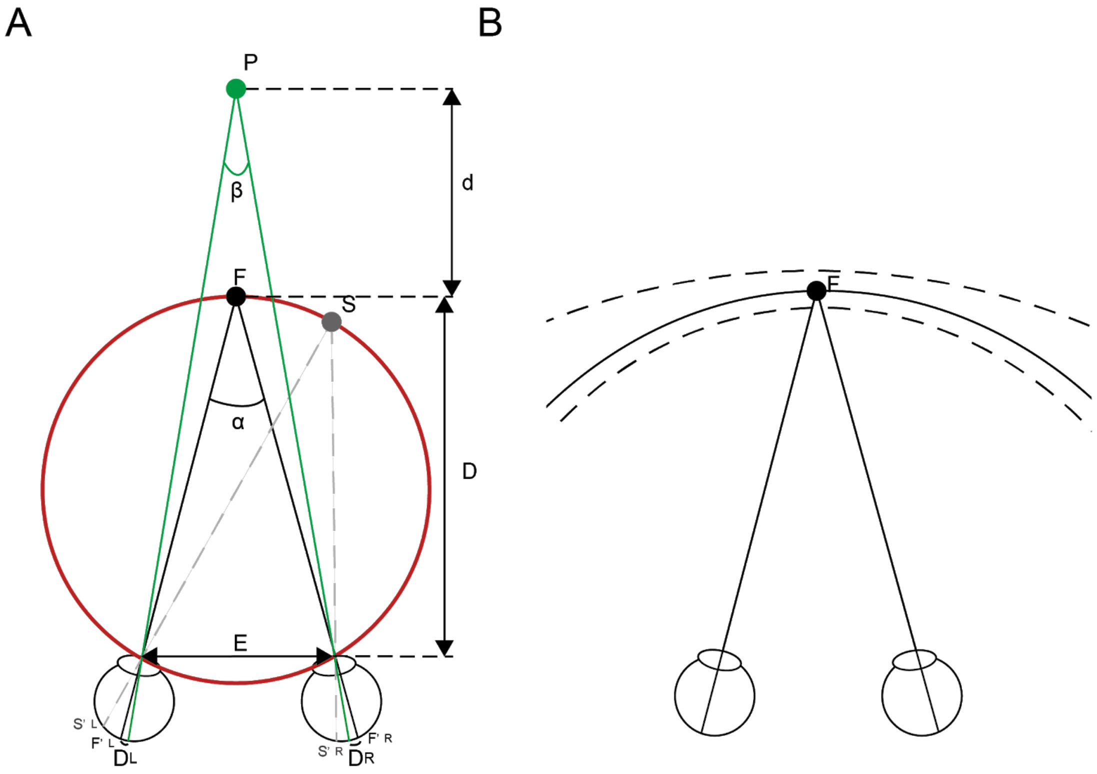

Figure 1.2.1 Geometry of binocular vision in horizontal plane. A. The geometry of theoretical horopter and depth representation. The point F is a fixation point. The F’L and F’R are locations of the F image in the left and right eye, respectively. S is the point on the theoretical horopter (Red circle). The S’L and S’R are locations of S images. The P is a point located farther than F. The α is a visual angle of F and the β is a visual angle of P. The D is a distance between an eye and F. The d is a distance between F and P. E is an inter-eye pupil distance. B. The geometry of the empirical horopter. The point F is a fixation point. Details of A and B are described in the subsubsubsection “binocular disparity and depth”.

Absolute and relative disparities

To understand binocular disparity in the framework of our perception, binocular disparity can be classified into two types of disparity, absolute and relative disparity. The absolute disparity represents the disparity of a target. Thus, the absolute disparity is variable based on the convergence angle (e.g. DL and DR in the Fig. 1.2.1A). The relative disparity is the difference in disparity between target and another target. Thus, the relative disparity is invariant to the convergence angle of targets whose depth is compared. The relative disparity is a cue to perceive depth between two objects. When the eyes are moved, the objects change positions on the retina. In this case absolute disparities of both objects are changed, but the relative disparity between objects is constant. Human depth perception relies considerably on the relative disparity (Westheimer, 1979). When an object moves back and force, it is easier for us to perceive depth change if there are fixed objects around the target object compared to the case in which there is no reference object around the target object. This suggests that our brain employs relative disparity framework to perceive depth (stereopsis).

Correlated and anticorrelated random dot stereograms

To detect binocular disparity, it is necessary to determine corresponding elements between left and right retinal images. This is called a corresponding problem. Julesz (1971) used Random dot stereogram (RDS; Fig. 1.2.2) and showed that binocular disparity could be divorced from the feature of figural representation (Julesz, 1971). I described how the brain extracts binocular disparity and perceives depth in the subsubsection “Disparity processing in the cortical pathway”.

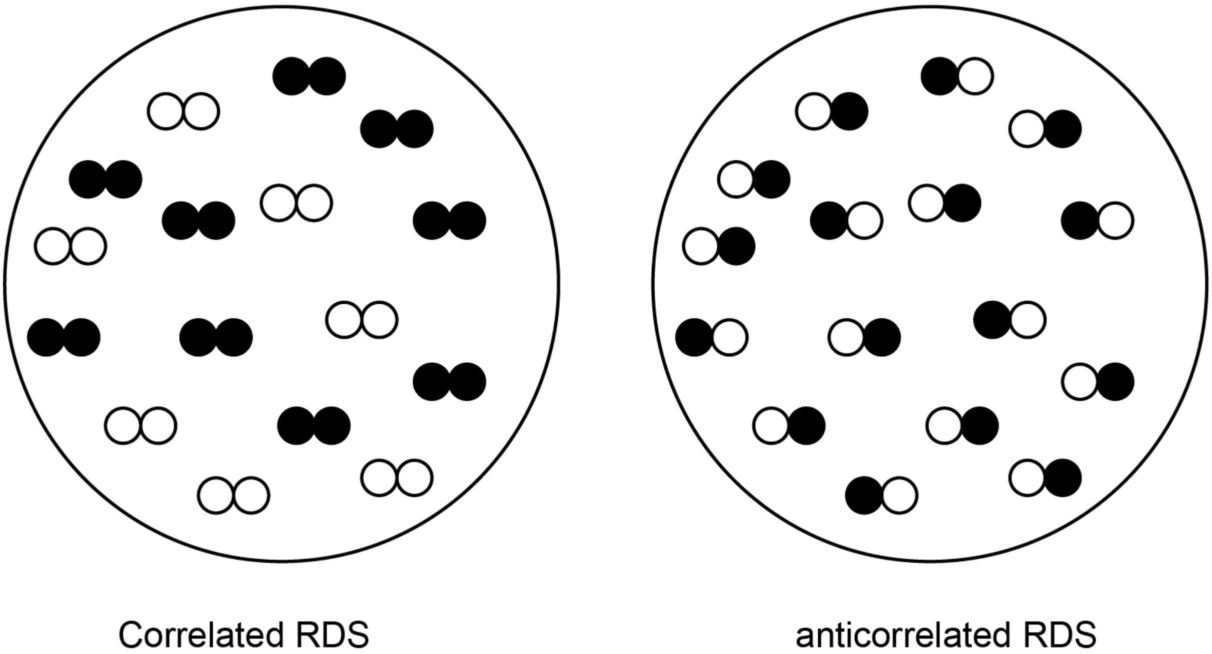

Figure 1.2.2. A schematic illustration of correlated and anti-correlated RDSs. Each pair of dots represents the luminance contrast of a corresponding dot in the left and right retinal images. The left panel represents correlated RDS, where all pairs have matched contrast between both retinal images. Based on the disparity of the matched dots in the left and right retiae, we can see depth in the correlated RDS. The right panel represents anticorrelated RDS, where all pairs have reversed contrast. Coherent depth can be seen in the correlated RDS but not in the anticorrelated RDS.

Disparity processing in the cortical pathway

Disparity processing in V1

The first processing area of binocular disparity is primary visual area, or V1 (Barlow et al., 1967). In V1, the visual information of left and right retinae are integrated by combining the ipsilateral and contralateral inputs of LGN neurons, resulting neurons of V1 have a binocular receptive field (Hubel and Wiesel, 1959). V1 neurons respond selectively to disparities (crossed, uncrossed and zero disparity). There are roughly two types of neurons, which detect binocular disparity. The one is a binocular simple cell. This neuron has different phase and position preferred receptive fields in the left and right eye. The zero disparity is detected by the left and right eye receptive fields, which have the same phase and position preference. The crossed or uncrossed disparity are detected by the left and right eye receptive fields, which have the phase and position shifted preference. Thus, the detection of the binocular disparity of this neuron depends on the phase and position. The other type of disparity selective neuron is a binocular complex cell. In contrast to the binocular simple cell, this neuron can detect binocular disparity, independent of phase and position in the receptive field. The disparity detection of this neuron is modeled as the sum of squares of at least four binocular simple cells, whose phase preferences are shifted by 90 deg. The model of this cell is called a binocular energy model (BEM). Ohzawa and colleagues provided the BEM as the reasonable neural model of V1 neuron response to disparity (Ohzawa et al., 1990, 1997).

The BEM can be mathematically regarded as the calculation of the correlation of left and right images (Qian and Zhu, 1997). When viewing a binocularly correlated RDS (Fig.1.2. 2), the model calculates the correlation of paired dots in the left and right images. When viewing a binocularly anti-correlated RDS (Fig. 1.2.2), where a white dot in the left image matches a black dot in the right eye, the model shows the flipped response profile against the response profile of the correlated RDS. Like the model, V1 neurons show preferences to both correlated and anti-correlated RDS (Cumming and Parker, 1997).

However, there are discrepancies between disparity response profiles in V1 and our perception to binocular disparity. The one is our depth perception becomes ambiguous when viewing anticorrelated RDS (Julesz, 1960; Tanabe et al., 2008; Doi et al., 2011; Hibbard et al., 2014). This indicates that, to perceive depth of entire RDS, dot contrasts should be matched between left and right retina images. The size of receptive field of V1 neurons is small and in fact V1 neurons compute only coherence of local contrast between both retinal images (Cumming and Parker, 1997). Another difference between our perception and V1 neuron response is that V1 responses describe well absolute disparity but not describe relative disparity (Cumming and Parker, 1999). As I mentioned in the previous subsubsection, our depth perception relies on the relative disparity framework. Taken together, V1 neurons detect binocular disparity, but depth plane perception needs global matching computation and extrastriate cortex should do that.

Disparity processing in dorsal and ventral streams

There are two disparity processing streams after V1. One is dorsal stream which is located in the dorsal part of occipital area, middle temporal area and intraparietal sulcus. The other one is the ventral stream which is located in the ventral part of the occipital area and inferior temporal cortex. In macaque and human, both dorsal and ventral streams are involved in processing binocular disparity (Janssen et al., 2003; Tsao et al., 2003; Tanabe et al., 2004; Uka et al., 2005; Parker, 2007).

Where is the substrate whose computation is consistent with our depth perception? Previous macaque electrophysiology and human fMRI used correlated and anticorrelated RDSs and measured responses from a variety of extrastriate areas. In macaque studies of ventral streams, Tanabe and colleagues (2004) found that V4 neurons showed attenuation of responses to anticorrelated RDSs (Tanabe et al., 2004). Janssen and colleagues (2003) also found the absent response sensitivity to anticorrelated RDSs in the inferior temporal (IT) cortex (Janssen et al., 2003). These results suggest that in the ventral stream of macaque after V4, matching computation is performed, i.e. corresponding problem is solved in V4. Shiozaki and colleagues applied a microstimulation technique to V4 and succeeded in manipulating the depth discrimination performance, suggesting a causal role for V4 in perceptual disparity detections.

In humans, Bridge and Parker (2007) provide the first fMRI measurements with anticorrelated RDS and found that response reductions to anticorrelated RDS in higher visual areas (Bridge and Parker, 2007). Preston and colleagues (2008) analyzed voxels' response pattern in each visual area to correlated and anticorrelated RDS and tested decoding accuracy (Preston et al., 2008). They found that the decoding accuracy was significantly higher for correlated RDS than anticorrelated RDS in higher dorsal (V3A, V3B, IPS-0) and ventral (lateral occipital (LO)) areas, suggesting disparity representations in these dorsal and ventral visual areas are consistent with our depth perception. In sum, higher dorsal and ventral visual areas are involved in perceptual related disparity processing.

Stereoacuity

Stereopsis performance can be determined using stereoacuity. The stereoacuity is the smallest detectable step of binocular disparity. RDS is one of the best research tools of stereoacuity. This is because the depth cue in RDS is only the binocular disparity. RDS consists of random pattern elements which are shifted between two images. We can conduct a quantitative stereoacuity measurement by changing the size of binocular disparity in RDS. The stereoacuity threshold is usually defined as the binocular disparities discriminated on 75% or 84% (1 standard deviation from the mean) of trials.

Some people have impaire stereoacuity who can not use binocular disparity to perceive depth. One cause of stereoblind is eye-derived problems (e.g. strabismus or amblyopia). Strabismus is a condition in which the eyes don’t properly align with each other when fixating. Amblyopia is a condition in which visual acuity of either or both eyes are very low. In these cases, it is difficult to compare both retina images so that stereopsis performance is poorer than intact people.

While the stereoacuity declines with the visual disorders, previous psychological studies tested a large population of human stereoacuity and found that humans have a substantial individual difference in stereoacuity (Zaroff et al., 2003; Hess et al., 2015). Hess and colleagues (2015) measured stereoacuity of over five hundreds people and found that human stereoacuity distribution is bimodal. This indicates that humans with intact eyes can be classified into two groups, good and poor stereoacuity groups. The unsolved question is: Are there any neural basis of the human individual difference in stereoacuity? To reveal the basis, it is crucial to measure the human visual pathway using noninvasive neuroimaging methods. I describe how to measure the neural properties of the human brain in the section “Neuroimaging methods and analyses for investigating the human visual pathway”.

Relationship between stereoacuity and human cortical pathway

Human neuropsychological studies showed that the cortical damage either in higher dorsal or ventral areas impair stereoacuity (dorsal: IPS-0 (Murphy et al., 2016), ventral: LO (Read et al., 2010; Bridge et al., 2013)). These conversing evidence suggest that stereoacuity declines even if either dorsal or ventral is damaged. Surprisingly, Bridge and colleagues (2013) found that a patient with ventral lesion showed significant volume reduction in dorsal area compared with control participants. Taken together, the dorsal and ventral visual areas may communicate with each other and this communication may contribute to depth discrimination.

White matter tracts in the visual pathway

The cerebral cortex consists of gray matter and white matter. Gray matter mainly consists of cell bodies while white matter mainly consists of axons and glial cells. Pyramidal cells in gray matter convey signals to other cells via axons. The bundle of axons is called a white matter tract. One may argue that gray matter is a basis of our behavior because functional activities are measured in gray matter rather than white matter. However, lesions in white matter disrupt human behavior. For example, aphasia (speech disorder) is a lesion at white matter tract between Broca's and Wernicke's areas (Eggert, 1977). This finding arised an idea that a function arises from the pattern of long-range cortical connections (Catani and Ffytche, 2005). This is the classic concept of connectionism (Eggert, 1977). Consistent with the connectionism, recent human studies suggests that the anatomical properties of white matter tissue correlate with behavior, for example, reading skill (Yeatman et al., 2011, 2012a) and face recognition (Tavor et al., 2014; Gomez et al., 2015). Although how white matter tissue impacts neural processes is still debated, white matter properties do relate to behavior (Sampaio-Baptista and Johansen-Berg, 2017).

There are a variety of white matter tracts. Four kinds of white matter tracts connecting visual areas were certainly identified in postmortem and living humans (Rokem et al., 2017). The optic radiation is a tract connecting lateral geniculate nucleus and V1. Forceps major is a part of callosal connecting left and right occipital areas. Inferior longitudinal fasciculus is a tract connecting occipital area (primary visual cortex) and temporal area (anterior temporal cortex). Vertical occipital fasciculus (VOF) is a tract connecting higher dorsal and ventral visual areas.

The VOF was visually inspected in the 19th century (Wernicke, 1881; Sachs, 1892; Dejerine and Dejerine-Klumpke, 1895) but its existence was widely ignored. The VOF was rediscovered recently (Martino and García-Porrero, 2013; Yeatman et al., 2013, 2014b; Takemura et al., 2016b, 2017). The main dorsal endpoints are near V3A and V3B, and the main ventral endpoints are near hV4 and VO (ventral occipital) and LO (Takemura et al., 2016). The visual representations of the both dorsal and ventral VOF endpoint areas cover both upper and lower visual fields, suggesting VOF contributes to transfer upper visual field information in dorsal area to ventral area and lower visual field information in ventral area to dorsal area to build hemifield representation.

1.2 Neuroimaging methods and analyses for investigating the human visual pathway

Investing the visual pathway of living humans requires the methods of noninvasive brain measurements. MRI can noninvasively measure the neural properties of visual areas, providing an opportunity to study the organization of the human visual pathway and the neural basis of human visual perception. In this section, I describe the key MRI methods and analyses for the first and second studies: macromolecular tissue volume (MTV) imaging, diffusion MRI (DMRI) and tractography.

1.2.1 Macromolecular tissue volume (MTV) imaging

MTV quantifies physical properties of neural tissue density (Mezer et al., 2013). MTV quantifies non water volume in each voxel. The equation is below.

$$MTV = 1 - PD$$

Where proton density (PD) relates the amount of water in each voxel. Thus, the MTV is the density of non-water content. The important thing about MTV is quantitatively. General structural MRI measurements including T1-weighted images have inhomogeneities of MR image intensity (see the left panel of Fig. 1.3.1). The inhomogeneities are not dependent on the tissue properties of the brain but are related to the different biases of MRI coil sensitivities. The MR intensity of the brain areas near a coil are greater than the brain areas far from a coil. The weighted image is generated by the mean of the images acquired by each coil. By averaging each coil image, the large intensity biases are smoothed. However, local biases exist in the T1 weighted image. Basically, the MTV minimizes the bias by measuring multiple MR images in each coil using different acquisition parameters of MRI excitation strength and implementing the least square estimation across coil images (Mezer et al., 2013, 2016). By this analysis, MTV enables quantitative estimation of the brain structure (see the right panel of Fig. 1.3.1).

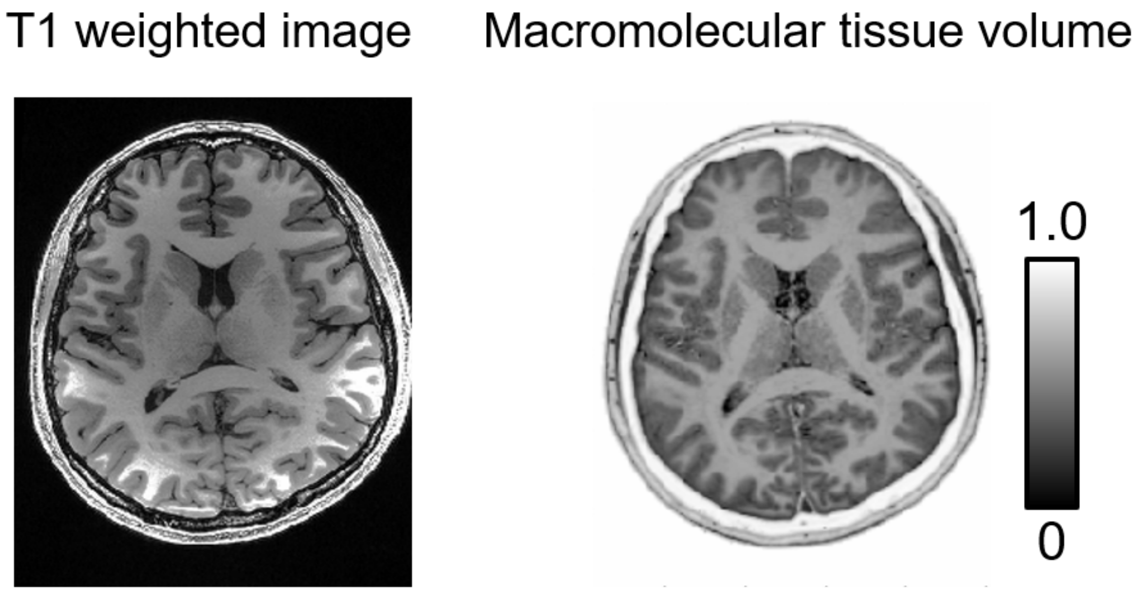

Figure 1.3.1. Non-quantitative and quantitative images. The left image is a T1 weighted image where the inhomogeneity is not corrected, thus non-quantitative. The lateral areas are darker than the other areas. The right image is the image of MTV, which corrects MR signal inhomogeneity. The bright color represents high neural tissue density areas and dark color represents low neural tissue density areas. Since the ventricles are almost filled with water, the color of the areas are dark.

1.2.2 DMRI

DMRI and related analysis enables to measure the configurations of white matter tracts. DMRI measures the magnitude and orientation of water diffusion of each voxel in the brain. Diffusion of water molecules differs depending on where water molecules are. In sparse areas, water molecules perform brownian movement and they diffuse isotropic direction over time. Conversely, in dense areas of white matter tracts, water molecules diffuse anisotropic direction along white matter tracts because diffusion of water molecules is restricted by tract and water molecules diffuse preferentially along tract.

A simple DMRI sequence consists of spin echo (SE) pulse sequence and motion probing gradient (MPG). First I describe the SE pulse sequence (Fig. 1.3.2). SE pulse sequence consists of 90° and 180° radiofrequency(RF) pulses. In the MRI scanner, spin directions of nucleuses of tissue are aligned to the direction of static magnetic fields. 90°RF pulse tilts spin directions of tissue nucleus to transverse direction and aligns phases of tissue nucleus. After that, phases of the nucleus become dispersed, but 180° RF pulse flips every spin direction and aligns phases again. This procedure generates strong transverse magnetization echo of nucleus resonance. MR coil measures this echo and builds the image of the brain. The strength of echo is different depending on local tissue property. In the SE sequence, after 90° RF pulse tilts spin directions of all nucleuses to transverse direction, as time advances, molecules' spin directions return to former directions. The spin direction recovery time is called relaxation time. Lipid molecules show shorter relaxation time than water molecules. The echo strength relates with the magnitude of transverse magnetization, so echo signal is different depending on tissue component.

MPG changes magnetic field strength along a direction and changes spin phases along the direction. In dMRI sequence, MPG is applied before and after the 180° RF pulse. The impact of MPG to echo signal is described using b.

$b \propto A^2 \Delta$

Where A is a magnitude of MPG and Δ is a duration of MPG. If the period of MPG is long, a lot of molecules (specifically water molecules) diffuse and then spin phases become dispersed. The echo signal is then weak. Taken together, the reduction of dMRI echo signal reflects the diffusion of water molecules along the MPG direction. By changing directions of MPG, different direction diffusions are measurable.

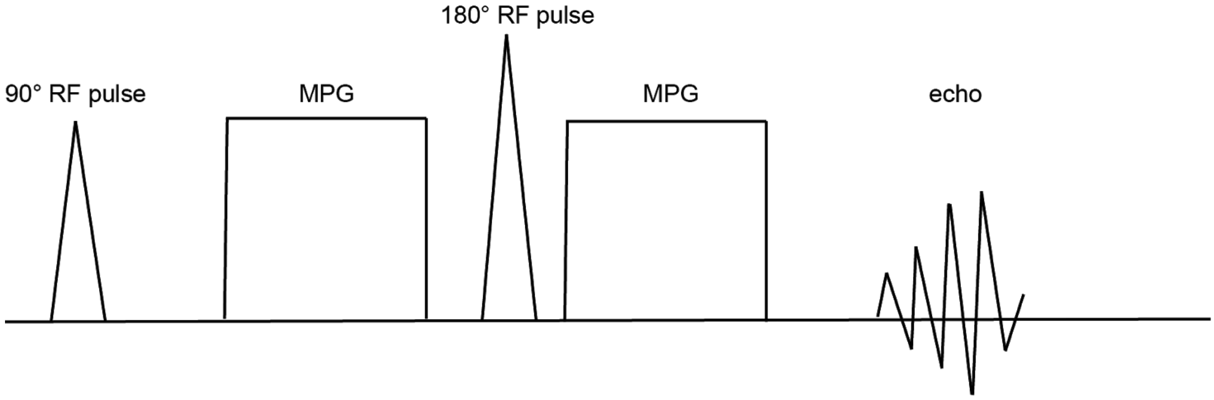

Figure 1.3.2. DMRI sequence. DMRI sequence consists of 90° RF pulse, MPG, 180° RF pulse and MPG in applied timing order. Echo is observed after each sequence. Details are described in the subsection "DMRI".

1.2.3 Tractography

The model of water diffusion of white matter tracts

Tractography enables to identify spatial configuration of white matter tracts using dMRI data. Streamlines (reconstructed fibers of a tract) are derived from dMRI data in individual voxels. First, I describe how to model the dMRI data within a voxel. The classical model is diffusion tensor model (DTM), which models dMRI data fitting ellipsoid defined by three eigenvectors

(Basser et al., 1994a, 1994b). The DTM gives rise to simple useful statistics. One is fractional anisotropy (FA), which describes the degree of anisotropic diffusion (Fig. 1.3.3A).

$$FA = \sqrt{\frac{1}{2}}\sqrt{\frac{(\lambda 1-\lambda 2)^2 + (\lambda 2-\lambda 3)^2 + (\lambda 3-\lambda 1)^2}{\sqrt{\lambda 1^2 + \lambda 2^2 + \lambda 3^2}}}$$

Where λ1, λ2, λ3 are eigenvectors. This DTM is simple but useful when measuring a few directions of diffusion signal. However, DTM cannot describe detailed fiber configurations e.g. crossing fibers. When measuring many directions of dMRI signals, more complex models work well. Tournier and colleagues (2004) introduced a constrained spherical deconvolution (CSD) model, which uses spherical harmonics (Fig. 1.3.3B). CSD model enables to describe crossing fibers (Tournier et al., 2004).

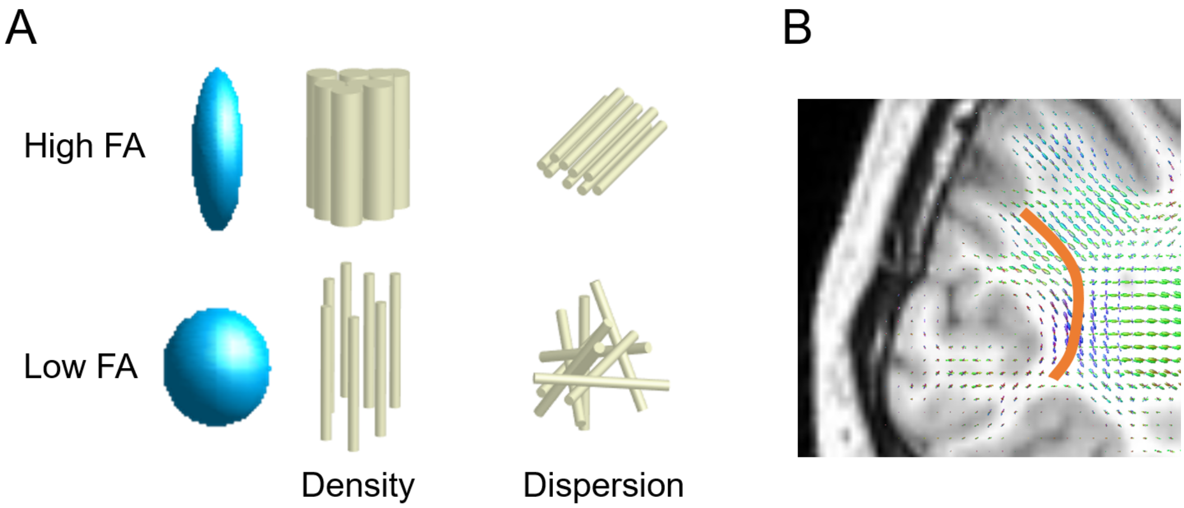

Figure 1.3.3. DMRI statistics and Tractography. A. Schematic of FA. FA is a degree of anisotropic diffusion. High FA represents water diffusion is strongly restricted by white matter fibers. The degree of fiber density and dispersion affects FA value. B. Schematic of tractography using CSD model. The CSD model is fitted in each voxel of white matter. Orange line represents streamline. The CSD model can describe more diffusion orientation than DTM. The CSD model is thus more appropriate to generate curving streamlines.

White matter tract estimation

Tractography connects the oriented water diffusions of individual voxels and reconstruct streamlines. The classical tractography method is deterministic tractography (Mori et al., 1999). This method greedily connects principal diffusion orientation of voxels. Most of the streamlines made by this method are linear. This method cannot describe curving fibers. To solve this problem, probabilistic tractography is introduced (Tournier et al., 2012). This tractography method connects not only principal diffusion orientation but also connects other diffusion orientation of individual voxels, resulting in generating various configuration streamlines. Whole brain streamlines are called connectome. Connectome should be statistically validated and remove false positive streamlines. Pestilli and colleagues (2014) introduced a method linear fascicle evaluation (LiFE) (Pestilli et al., 2014). The LiFE evaluates the strength of the evidence of each streamline existence. The LiFE predicts dMRI signal of each voxel using connectome and calculates the weight of each streamline that contributes to the prediction. They observed about 80% of connectomes are zero weight that do not contribute to the prediction. Using LiFE, plausible streamlines are selected.

Tractometry of white matter tracts

By superimposing FA or MTV data on streamlines estimated by dMRI data, we can calculate the FA and MTV along the streamlines. Thus, we can estimate the anisotropy of the water diffusion or neural tissue density of white matter tracts by FA or MTV, respectively. The procedure of profiling the structural properties on a white matter tract is called tractometry. Comparing FA and MTV, MTV can detect tissue differences that FA could not. Mezer and colleagues (2013) measured multiple sclerosis patients and found MTV difference of corticospinal tract (CT), which is not observed using FA (Mezer et al., 2013). CT intersects many other tracts. Their result suggests FA shows low reliability in crossing fiber regions while MTV shows robustness there.

Note that this superimposing procedure can be implemented not only white matter tracts but also cortical and subcortical areas. In Chapter 2, I superimposed the MTV on the LGN and investigated the difference of MTV in the LGN.

Chapter 2.

Macromolecular tissue volume mapping of lateral geniculate nucleus subdivisions in living human brains

2.1 Introduction

The lateral geniculate nucleus (LGN) plays an essential role for visual processing in the human visual system, by receiving visual inputs from retinal ganglion cells and transferring those signals to the primary visual cortex (V1) (Nassi and Callaway, 2009). Besides the function as a relay station, a growing body of evidence suggests the involvement of LGN in wide ranges of visual functions, such as eye-specific dominance and suppression during binocular rivalry (Haynes et al., 2005), visual attention (O'Connor et al., 2002; Schneider and Kastner, 2009; Ling et al., 2015), and visual perceptual learning (Yu et al., 2016). The LGN is also involved with neuronal synchrony widely observed in the visual cortex (Hughes et al., 2004; Liu et al., 2012; Minami et al., 2020).

Human LGN is composed of six layers which are categorized into two major subdivisions, magnocellular and parvocellular subdivisions (hereafter M and P subdivision, respectively). These subdivisions are clearly distinguishable on the basis of cell size (Hickey and Guillery, 1979). A number of studies suggested that these two subdivisions have complementary roles in visual processing, by demonstrating distinct spatial, temporal, luminance, and chromatic stimulus preferences (Derrington and Lennie, 1984; Schiller et al., 1990; Usrey and Reid, 2000; Denison et al., 2014). Based on these observations, previous studies have proposed that distinct roles of M and P subdivisions in attention (Yeshurun and Levy, 2003) and reading (Demb et al., 1998; Stein, 2001; Main et al., 2014) based upon psychophysical performance on specific types of visual stimuli and their relevance to neural response in M and P subdivisions. A psychophysical study using a motion coherence task also led to a hypothesis that M subdivisions received damage earlier than P subdivision as a consequence of glaucoma (Joffe et al., 1997). However, hypotheses proposed by previous psychophysical studies remain speculative because they are mostly derived from similarities between neural response selectivities of M and P subdivision and stimulus dependence of psychophysical performances, without comparisons with functional or structural measurement on M and P subdivisions. Therefore, it is essential to establish such non-invasive measurements, which enables a direct comparison between neuroimaging data of LGN subdivisions and psychophysical data, and a comparison between properties of LGN subdivisions and those in visual cortical areas.

The non-invasive neuroimaging measurements on structural properties of human LGN subdivisions have not been established, because of the requirement for high-resolution, quantitative MRI measurements for the LGN, which has a volume around 180 mm^3 (Mcketton et al., 2014). While functional MRI (fMRI) has been used to localize M and P subdivisions based upon BOLD response selectivity for distinct visual stimuli (Denison et al., 2014; Zhang et al., 2015, 2016), spatial resolution ($1.25\times1.25\times1.2$ mm^3 - $1.75\times1.75\times1.5$ mm^3) and robustness of the measurements are limited. fMRI measurements also require visual stimulus presentations, which limit applicability for clinical populations with visual field loss.

In order to examine the properties of LGN subdivisions in individual living humans, here I propose a method to identify LGN subdivisions using structural MRI measurements. To this end, I primarily used macromolecular tissue volume (MTV) mapping, which is a quantitative structural MRI method sensitive to a fraction of non-water macromolecules (Mezer et al., 2013). I hypothesize that MTV fraction will provide a clue to distinguish M and P subdivisions, since (1) MTV is sensitive to lipids which constitutes cell membrane and myelin (Mezer et al., 2013; Filo et al., 2019; Shtangel and Mezer, 2020) and (2) neuronal cell and myelin densities differ between M and P subdivisions (Hassler, 1966; Yücel et al., 2000, 2003; Pistorio et al., 2006). In a proposed method, I first identify the location and contour of the whole LGN using a high-resolution proton-density (PD)-weighted image as used in previous studies on human LGN (Mcketton et al., 2014; Viviano and Schneider, 2015; Giraldo-Chica and Schneider, 2018). I then defined the subdivisions in the LGN based upon MTV fraction data using the anatomically known volume ratio of M and P subdivisions. I finally tested the validity of the definition based upon (1) comparisons with histology data, (2) fMRI measurements on stimulus selectivity, and (3) analyzing test-retest reliability.

As a result, I found a gradual change of MTV fraction within LGN in each axis (lateral-medial, dorsal-ventral, and anterior-posterior). This pattern of change was consistent across subjects and was also in line with hypotheses expected from known histological findings on the LGN subdivisions. I also found that the difference in stimulus selectivity between the subdivisions is consistent with previous literature. The definition was robust across measurements on different days. The definition of subdivisions using widely used non-quantitative methods, such as T1-weighted/T2-weighted ratio map, was not sufficient for identifying LGN subdivisions as compared with MTV, suggesting that quantitative structural mapping is crucial for identifying the M and P subdivisions in human LGN. This study provides a novel method to non-invasively investigate the properties of LGN subdivisions in living human brains, which can be combined with functional or behavioral experiments to test neuroscientific or clinical hypotheses.

2.2 Materials and Methods

2.2.1 Subjects

Fifteen healthy volunteers (8 male, 7 female; mean age, 23.53 years old; standard deviation, 1.71 years old; range, 21-26 years old) participated in the study. All subjects had normal or corrected-to-normal vision, without clinical histories of eye disease. All participants gave written informed consent to take part in this study. The study was conducted in accordance with the ethical standards stated in the Declaration of Helsinki and approved by the local ethics and safety committees at the Center for Information and Neural Networks (CiNet), National Institute of Information and Communications Technology (NICT).

2.2.2 Structural MRI data acquisition

All MRI data were collected using a 3T MAGNETOM SIEMENS Prisma scanner (Siemens Healthcare, Erlangen, Germany) in CiNet, NICT with a 32-channel head coil.

T1-weighted MRI data acquisition

T1-weighted magnetization prepared rapid gradient echo (MP-RAGE) images (voxel size, 0.75 mm ×1.0 mm × 0.75 mm; Repetition Time [TR], 1900 ms; Echo Time [TE], 3.58 ms; flip angle, 9°; 256×256 matrix; in-plane acceleration factor, 2) were acquired from all subjects. This image was used as a reference to coregister the subsequent MRI data (PD-weighted, MTV, and fMRI) in the same coordinate space on each individual subject. The total acquisition time for the T1-weighted MRI data was approximately 15 min for each subject.

Proton density (PD)-weighted MRI data acquisition

PD-weighted images were acquired in all participants in order to identify the location of the LGN. Acquisition parameter of PD-weighted images follows those used in a previous study

(Viviano and Schneider, 2015); voxel size, 0.75 mm × 0.75 mm × 1.0 mm; TR, 3000 ms; TE, 21.0 ms; flip angle, 120°; 256×256 matrix; in-plane acceleration factor, 2). PD-weighted image acquisition was repeated at least 40 times in all subjects. We further repeated PD-weighted image acquisition when subjects agreed to continue the acquisition to improve the signal-to-noise ratio (maximum number of repetitions: 60). Each image consisted of 50-60 coronal slices (slice thickness, 1 mm; no gap), covering the whole posterior thalamus. The total acquisition time for the PD-weighted MRI data was approximately 60-90 min for each subject, depending on the number of repetitions.

MTV data acquisition

MTV data was acquired from all subjects. Acquisition protocol for MTV follows those described in previous publications (Mezer et al., 2013; Filo et al., 2019; Minami et al., 2020; Takemura et al., 2020). Four fast low-angle shot (FLASH) images were measured with flip angles of 4°, 10°, 20°, and 30° (TR, 12 ms; TE, 2.43 ms) with 1 mm isotropic voxels. For the purposes of removing field inhomogeneities, five additional spin echo inversion recovery (SEIR) scans were also measured with an EPI readout (TR, 3 s; TE, 49 ms; 2 × acceleration). The inversion times were 50, 200, 400, 1200, and 2400 ms. In-plane resolution and slice thickness of the additional scan were 2 × 2 mm^2 and 4 mm, respectively. The total scan time of qMRI was approximately 35 min for each participant. For 11 subjects, I acquired MTV data again on a different day for evaluating test-retest reproducibility.

T1w/T2w MRI data acquisition

For 13 subjects, I also acquired data for T1-weighted/T2-weighted ratio map (T1w/T2w), which has been widely used in the analysis of Human Connectome Project (HCP) data (Glasser and Van Essen 2011). T1-weighted image was acquired using a 3D MPRAGE (MPRAGE: TR, 2400ms; TE, 2.06ms; TI, 1000ms; flip angle, 8°; bandwidth, 220 Hz/Pixel; echo spacing, 7.5ms; FOV, 256mm × 256mm × 176mm; matrix, 256 × 256 × 176; voxel size, 1mm isotropic resolution) sequence. T2-weighted image was acquired using Sampling Perfection with Application optimized Contrast using different angle Evolutions (SPACE: TR, 3200ms; TE, 438ms; flip angle, 120°; bandwidth, 574 Hz/Pixel; echo spacing, 3.88ms; Turbo Factor, 139; FOV, 256mm × 256mm × 176mm; matrix, 256 × 256 × 176; voxel size, 1mm isotropic resolution) sequence. While these acquisition protocols aimed to follow those of HCP (Glasser and Van Essen 2011), acquisition parameters are not fully identical to HCP because of hardware differences. These data were also collected with prescan normalization, which corrects image intensity inhomogeneity.

2.2.3 Structural MRI data analysis

T1-weighted MRI data

T1-weighted MRI image of individual subjects were interpolated and aligned to ICBM 152 2009b symmetric template in MNI152 database (http://www.bic.mni.mcgill.ca/ServicesAtlases/ICBM152NLin2009; 0.5 mm isotropic resolution; Fonov et al., 2009, 2011) using rigid-body transformation implemented in FSL FLIRT tool. No spatial smoothing and normalization has been performed. T1-weighted MRI image aligned into MNI152 space was used for subsequent comparisons between qMRI, fMRI and histological data on individual brains in MNI coordinates.

PD-weighted MRI data

The PD-weighted image at the first scanning session was used as a reference, and all subsequent PD images were coregistered to the first image using rigid-body transformation implemented in FSL. We then averaged all PD-weighted images aligned to the first PD-weighted image. The averaged PD-weighted image was then interpolated and aligned to the T1-weighted MRI data, which was further aligned with MNI coordinate with 0.5 mm isotropic resolution, for subsequent analyses.

Quantitative MRI data

Using the mrQ software package (https://github.com/mezera/mrQ) in MATLAB, both the FLASH and SEIR scans were processed to produce the MTV maps (Mezer et al., 2013, 2016). MTV quantifies macromolecular tissue volume density by estimating a quantitative proton-density map from the qMRI dataset after correcting for RF coil bias by the mrQ analysis pipeline using SEIR-EPI scans (Barral et al., 2010; Mezer et al., 2013). Since the cerebrospinal fluid (CSF) voxels are entirely filled with water, I assumed that these voxels had a full water volume fraction (WVF). I then calculated the WVF ratio in cortical gray or white matter voxels compared to CSF. MTV was defined as: MTV = 1 − WVF. It was used to quantify the non-proton macromolecule volume fraction in each voxel. Finally, the MTV map was aligned to T1-weighted MRI data, for further comparisons with other images in the same coordinate space. The full analysis pipeline can be found in previous publications (Mezer et al., 2013, 2016; Oishi et al., 2018; Takemura et al., 2019; Minami et al., 2020).

T1w/T2w MRI data

I obtained a T1w/T2w ratio map by co-registering T2-weighted image to T1-weighted image by using FSL's FLIRT (Jenkinson et al., 2002) with 6 parameters (rigid body), and calculated the ratio between them. The T1w/T2w ratio map is then co-registered to the reference T1-weighted MRI data in the MNI coordinate.

2.2.4 Identifying region-of-interest from structural MRI data

Following previous studies (Viviano and Schneider, 2015), I identified the position of the whole LGN in individual subjects based on the PD-weighted image averaged across multiple acquisitions (Fig. 2.1.1). I manually delineated the whole LGN based on visible intensity difference between LGN and neighboring tissues (surrounding white matter and CSF) using ITK-snap tool (http://www.itksnap.org/; Fig. 2.1.1B). The delineation was performed in a series of coronal sections of PD-weighted images, which have the highest spatial resolution as compared with axial and sagittal sections. This whole LGN region-of-interest (ROI) was used for subsequent analysis to classify M and P subdivisions using MTV.

2.2.5 Parcellation of the LGN based on MTV and other structural MRI maps

I first rank-ordered all voxels within the whole LGN ROI based on their MTV fractions. Since previous histological studies have shown that P-subdivision has higher neuronal cell density (Hassler, 1966; Yücel et al., 2000, 2003) and greater myelin content (Pistorio et al., 2006), I hypothesized that P-subdivision has larger MTV fractions as compared with M-subdivision. Therefore, I classified 20% voxels with the lowest MTV fraction as the putative M-subdivision and the remaining 80% voxels as the putative P-subdivisions (Fig. 2.2.1). This ratio is based on the reported volumes of LGN subdivisions in previous human histological studies (Andrews et al., 1997; Selemon and Begovic, 2007) and was used in a previous fMRI study (Denison et al., 2014). Fig. 2.2.1 depicts examples of MTV-based LGN parcellation in representative hemispheres.

I also attempted to parcellate LGN based on image intensity of non-quantitative structural MRI maps (PD-weighted image and T1-weighted/T2-weighted ratio map). For PD-weighted image, I classified 20% of voxels with the highest image intensity to the putative M-subdivision and the remaining 80% of voxels as the putative P-subdivisions since image contrast of PD-weighted has an opposite trend from that of MTV maps. For the T1-weighted/T2-weighted ratio map, I used the identical criteria as used for MTV.

2.2.6 Histological data (BigBrain) analysis

In order to compare the MTV-based parcellation of LGN subdivisions with histological definition, I analyzed publicly available BigBrain data (100 µm version of the BigBrain 3-D Volume Data Release 2015 in MNI space from https://bigbrain.loris.ca; Amunts et al., 2013). In brief, BigBrain is a three-dimensional reconstruction data of 7404 histological sections of one post-mortem human brain and provides high-resolution anatomical data aligned with MNI coordinate space. In this database, all six layers in human LGN are visible (see Fig. 2.2.3).

I performed manual segmentation of M- (layer 1-2) and P-subdivisions (layer 3-6) of human LGN on BigBrain data. I used this M- and P-subdivision definition from BigBrain as a reference for a comparison with MRI-based parcellation. Example of manual segmentation on BigBrain data is shown in Fig. 2.2.3.

2.2.7 Comparison between MRI data with histological data

In order to quantify the spatial organization of the M and P subdivisions, I calculated the spatial centers of both subdivisions in MRI and histological data, following the analysis used in a previous fMRI study (Denison et al., 2014). The 3D spatial centers of M and P subdivisions were defined as the mean voxel coordinates in each spatial dimension (anterior-posterior, dorsal-ventral, and left-right) in MNI space. While I co-registered a reference (T1-weighted) image to MNI space, human thalamic nuclei have individual differences in their positions, volume and shape (Csernansky et al., 2004). Therefore, the position of LGN and its subdivision in the MNI coordinate is variable across individual brains. I thus calculated the relative positions of the centers of each LGN subdivisions with respect to the widths of LGN on each spatial dimension, for comparisons of LGN subdivision between datasets and brains (Denison et al., 2014).

2.2.8 Functional MRI data acquisition

All subjects took part in an additional fMRI experiment investigating stimulus selectivity on LGN voxels. I performed fMRI acquisition with 1.5 mm isotropic voxels for 10 participants (S1-S10) and 2 mm isotropic voxels for 5 participants (S11-S15).

Acquisition parameters.

fMRI data were acquired with an interleaved T2* weighted gradient echo sequence at voxel size of 1.5 or 2.0 mm isotropic by using simultaneous multi-slice EPI sequence (TR, 2250 ms; TE, 40 ms; flip angle, 75°; in-plane field of view [FoV], 192 × 192 mm) provided by the Center for Magnetic Resonance Research, Department of Radiology, University of Minnesota (https://www.cmrr.umn.edu/multiband/) (Moeller et al., 2010). Slices were transverse axial (57 slices for 1.5 mm and 50 slices for 2.0 mm) with no gap and were oriented to cover LGN and occipital lobe. Some other acquisition parameters also differed between 1.5 mm^3 and 2 mm^3 voxel size acquisitions (multi-band factor, 3; acquisition matrix, 128 × 128; echo spacing, 0.93 ms; partial Fourier, 6/8 for 1.5 mm^3 voxel acquisition for 1.5 mm^3; multi-band factor, 2; acquisition matrix, 96 × 96; echo spacing, 0.68 ms; partial Fourier was not applied for 2 mm^3), while other parameters were identical.

Stimuli, block design and task.

All visual stimuli were generated by using Psychtoolbox 3 in MATLAB (http://psychtoolbox.org/). Stimuli were projected from a projector (WUX5000, Cannon) located outside the scanner room and reflected via a mirror onto a gamma-corrected translucent screen positioned over the subject's head. Gamma-correction was applied using Mcalibrator2 (Ban and Yamamoto, 2013; https://github.com/hiroshiban/Mcalibrator2). Stimuli were presented on a full-flat screen (416 mm × 222 mm) at a spatial resolution of 1920 × 1200 and a frame rate of 60 Hz. The screen was viewed via a mirror mounted over the subject's eyes. The viewing distance and visual angle of the screen was 92 cm and 41.2 ° × 25.8 °, respectively.

I adapted two types of stimuli (M-type and P-type stimulus; Fig. 2.4.1A) designed to elicit selective BOLD responses in M and P subdivisions (Denison et al., 2014); https://github.com/racheldenison/MPLocalizer). M-type stimulus was a 100% contrast, black-white grating with low spatial frequency (0.5 cycles per degree) and higher flicker frequency (15 Hz). P-type stimulus was near-isoluminant (see below) red-green grating with higher spatial frequency (2 cycles per degree) and lower flicker frequency (5 Hz). The orientation of the grating (0°, 30°, 60°, 90°, 120°, or 150°) was changed per every 3 seconds in a random manner. Prior to the fMRI experiment, I adjusted luminance of P-type stimuli in order to make it perceptually isoluminant using a flicker method (Ives, 1912; Minami and Amano, 2017).

I used block design for fMRI experiment, in which each run comprised 15 blocks (6 blocks for each of the M- or P-type stimuli and 3 blocks with blank screen). The duration of each block was 20.25 seconds (18 seconds for stimulus presentation and 2.25 seconds for blank period, during which subjects made responses). During each block, subjects were instructed to count the number of the randomly presented targets, two-dimensional Gaussian contrast decrement within stimuli, while maintaining fixation. During the blank period, subjects reported how many targets they had seen during a previous stimuli block by pressing a button. Subjects completed 7-8 runs. This procedure Other details of the stimuli, task and the block design were described in a previous fMRI study (Denison et al., 2014).

2.2.9 Functional MRI data analysis

Functional MRI data were analyzed using MrVista (https://github.com/vistalab/vistasoft). I registered fMRI data into T1-weighted MRI data to ensure comparisons with other MRI dataset. I corrected the slice timing to match the multi-slice acquisition order. Data was then corrected for the subject's motion within and between scans. I fitted a general linear model (GLM) consisting of predictors (M type and P type stimuli were regressors) convolved with hemodynamic response function (HRF; Boynton et al., 1996) to the time course of each voxel. I used Boynton HRF in order to match a procedure with a previous fMRI study (Denison et al., 2014). By fitting the HRF model to the time series of BOLD responses, I estimated the beta values for the M and P type stimuli. I then calculated the difference between them ($\mathrm{beta}_{\mathrm{M-P}}$):

$$\mathrm{beta}_{\mathrm{M-P}} = \mathrm{beta}_{\mathrm{M}} - \mathrm{beta}_{\mathrm{P}} \qquad (1)$$

I used $\mathrm{beta}_{\mathrm{M-P}}$ as an index for evaluating stimulus selectivity of LGN subdivisions identified by qMRI. I averaged $\mathrm{beta}_{\mathrm{M-P}}$ across all voxels in each LGN subdivisions parcellated on the basis of MTV maps. Finally, I compared $\mathrm{beta}_{\mathrm{M-P}}$ between MTV-based M- and P-subdivisions to evaluate consistency between stimulus selectivity of BOLD responses and MTV-based parcellation of LGN subdivisions.

2.2.10 Test-retest reliability analysis

In order to assess the reproducibility of the MTV measurements and MTV-based LGN parcellation, I re-measured qMRI of thirteen participants (mean age, 23.85; five female). The data acquisition and analysis procedure of qMRI retest data is identical to those in the main experiments. I evaluated the reproducibility of MTV measurements within the LGN by calculating the inter-voxel correlation coefficient (R) between test and retest data. I also quantify the reproducibility of MTV-based LGN parcellation, by calculating the proportion of voxels which were classified into the same subdivisions between test and retest data, among all LGN voxels. I evaluated statistical significance on this proportion based upon comparison with a null distribution, which was obtained by shuffling the labelling of M and P voxels for

10,000 times and calculating the distribution of proportions of voxels classified into the same subdivisions between test and shuffled data. Finally, I also performed the spatial comparisons between retest data and BigBrain data using the same procedure used for the test data.

2.3 Results

I identified the whole LGN in individual subjects using PD-weighted image (Viviano and Schneider, 2015). I then used MTV maps (Mezer et al., 2013) to identify LGN subdivisions in a single-subject level. I evaluated the validity of MTV-based parcellation of human LGN by comparison with histological data from BigBrain (Amunts et al., 2013) and with functional MRI data collected from identical subjects. I also tested the validity of LGN parcellation obtained from other types of structural MRI images. Finally, I evaluated test-retest reliability of MTV-based parcellation of human LGN.

2.3.1 LGN in PD-weighted image

In all individual hemispheres, position and shape of the whole LGN was visible in PD-weighted images (Fig. 2.1.1A), as reported in a previous work (Viviano and Schneider, 2015). We delineated the whole LGN in all individual hemispheres, by manual inspection of PD-weighted images (Fig. 2.1.1A-2.1.1B; see Materials and Methods). Figure 2.1.2 depicts volume of whole LGN in all individual hemispheres. LGN volume identified from BigBrain histological data (Amunts et al., 2013) and previous structural MRI works (Mcketton et al., 2014; Giraldo-Chica and Schneider, 2018) were also shown. Among 15 subjects tested in this study, the mean (± s.e.m.) volume of the whole LGN was 153.48 mm^3 ± 2.32 mm^3 and 158.40 mm^3 ± 1.83 mm^3 in the left and right hemispheres, respectively. The LGN volume manually identified from PD-weighted images are overall consistent with that of BigBrain (168.65 mm^3 and 162.37 mm^3 in left and right hemispheres, respectively) and previous structural MRI work on the basis of similar PD-weighted MRI data (Mcketton et al., 2014; Giraldo-Chica and Schneider, 2018) (Figure 2.1.2). The right LGN was slightly larger than the left LGN (d' = 0.608, t_{14} = 2.136, p = 0.0508, a paired t test). I note that M and P subdivisions cannot be identified by visual inspections of the PD-weighted image.

2.3.2 M and P subdivisions identification from MTV fraction

I then analyzed MTV maps (Mezer et al., 2013) co-registered with PD-weighted images in each individual subject (Fig. 2.1.1C). In all individual hemispheres, I observed gradual changes of MTV fractions within LGN ROIs (Fig. 2.1.1D); the superior-lateral part of the LGN has a higher MTV fraction than inferior-medial part. The distribution of MTV (pooled across subjects) did not exhibit clear multiple peaks (Fig. 2.1.3), which made it difficult to determine a threshold value of MTV to separate M and P subdivisions. The gradual MTV change within LGN was likely due to a limited spatial resolution of *in vivo* qMRI measurements in this study (voxel size: 1 mm isotropic). I here parcellated human LGN, by incorporating prior knowledge from anatomical study demonstrating that the area size of P subdivisions is roughly four times larger than that of M subdivision (Andrews et al., 1997). Based upon this knowledge, I classified the 20% of voxels with the lowest MTV to the putative M-subdivision and the remaining 80% of voxels to the putative P-subdivisions (Fig. 2.2.1; see Figs. 2.2.3 and 2.2.4 for results in other representative subjects; see Figure 3-S3 for results with different M/P ratio definition). As expected from the gradual difference in MTV fractions, voxels classified as putative M-subdivision appears at inferior-medial part whereas voxels classified as putative P-subdivision appeared at superior-lateral part. I also note that these M- and P-subdivisions are identified as distinct two clusters of voxels which are highly continuous across slices in most hemispheres (Figs. 2.2.2 and 2.2.3).

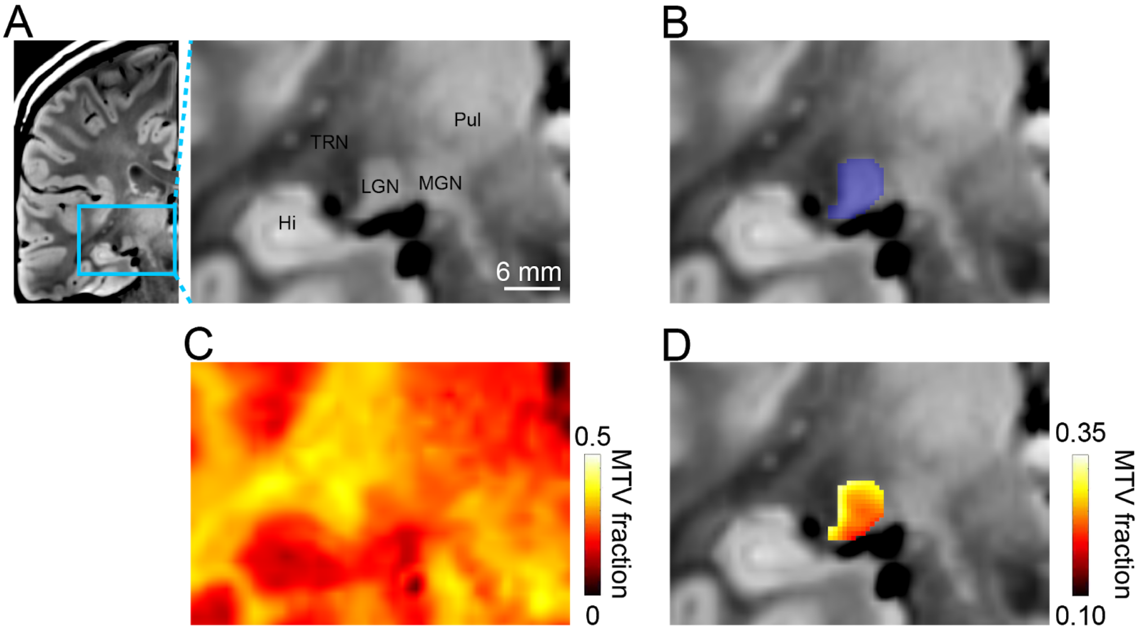

Figure 2.1.1 Procedure for identifying the whole LGN and LGN subdivisions in a single human subject from structural MRI data. (A) A coronal section of Proton density (PD)-weighted image in a representative subject (left hemisphere, Subject S10). *Left panel,* the coronal PD-weighted image of the whole left hemisphere. The cyan rectangle indicates the region magnified in the right panel. *Right panel,* the magnified PD-weighted image near the LGN. TRN, thalamic reticular nucleus; Hi, hippocampus; MGN, medial geniculate nucleus; Pul, pulvinar. The scale bar (while line) indicates 6 mm. (B) ROI covering the whole LGN (translucent blue), which was manually defined from the PD-weighted image. (C) Macromolecular tissue volume (MTV) map coregistered with the PD-weighted image. The hot color map corresponds to MTV fractions in individual voxels. (D) MTV fractions within the LGN ROI. MTV fraction gradually changed along the superior-inferior and lateral-medial axis. Note that the scale of the MTV fraction differs from that of panel C.

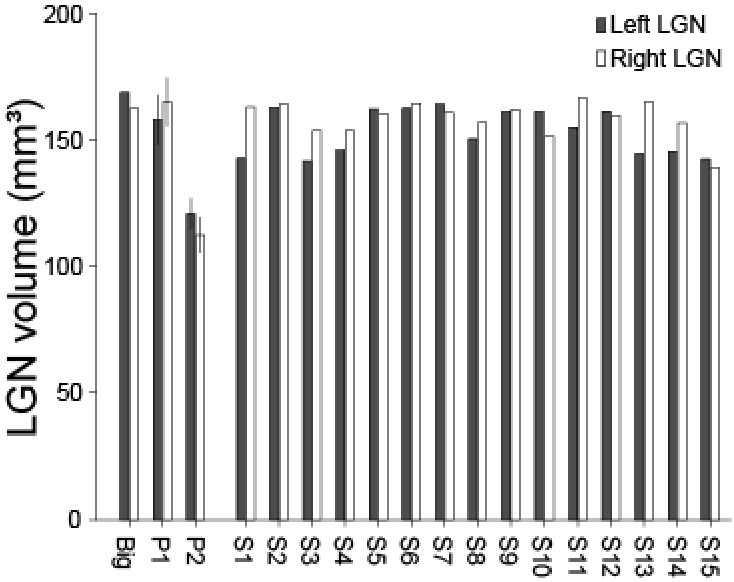

Figure 2.1.2: The LGN volume estimated in the current study and previous anatomical and neuroimaging studies. The gray and white bars depict the LGN volumes of the left and right hemispheres, respectively. The LGN volumes in this study (*N* = 15, from S1-S15) are within the range of the BigBrain (Big, left end) and previous structural MRI works (P1, Mcketton et al., 2014 and P2, Giraldo-Chica et al., 2018). I note that both P1 and P2 data is taken from the data collected from healthy control subjects in each paper. Error bars depict ±1 S.E.M.

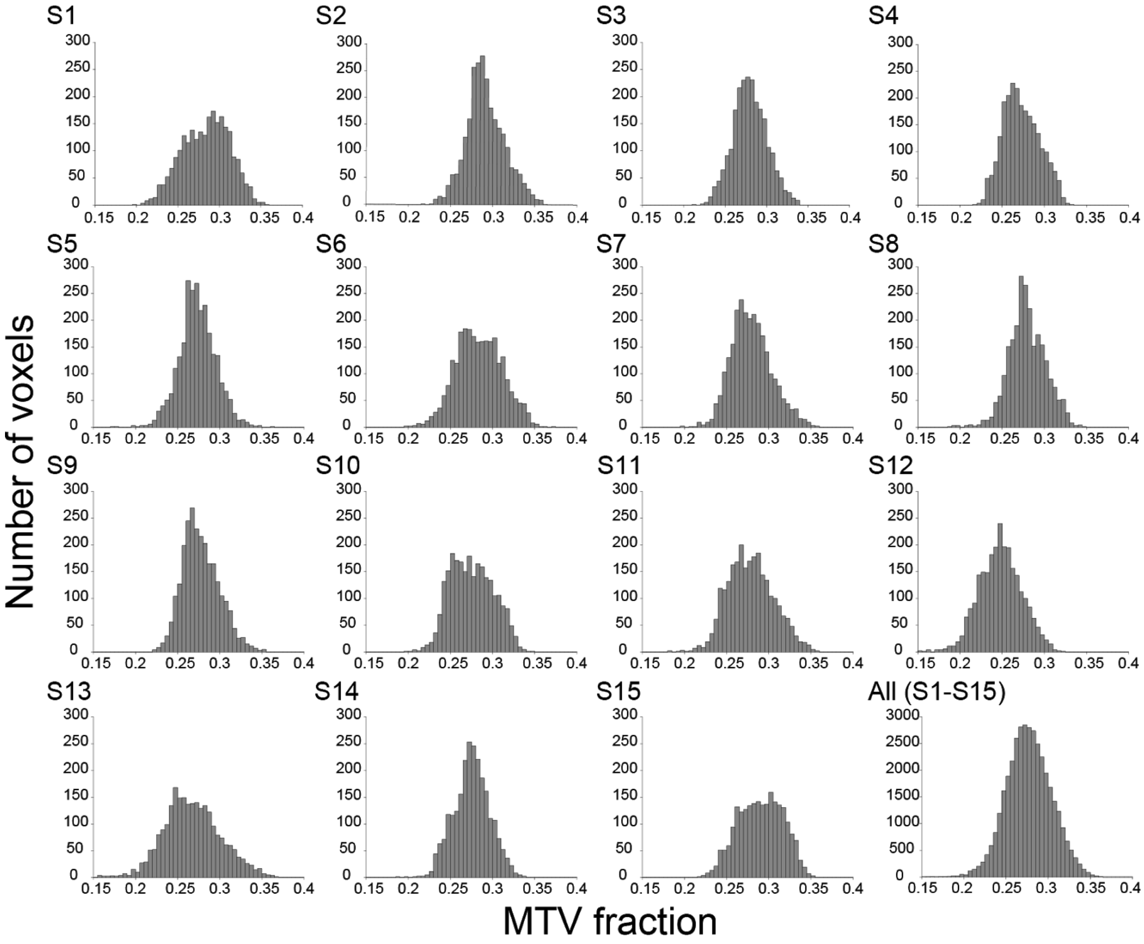

Figure 2.1.3: The histogram of MTV fraction in all LGN voxels for all subjects (S1-S15) and those pooled across subjects. The horizontal axis represents MTV fraction and the vertical axis represents the number of voxels. Bin widths are 0.005. I did not find a visible bimodal distribution of MTV fraction within the LGN ROI.

Figure 2.2.1. LGN subdivisions parcellated by MTV fraction on a series of coronal sections in a single representative hemisphere. (A) MTV fractions in LGN ROI overlaid on a series of coronal sections of PD-weighted image (the left and right panels represent anterior and posterior sections; distance between sections: 0.5 mm) in a representative hemisphere (left hemisphere, subject S10). The conventions are identical to those used in Figure 1D. (B) M- and P-subdivisions estimated from MTV fractions in the hemisphere shown in panel A. I classified 20% voxels with the lowest MTV fractions as M-subdivision (dark red), and the remaining 80% voxels as P-subdivision (light green). The scale bar indicates 4 mm.

Figure 2.2.2: LGN subdivisions parcellated by MTV in the left hemispheres of all subjects. M and P subdivisions identified by MTV in all subjects (N=15) were overlaid on a series of coronal sections of PD-weighted images (left: anterior section; right: posterior section; distance between sections: 0.5 mm). Conventions are identical to those used in Figure 2B.

Figure 2.2.3: LGN subdivisions parcellated by MTV in the right hemispheres of all subjects. Conventions are identical to those used in Fig. 2.2.1B and 2.2.2.

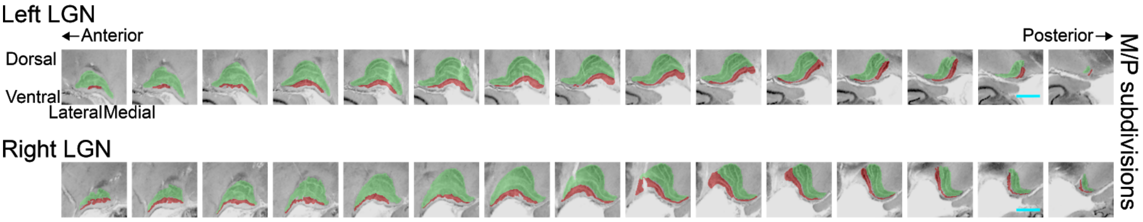

Figure 2.2.4: LGN subdivisions on a series of coronal sections in the BigBrain. M (translucent red) and P subdivisions (translucent green) manually identified from BigBrain data (upper panel, left hemisphere; lower panel, right hemisphere). The cyan scale bar indicates 4 mm, and the distance between sections was 0.5 mm. Other conventions are identical to those used in Fig. 2.2.1.

2.3.3 Validations of M and P subdivisions in MRI data

I evaluated the validity of MTV-based LGN parcellation by comparing with the histological data on human LGN subdivisions (Fig. 2.2.4). To do so, I calculated the centers of coordinates among all M- and P-subdivision voxels classified based on MTV in all hemispheres (Denison et al., 2014), and compared them with those of BigBrain data (Fig 2.3.1; Fig. 2.3.2). In BigBrain, center of M subdivision was located in medial, posterior and ventral part of the LGN, while center of P division was located in lateral, anterior and dorsal part (dashed lines and open circles in Fig. 2.3.1 and Fig. 2.3.2). I found that the center of coordinates of M- and P-subdivisions defined by *in vivo* MTV data showed a similar trend as BigBrain data, and this trend was well replicated across all subjects (solid lines and filled circles in Fig. 2.3.1 and Fig. 2.3.2). Therefore, this result suggests that LGN subdivisions identified from MTV have a good agreement with anatomical architecture of histological human LGN data.

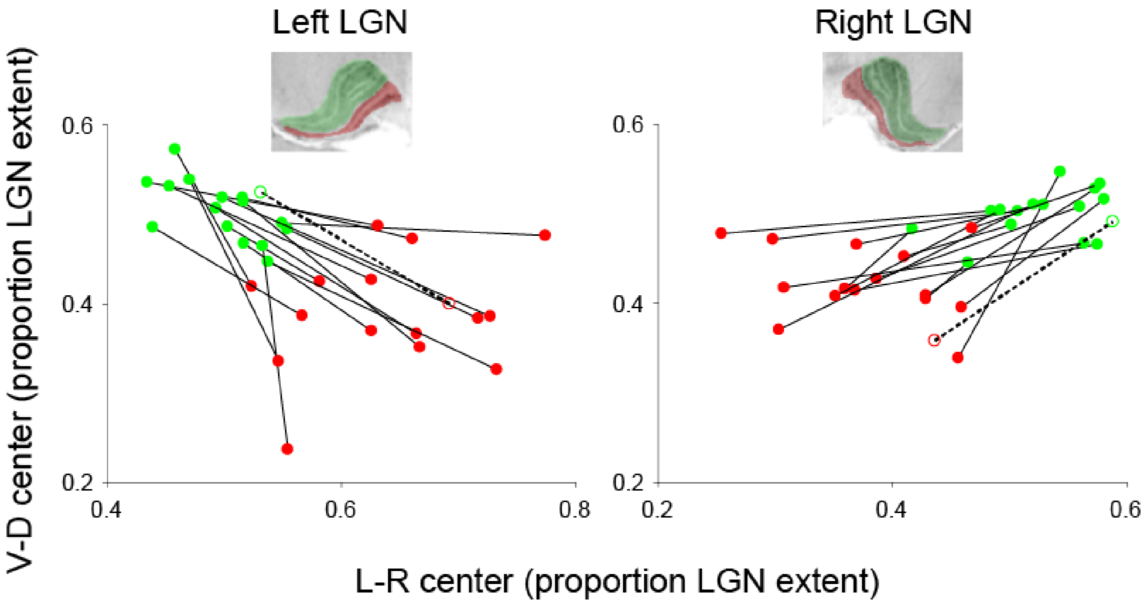

Figure 2.3.1: Center positions of MTV-based M- and P-subdivisions, compared with BigBrain data. The horizontal and vertical axis depicts the center position for M (red) and P subdivisions (green). The horizontal and vertical axes represent left-right and ventral-dorsal axes, respectively (Denison et al., 2014). M and P subdivisions identified in a representative coronal slice of the BigBrain are inserted in each panel. The center positions were calculated in MNI coordinates and are plotted as a proportion of the extent of each subject's entire LGN along a given axis. Filled circles and solid lines are spatial centers of M- and P-subdivisions estimated from MTV map. Open circles and dotted lines are spatial centers of M and P subdivisions in a human histological dataset (BigBrain; Amunts et al., 2013). I found that the centers of M voxels defined from MTV are located more medially and ventrally as compared with P-voxels in all hemispheres, in a consistent manner with the BigBrain histological data.

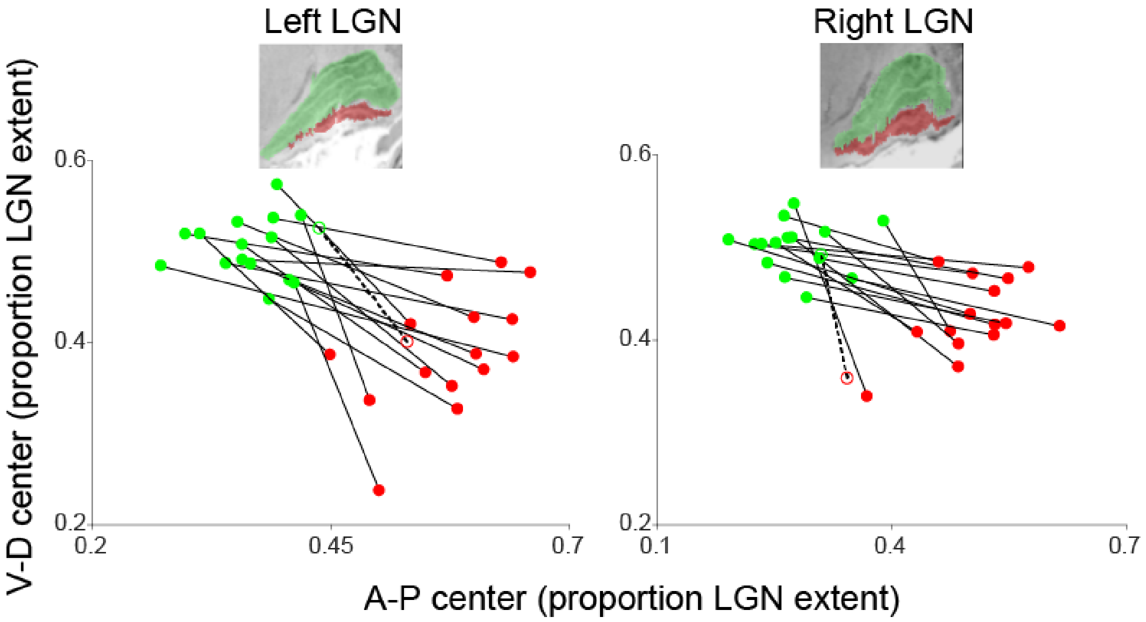

Figure 2.3.2: Center positions of MTV-based M- and P-subdivisions, compared with BigBrain in the anterior-posterior/ventral-dorsal axis. Horizontal and vertical axes represent anterior-posterior and ventral-dorsal axes, respectively. M and P subdivisions identified in a representative sagittal slice of the BigBrain are inserted in each panel. Other conventions are identical to those used in Fig. 2.3.1.

I replicated MTV-based parcellation results using two different definitions of volume ratio between M and P subdivisions (M:P ratio = 19.0:81.0 or 28.9:71.1) in order to test how much arbitrary choice of fixed volume ratio in the main analysis (1:4; (Denison et al., 2014) affects validity of MTV-based parcellation. These two ratios correspond to the minimum and maximum proportion of M subdivisions across brains reported among a previous post-mortem studies (Andrews et al., 1997) and the current investigations on BigBrain data. I found that the overall pattern of MTV-based parcellation was well preserved in this analysis, suggesting that as far as I used the volume ratio within a range reported in anatomical study, I could obtain similar MTV-based LGN parcellation in a consistent manner with histological data (Fig. 2.3.3).

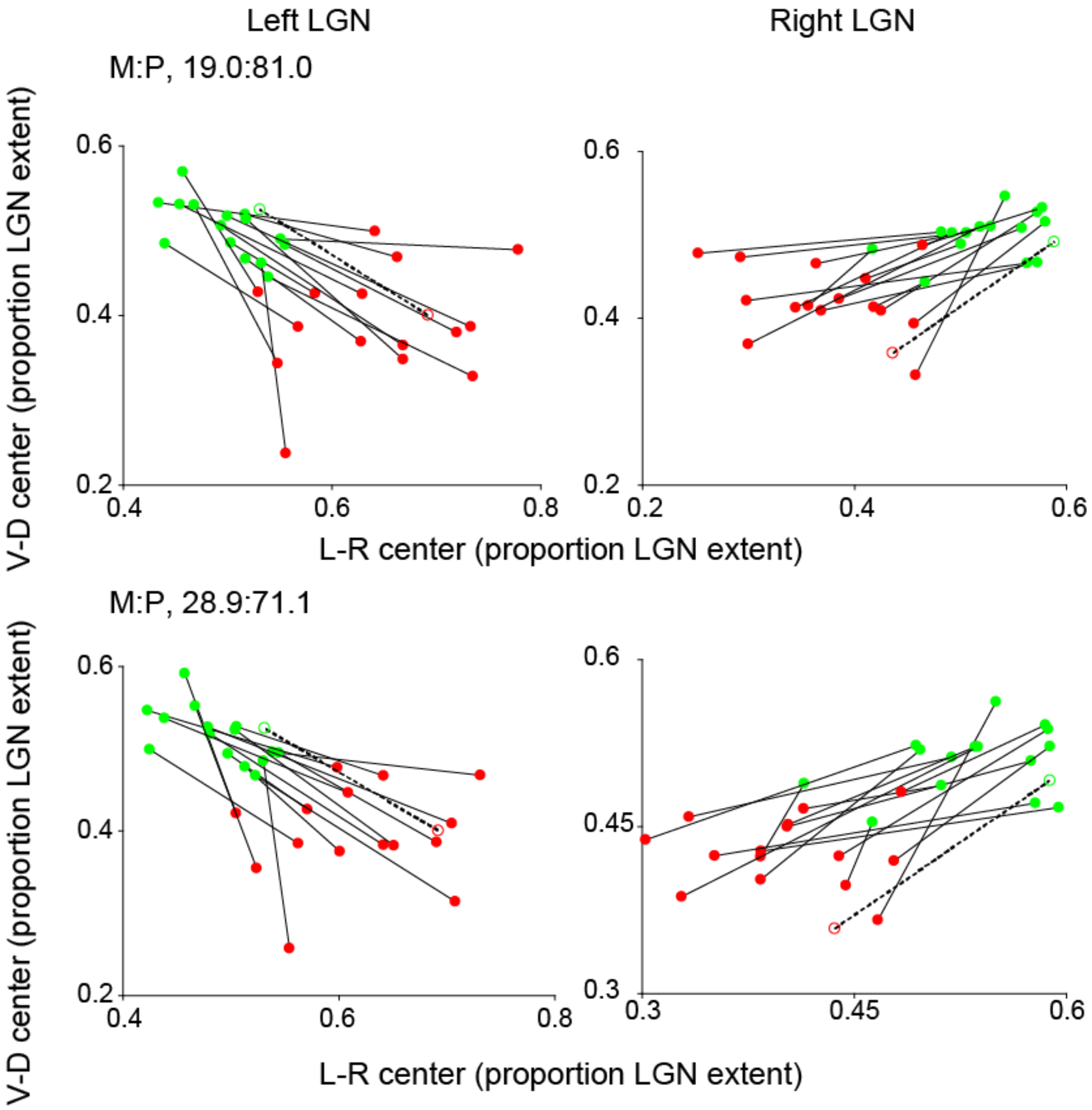

Figure 2.3.3: MTV-based parcellation was robust against the ratios of M and P subdivisions. The plots depict the center of M and P subdivisions estimated by MTV fractions with different M:P ratios from the main analysis (top panels, M: 19.0%; bottom panels, M: 28.9%). These two ratios correspond to the minimum and maximum proportion of M subdivisions across brains reported among a previous post-mortem studies (Andrews et al., 1997) and the investigations on BigBrain data. The conventions are identical to those used in Fig. 2.3.1.

2.3.4 Different visual sensitivity in MTV-based M and P subdivisions

Using fMRI, I further tested whether M and P subdivisions identified from MTV showed different visual stimulus sensitivities that are reported in previous macaque and human studies (Derrington and Lennie, 1984; Usrey and Reid, 2000; Denison et al., 2014; Zhang et al., 2015, 2016). I measured BOLD responses to a pair of visual stimuli designed to activate M and P subdivisions differently (Denison et al., 2014) (Fig. 2.4.1A; see *Materials and*

Methods, Functional MRI data acquisition). I examined the extent to which M and P subdivisions defined from MTV show different stimulus selectivity in their BOLD response.

I calculated the difference in beta weights between M and P type stimuli ($\mathrm{Beta}_{\mathrm{Mstim-PStim}}$; positive value indicates BOLD response was greater for M type stimuli) for M and P subdivisions defined from MTV in individual hemispheres (Fig. 2.4.1B). Group analysis showed a significant difference in $\mathrm{Beta}_{\mathrm{Mstim-PStim}}$ between M and P subdivisions (t_{14} = 4.5416, *P* = 0.0005 for left hemisphere; t_{14} = 3.5838, *P* = 0.0030 for right hemisphere, a paired t-test). Consistency with known stimulus selectivity in M and P subdivisions further support that MTV-based parcellation provides reasonable *in vivo* identification of LGN subdivisions in individual hemisphere level.

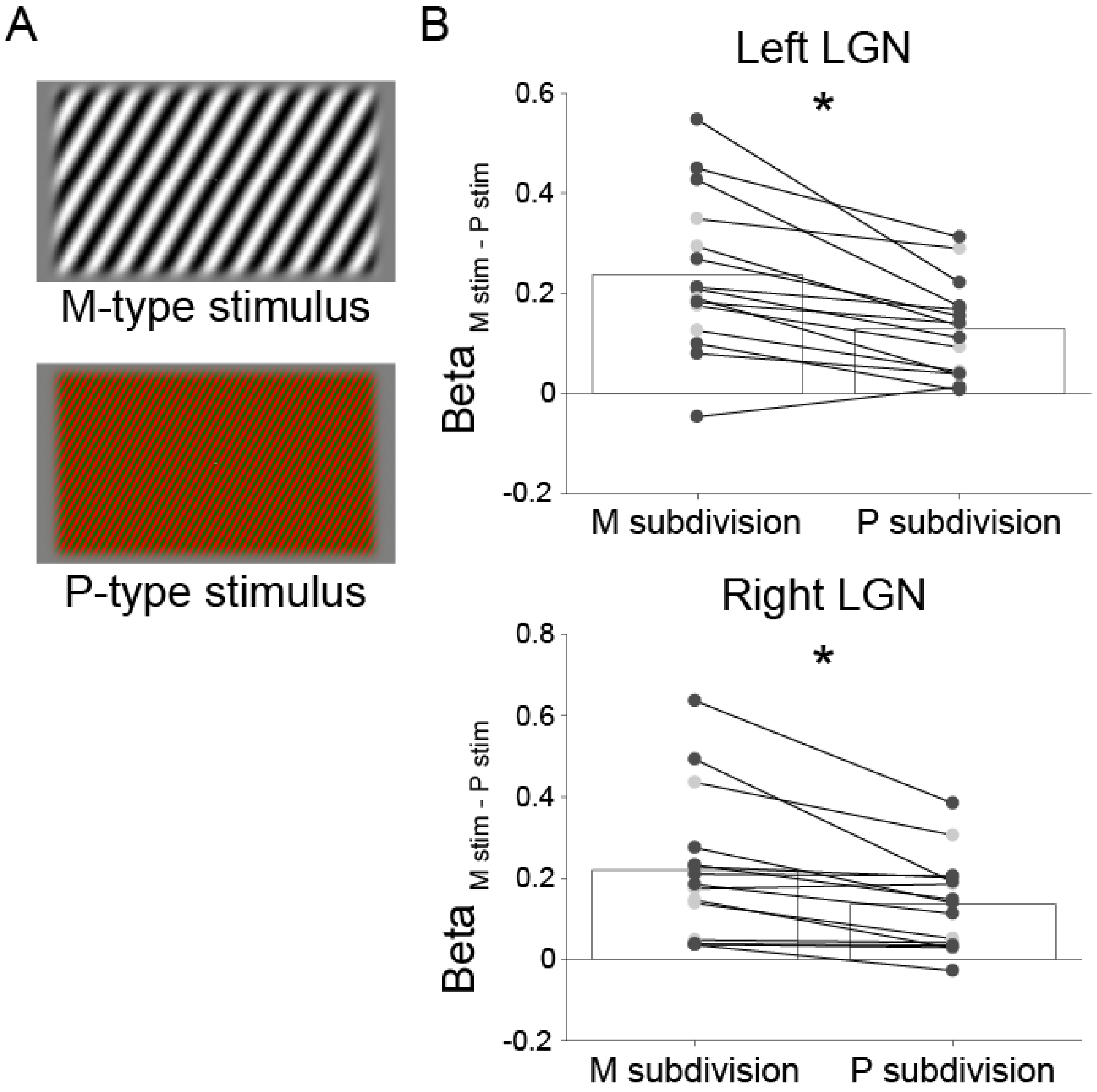

Figure 2.4.1: MTV-based M and P subdivisions show the stimulus selectivity reported in the previous literature. (A) Stimuli used for eliciting differential BOLD responses from voxels with greater M subdivision representation and voxels with greater P subdivision representations. *Upper panel:* Achromatic, low spatial frequency, high temporal frequency, and high luminance contrast grating stimulus used for activating M-subdivisions. *Lower panel:* High color contrast, high spatial frequency, low temporal frequency, and low luminance contrast grating stimulus used for activating P-subdivisions. These stimuli are adapted from Denison et al., (2014). See Materials and Methods for the details of stimuli. (B) Stimulus selectivity measured by fMRI in the MTV-based M- and P-subdivision (*top panel*, left hemisphere; *bottom panel*, right hemisphere; *N*=15 for each). The vertical axis depicts the difference of beta value between M- and P-type stimuli (positive value indicates more selective BOLD responses for M-type stimuli). Dots indicate data in individual hemispheres. Dark and light gray dots represent the measurement with1.5 mm isotropic (S1-S10) and 2.0 mm isotropic (S11-S15) voxels, respectively. Asterisks represent statistically significant difference in stimulus selectivity measured by BOLD response between M- and P-subdivisions (two-sample *t*-test, * < 0.005). Details of fMRI methods are described in *Materials and Methods, Functional MRI data acquisition*.

2.3.5 Inter-subject variability and hemispheric differences of MTV fractions

I examined how much MTV fractions in estimated M and P subdivisions are consistent or variable across healthy subjects participated in this study (Fig. 2.5.1). MTV fractions of estimated M-subdivision were 0.2525 ± 0.0032 and 0.2388 ± 0.0035 for left and right hemispheres (mean ± S.E.M), whereas MTV fractions of estimated P-subdivisions were 0.2923 ± 0.0029 and 0.2782 ± 0.0031 for left and right hemispheres. Therefore, the inter-subject variability of MTV fractions in each subdivision was much smaller than the mean difference between M- and P-subdivisions in healthy subjects. Given small variability in measurements across the healthy population, MTV measurement in LGN can be useful for evaluating how much LGN tissue properties of individuals such as eye-disease patients are deviated from controls.

I found the MTV of the left LGN was significantly higher than that of the right LGN in both M and P subdivisions (M subdivisions, 0.2525 ± 0.0032 and 0.2388 ± 0.0035 in left and right hemispheres [mean MTV ± S.E.M], $d' = 1.0708$, $t_{14} = 4.9078$, $p = 0.0002$, paired t-test; P subdivisions, 0.2923 ± 0.0029 and 0.2782 ± 0.0031 in left and right hemispheres, $d' = 1.220$, $t_{14} = 5.1707$, $p = 0.0001$, paired t-test). These significant hemispheric asymmetries of MTV may not be due to measurement biases present in the entire image, since I did not observe inter-hemispheric MTV difference in whole gray matter and white matter (gray matter, 0.2038 ± 0.0015 and 0.2033 ± 0.0013 in left and right hemispheres, d' = 0.0933, $t_{14} = 0.6404$, $p = 0.5322$; white matter, 0.3069 ± 0.0021 and 0.3073 ± 0.0022 in left and right hemispheres, d' = 0.0533, $t_{14} = 1.3652$, $p = 0.1937$). The asymmetry of MTV suggests that there may be some inter-hemispheric tissue differences in LGN, although the exact microstructural interpretation of this effect should be tested in future works.

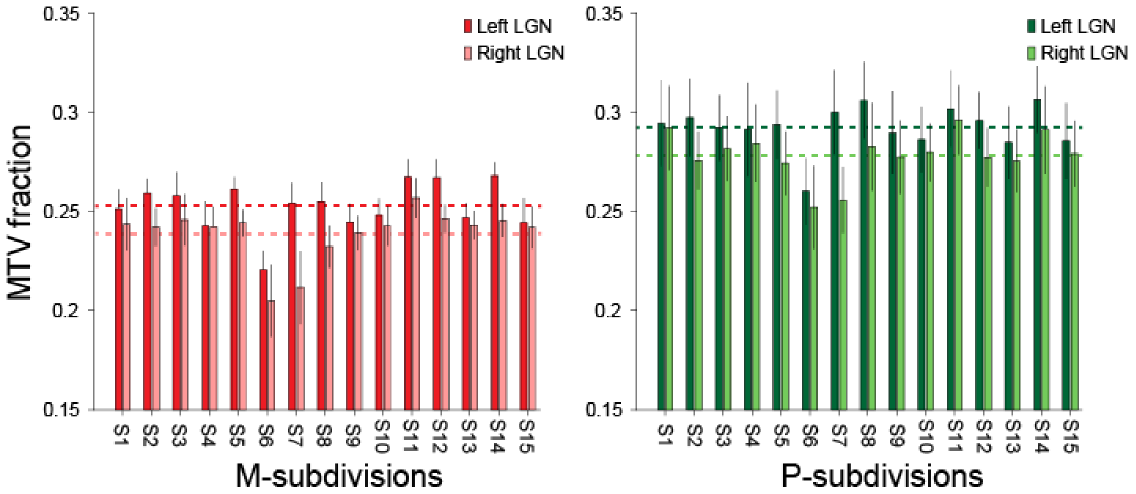

Figure 5: MTV fractions in estimated M- and P-subdivision are overall consistent across healthy subjects. Vertical axis depicts the MTV fraction averaged across voxels within M- (left panel, red) and P-subdivisions (right panel, green) in individual hemispheres. The dark and light bars indicate the MTV fractions of left and right hemispheres, respectively. The thin dotted lines indicate the averages across subjects in each hemisphere. MTV fractions in these subdivisions are overall consistent across 15 healthy subjects. Error bars depict ±1 standard deviation across voxels.

2.3.6 Non-sufficient parcellation of M and P subdivisions base on PD-w and T1-w/T2-w ratio map

MTV is a useful measurement method to provide quantitative measurements on brain tissue properties (Mezer et al., 2013; Duval et al., 2017; Berman et al., 2018). Meanwhile, a number of studies have used other types of MRI-based metrics, such as the ratio between T1-weighted and T2-weighted images (T1w/T2w ratio), to evaluate tissue properties with shorter acquisition time, while measurements are not fully quantitative (Glasser and Van Essen, 2011; Glasser et al., 2016). Therefore, we also tested whether M and P subdivisions can be similarly parcellated using image intensity of other non-quantitative structural MRI data or not, to evaluate a possible advantage of MTV-based approach.

I firstly tested LGN parcellation by using image intensities of PD-weighted images, which was used to identify the whole LGN (Fig. 2.6.1A). I also tested the parcellation using the T1w/T2w ratio map, which have been often used to perform parcellation of cortical areas (Glasser and Van Essen, 2011) (Fig. 2.6.1B). In both cases, I found that coordinates of M- and P-subdivision centers in a majority of subjects showed inconsistent patterns from those in the histological data (BigBrain), suggesting that these maps were not sufficient for parcellating M and P subdivision in LGN. This is most likely because these values are prone to measurement biases (Shams et al., 2019). Unsuccessful parcellation using PD or T1w/T2w maps indicates the advantage for acquiring MTV data for LGN parcellation.

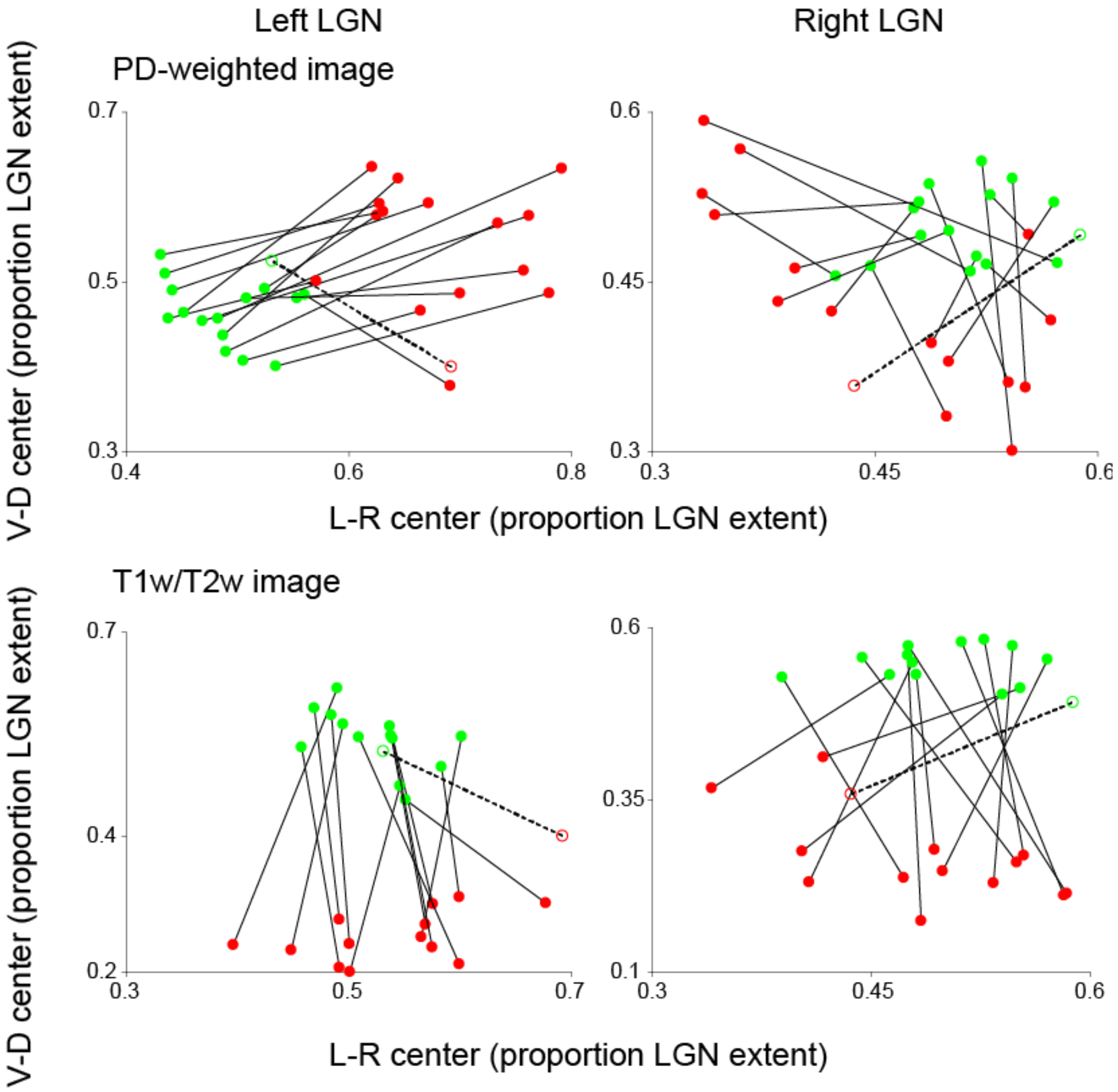

Figure 6: LGN subdivisions may not be identified from non-quantitative structural MRI maps. (A) LGN parcellation performed based on image intensity of PD-weighted image. The centers of M- and P-voxels are varied across hemispheres and inconsistent with the LGN in the BigBrain. (B) LGN parcellation performed based on image intensity of T1w/T2w map. In most hemispheres, center locations along the left-right axis were similar between M and P subdivisions, unlike the BigBrain data. The conventions are identical to those used in Fig. 2.3.1.

2.3.7 Robust parcellation of M and P subdivisions based on MTV

Finally I tested the test-retest reliability of the M and P parcellations by performing the same MTV measurement in 13 subjects on a different day. MTV fractions of voxels within LGN ROI were highly correlated between test and retest experiment (r = 0.78, Fig. 2.7.1A). I then calculated the probability that individual voxel can be classified as the same subdivisions between test and retest experiments. I found that 85.62 and 82.31 % of voxels (left and right

LGN, respectively) were classified as the same subdivision between test and retest data (Fig. 2.7.1B; mean across subjects). In order to assess statistical significance of these numbers, I randomly classified 80% voxels into P subdivisions and remaining 20 % voxels into M subdivisions in order to obtain a null distribution. I repeated this process by shuffling voxels 10,000 times. The maximum probability of voxels classified into the same subdivisions between test data and shuffled data was 71.73 and 71.55 % for left and right hemisphere (mean across subjects), suggesting that the test-retest reliability of MTV-based parcellation was much higher than the significance level ($p < 0.0001$). Finally, I replicated the results that the center of M- and P-subdivisions showed the same spatial pattern as histological data in the retest dataset (Fig. 2.7.1C). Taken together, these results support a considerable degree of reproducibility of the current results on MTV-based LGN parcellation.

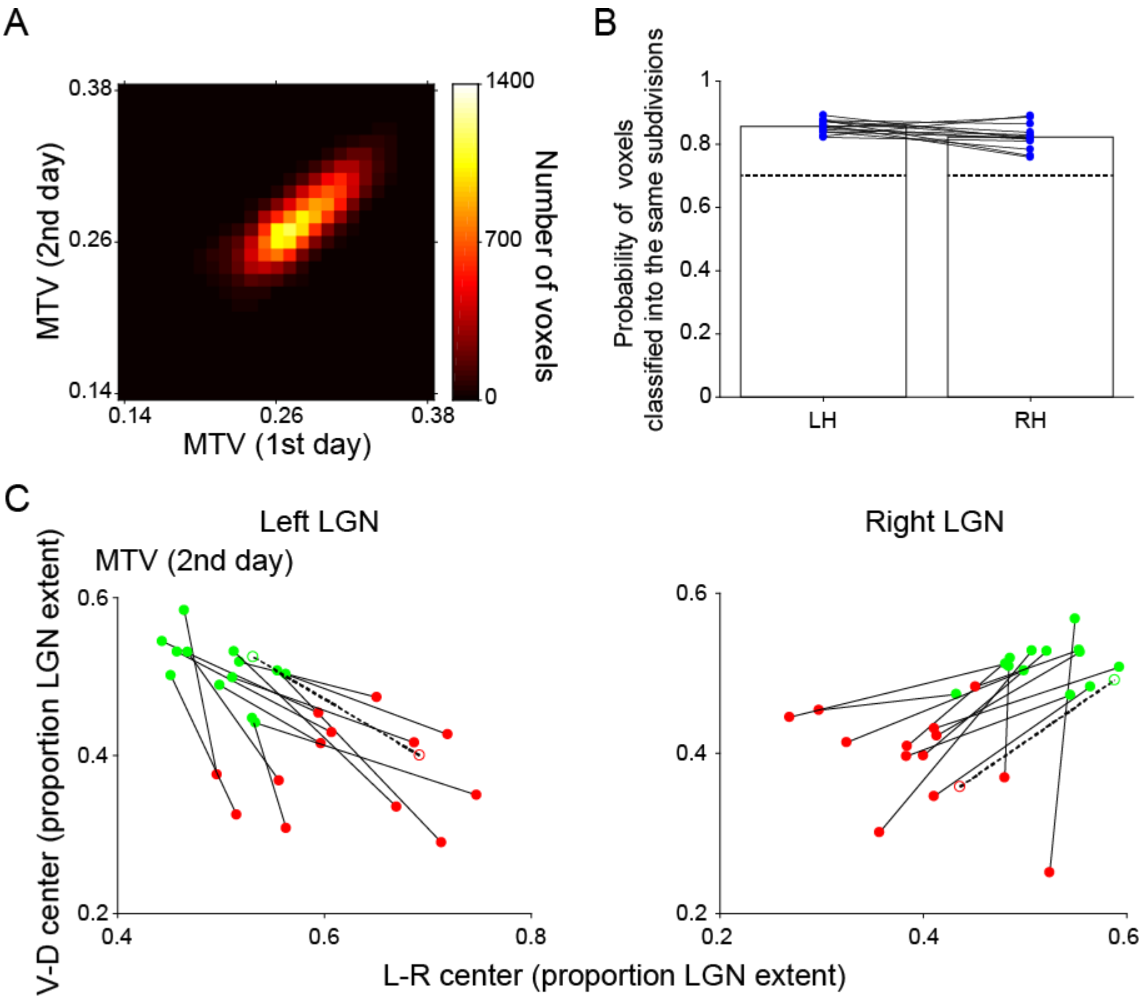

Figure 7: Test-retest reproducibility of MTV-based parcellation. (A) Two-dimensional histogram comparing MTV measurements across days in LGN voxels. The data are derived from LGN voxels pooled across participants, who participated in retest scanning (*N* = 13). Color map indicates the number of voxels. The correlation coefficient of MTV measurements across days was 0.78 ($p < 10^{-10}$). This high correlation coefficient indicates that MTV measurement is reproducible across days. (B) Reproducibility of classification. The vertical axis depicts a probability that individual voxels are classified into the same LGN subdivisions between test and retest dataset. Individual dots depict results in individual hemispheres. The dotted lines depict the maximum probability of voxels classified into the same subdivisions between test and shuffled data, which is equal to $p = 0.0001$. (C) The center of coordinates in M and P subdivisions identified by MTV-based parcellation using retest dataset (filled circles and solid lines). I replicated results with BigBrain data (open circles and dotted line). The conventions are identical to Fig. 2.3.3.

2.4 Discussion

It is widely known that the human LGN consists of functionally and anatomically different subdivisions. However, identifying these subdivisions in individual living human brains using conventional structural neuroimaging methods had been challenging. In this study, I demonstrated the approximate parcellation of LGN subdivisions in a single-subject level, by combining *in vivo* structural MRI methods (multiple PD-weighted imaging and MTV measurement). Spatial positions of identified LGN subdivisions were consistent with those in the postmortem human LGN subdivisions in BigBrain data (Amunts et al., 2013). Furthermore, using fMRI, I confirmed that these subdivisions have different stimulus selectivity, in a consistent manner with previous physiological studies. Finally, I confirmed the MTV-based LGN parcellation is highly consistent across datasets acquired in different days, suggesting that proposed methods are highly reproducible. Other non-quantitative MRI methods did not provide LGN parcellation consistent with neuroanatomical data. Taken together, this study provides evidence on the utility of quantitative structural MRI approach on LGN parcellation, and establishes methods to measure structural properties of human LGN subdivisions in single living human subjects, using clinically feasible 3T MRI scanner.

2.4.1 Microstructural origin of MTV-based parcellation

The current result demonstrated that the MTV fraction can be a useful measurement for distinguishing M and P subdivision. One might ask what types of microstructural differences may lead MTV differences between M and P subdivisions. In principle, MTV quantifies non-water macromolecular volumes on the basis of calibrated quantitative proton density maps (Mezer et al., 2013). Phantom experiments confirmed that MTV measurement correlated with lipid fraction (Mezer et al., 2013; Filo et al., 2019; Shtangel and Mezer, 2020). Still, there is no established theory on how much variance of MTV in a certain brain area can be explained by specific types of microstructural properties. A number of histological studies on non-human primate reported differences in anatomical properties between M and P subdivisions, such as higher neuronal cell density in P subdivision (Hassler, 1966; Yücel et al., 2000, 2003) and greater myelin content in P subdivision (Pistorio et al., 2006). A recent post-mortem human study confirmed that P subdivision has higher neuronal cell and myelin densities as compared with M subdivisions (Müller-Axt et al., n.d.). These results are in line with the current results showing a larger MTV fraction in P subdivision than in M subdivision since both a larger number of cells and greater myelin content will result in larger lipid volume fraction. There remains a possibility that other neurobiological factors such as glial cell density also partly explain the difference in MTV between M and P subdivisions. This remains as an open question for future investigations more directly comparing histology and quantitative MRI maps.

In this study, I also found the significant MTV difference between left and right LGN. To my knowledge, this is the first neuroimaging study showing the inter-hemispheric difference of human LGN tissue properties. While speculative, these results may be related to a previous study showing the difference of number of neurons in left and right LGN of rhesus monkeys (Williams and Rakic, 1988). Further histological examination necessary to establish what type of microstructural difference between hemispheres may exist in human LGN.

2.4.2 Advantage of MTV-based parcellation over other structural MRI methods

In a standard practice, many neuroimaging studies have utilized T1-weighted image and/or T2-weighted image to identify the location of cortical area or subcortical nuclei. While the relative values in these images are useful to identify the border between gray matter and white matter, their absolute values can not be interpreted as a quantitative unit since measurements are affected by multiple sources of inhomogeneity such as B1+ inhomogeneity or coil gain bias. Recent development of quantitative MRI method enables us to quantify MRI parameters (such as PD, T1, and T2), which opens the avenue to study tissue properties of the brain across human subjects (Mezer et al., 2013; Weiskopf et al., 2015; Forstmann et al., 2016; Keuken et al., 2017; Cercignani et al., 2018). These quantitative MRI measurements have provided valuable insights on tissue properties of cortical areas (Sereno et al., 2013; Lutti et al., 2014) or white matter (Stuber et al., 2014; Takemura et al., 2019).

Mezer and colleagues (2013) proposed MTV methods, and demonstrated consistency of measurements with lipid volume fractions in the phantom, high test-retest reproducibility, and sensitivity for white matter tissue changes in multiple sclerosis patients. A strong advantage of this method is its independence from static magnetic field strength, since it is based on PD measurements calibrated by assuming that water fraction in CSF voxels equals to 100%. In fact, Mezer et al. (2013) demonstrated that MTV measurements in the brain are consistent across measurements performed by using different hardwares. Therefore, I chose MTV mapping as a method for human LGN parcellation since it is a promising method relatively independent from hardware choices and thus useful for future clinical works.

I found that MTV provides parcellation consistent with histological data (Fig. 2.3.1) and stimulus selectivity known in physiological studies (Fig. 2.4.1). MTV-based parcellation was superior to the parcellation based upon other non-quantitative MRI maps (PD-weighted or

T1w/T2w; Fig. 2.6.1). This is most likely because MTV has been corrected for B1 transmitter (B1+) inhomogeneity, while other maps do not. While T1w/T2w map has been demonstrated to enhance tissue contrast and thus be useful for delineating borders between brain areas (Glasser and Van Essen, 2011) and has advantages in its shorter acquisition time, several studies demonstrated inconsistencies between T1w/T2w and quantitative MRI measurements that are more sensitive to myelin (Arshad et al., 2017; Hagiwara et al., 2018; Uddin et al., 2018). These inconsistencies are most likely due to the fact that T1w/T2w is not calibrated for B1+ inhomogeneity (Glasser and Van Essen, 2011). While I do not fully exclude a possibility that ad-hoc B1+ bias field correction (Glasser et al., 2013) may improve LGN parcellation using T1w/T2w, the current results showed superior performance for LGN parcellation with MTV than with T1w/T2w, most likely because of superior calibrations for B1+ inhomogeneity in the LGN.

2.4.3 Comparison with fMRI-based LGN parcellation

A few fMRI studies have examined the spatial pattern of visually-evoked BOLD signals in the LGN (Denison et al., 2014; Zhang et al., 2015). These studies demonstrated clusters of LGN voxels preferentially responding to distinct types of visual stimuli, in a consistent manner with neurophysiological findings, suggesting that approximate identification of LGN subdivisions in living humans can be achieved by fMRI measurements on visual stimulus sensitivities. Quantitative structural MRI-based parcellation methods as shown in this study have several advantages as compared with the fMRI-based parcellation method. First, the fMRI-based methods require a precise control of stimuli including presentation of isoluminant stimuli (Denison et al., 2014), which is unnecessary in the structural MRI-based methods. Furthermore, use of visual stimuli limits the application for LGN parcellation methods on clinical studies for patients with visual field loss or using MRI scanners where visual stimulus presentation equipment is not available. Second, structural MRI-based methods have higher spatial precision, since voxel size of qMRI measurement (e.g. 1 mm isotropic in this study) is generally smaller than those used in fMRI experiments (e.g. 1.8×1.8×1.5 mm for 3T, 1.2~1.5 mm isotropic for 7T in Denison et al., 2014). For fMRI, large veins passing through multiple voxels can limit spatial specificity of BOLD signal (Uludağ and Blinder, 2018; Kay et al., 2019). Therefore, the current methods have advantage over fMRI-based methods in terms of spatial precision, though fMRI-based methods will surely continue to improve (Huber et al., 2014, 2018b; Kay et al., 2020). Finally, MTV-based parcellation has higher test-retest reliability across days (Fig. 2.7.1), as compared with those reported in a previous fMRI work (r < 0.4; Denison et al., 2014). Therefore, MTV-based parcellation will provide more stable identification for M and P subdivisions in individual living human brains.

2.4.4 Limitations and future directions

In this study, I classified voxels into M and P subdivisions using a fixed volumetric ratio (1:4). However, previous studies reported the inter-subject variability in the ratio of the M and P subdivision volumes in post-mortem human data (Hickey and Guillery, 1979; Andrews et al., 1997). Therefore, it will be ideal to classify LGN voxels into M and P subdivisions by fitting a mixture model composed of two curves with distinct peaks to the distribution of MTV fractions in each individual LGN. However, this approach was not practical in this study due to the fact that MTV distribution of LGN voxels in the current *in vivo* data did not show two distinct peaks which correspond to M and P subdivisions (Fig. 2.1.3). Given that a recent study using a high resolution *ex vivo* quantitative structural MRI (220 μm isotropic) using 7T MRI demonstrated a parcellation of LGN subdivisions using aforementioned curve fitting procedure (Müller-Axt et al., n.d.), I expect that future improvement on the spatial resolution of i*n vivo* quantitative MRI will provide LGN parcellation without assuming a fixed volumetric ratio, enabling quantitative comparisons of M and P subdivisions volumes across subjects.

The other limitation of the MTV-based parcellation method proposed in this work is a relatively long acquisition time. The current identification method requires multiple structural image acquisitions, each of which require considerable acquisition time (60-90 and 28 min for PD-weighted image and quantitative structural MRI, respectively) in order to ensure higher signal quality at the LGN and quantification of MTV (Mezer et al., 2013; Mcketton et al., 2014; Giraldo-Chica et al., 2015; Viviano and Schneider, 2015; Giraldo-Chica and Schneider, 2018). While the trade-off between signal quality and acquisition time is inherent to any neuroimaging methods, prolonged acquisition time limits application of MTV-based parcellation to studies on clinical populations. Further development of quantitative MRI method with shorter acquisition time (Warntjes et al., 2008; Marques et al., 2010; Ma et al., 2013; Caan et al., 2019) is essential to increase an opportunity to measure LGN subdivisions in a wide range of populations.

The length of time for the current scanning protocols can be too long compared to scan time in clinical situations. It is a trade-off between time and accuracy, but it can be possible to reduce scanning time. For example, I identify LGN by averaging multiple acquisitions of LGN using PD 2D Turbo Spin Echo (TSE), which is the established method (Mezer et al., 2013; Mcketton et al., 2014; Giraldo-Chica et al., 2015; Viviano and Schneider, 2015;

Giraldo-Chica and Schneider, 2018), but the weak point of 2D imaging is the cross-talk between adjusted slices. I measured at 1.0 mm of slice thickness with no gap, which might have interfered with the contrast to Noise Ratio (CNR) of the image. Although the time per scan of 3D imaging will become longer, the 3D imaging (e.g. 3D-TSE) will improve the CNR of the image, which will result in reducing the required numbers of acquisition.

It is known that thin layers named koniocellular layers (K layers) exist between each layer of M and P subdivisions in the LGN (Guillery and Colonnier, 1970). Previous histological studies showed the K layers have distinct anatomical properties given its smaller cell size compared with M and P subdivisions (Hendry and Clay Reid, 2000). Considering the location of K layers, MTV fractions in many of LGN voxels are likely to be affected by partial voluming between K layers and M/P subdivision. Therefore, a part of variance in structural measurements can be affected by anatomical properties of K layers.

Despite the limitations discussed above, the current study is an important step for establishing a method to parcellate human LGN subdivisions and quantify their tissue properties in living humans brains. Once I could overcome the existing limitation of acquisition time, MTV-based *in vivo* human LGN measurements will open fruitful opportunities for understanding how properties of human LGN are related to brain functions and are affected as a consequence of diseases. For example, psychophysical studies have suggested that properties of M subdivisions will be crucially related to reading performance (Chase and Jenner, 1993; Felmingham and Jakobson, 1995; Demb et al., 1998; Stein, 2001; Main et al., 2014). Similarly, psychophysical investigations on glaucoma patients suggested that M subdivision may be damaged earlier than P subdivisions (Maddess et al., 1992; Cello et al., 2000). Extension of this study will provide a powerful tool to directly compare tissue properties of LGN subdivisions and psychophysical performance measured in identical subjects, and thus to improve our understanding how properties of LGN subdivisions are related to functions and disorders.

Chapter 3.

Structural properties of the vertical occipital fasciculus correlates with the variability in human stereoacuity.

This chapter is adapted from "Microstructural properties of the vertical occipital fasciculus explain the variability in human stereoacuity." Proceedings of National Academy of Sciences of the United States of America, National Academy of Sciences, 115 (48), 12289-12294, 2018, Hiroki Oishi, Hiromasa Takemura, Shuntaro C. Aoki, Ichiro Fujita, Kaoru Amano.

3.1 Introduction

Stereopsis is a fundamental human visual function that has been studied over two centuries (Wheatstone, 1843; Julesz, 1971; Howard and Rogers, 1995). Traditional visual neuroscience has focused on the properties of neural response towards important cues for the stereopsis, such as binocular disparity, to understand the neural computation achieving the perception of three-dimensional world (Parker, 2007; Welchman, 2016). A series of studies have revealed a number of cortical areas involved in binocular disparity processing (Janssen et al., 1999; Orban et al., 2006; Parker, 2007; Welchman, 2016) and demonstrated that dorsal and ventral visual areas have complementary roles in processing different aspects of stereoscopic information (Neri et al., 2004; Uka and DeAngelis, 2006a; Shiozaki et al., 2012a; Chang et al., 2014).

However, there is one key question that remains unanswered: why does the ability to discriminate depth (stereoacuity) vary among people. In fact, a number of psychophysical studies have reported a broad and often bimodal distribution of human stereoacuity, which are much less evident than other visual modalities (Richards, 1970; Movshon et al., 1972; Zaroff et al., 2003; Hess et al., 2015). The neurobiological origin of such large differences in perceptual performance is unknown.

As I mentioned above, several visual areas in both dorsal and ventral pathways are known to be involved in stereo perception and each pathway has complementary aspects for stereopsis. For example, absolute disparity is represented in the dorsal visual areas while relative disparity processing is represented in the ventral visual areas (Neri et al., 2004). While this suggests the distinct representation between dorsal and ventral pathways, the depth discrimination acuity for the absolute disparity and that for the relative disparity of humans is marginally correlated (Chopin et al., 2016). Based on the complementary representations of absolute and relative disparity in dorsal and ventral pathways but with perceptual correlation between them, I hypothesised the dorsal and ventral pathways communicate with each other during stereopsis. The anatomical properties of the white matter tract that supports communication between the dorsal and ventral areas should thus be crucial. VOF (Yeatman et al., 2014b; Takemura et al., 2016c, 2017), which connects dorsal and ventral visual cortices, can be one of the candidates for the tracts responsible for the dorso-ventral communication.

Here, I have combined modern structural neuroimaging techniques (diffusion MRI and MTV) with psychophysical measurements to assess human stereoacuity, and attempted to clarify how the tissue properties of visual white matter tracts may relate to the stereoacuity. In addition, I have evaluated the relationship between the endpoints of the tracts and areas activated by the same stereo stimuli using fMRI. Furthermore, I tested how these tissue properties relate to the contrast detection threshold to test whether the observed relationship between anatomical and psychophysical measurements are specific to stereoacuity.

3.2 Materials and Methods

3.2.1 Participants

Twenty-three healthy volunteers (19 males and 4 females; mean age 26.1 years) participated in the study. All participants had normal or corrected-to-normal vision. All individual participants gave written informed consent to take part in this study, which was conducted in accordance with the ethical standards stated in the Declaration of Helsinki and approved by the local ethics and safety committees at Center for Information and Neural Networks (CiNet), National Institute of Information and Communications Technology.

3.2.2 Psychophysical measurement and analysis of stereoacuity experiment

Participants.

Nineteen participants underwent an experiment to determine their stereoacuity (16 males and 3 females; mean age 25.0 years old). All participants had no diagnosis history of eye diseases. For each participant, all procedures in this experiment took around 80 minutes.

Apparatus.

The stereoacuity experiment employed a haploscope in which each eye viewed a half side of the monitor through an angled mirror and a front triangular prism mirror. RDSs were presented with a spatial resolution of 3840 × 2160 pixels at a frame rate of 60 Hz on a gamma-corrected, full-flat 4K LCD monitor (P2715Q, Dell, USA). The distance from the angled mirror to the prism mirror was 10 cm and the direct distance from a display to chin support was 160 cm, i.e., the viewing distance was 170 cm. Each side of the monitor covered a visual angle of 10.0°× 11.3°.

Stimuli.

An RDS was presented at one of 4 different positions (Up-Right, Up-Left, Down-Right and Down-Left), whose center was 3° away from the fixation point (see Fig. 3.1A). The stimulus consisted of an equal number of black (0.15 cd/m^2) and white (171.85 cd/m^2) dots on a mid-gray background (86.00 cd/m^2). Diameter and density of the dots were 0.16° and 25%, respectively. Dot patterns in each eye were refreshed at 20 Hz. An RDS composed of a central disk (diameter: 3°) and a surrounding ring (width: 0.5°, outer diameter: 4°; see Fig. 3.1A for an example stimulus used in the stereoacuity experiment). While the surrounding ring always had zero disparity, the binocular disparity in the central disk varied across trials (±0.12, ±0.24, ±0.48, ±0.96, ±1.92, ±3.84, ±7.68 arcmin; these disparity magnitudes were chosen based on the range of human stereoacuity (Zaroff et al., 2003). The stimulus duration was 94 ms, in order to avoid the occurrence of vergence eye movements (Masson et al., 1997). The inter-stimulus interval was 2 s.

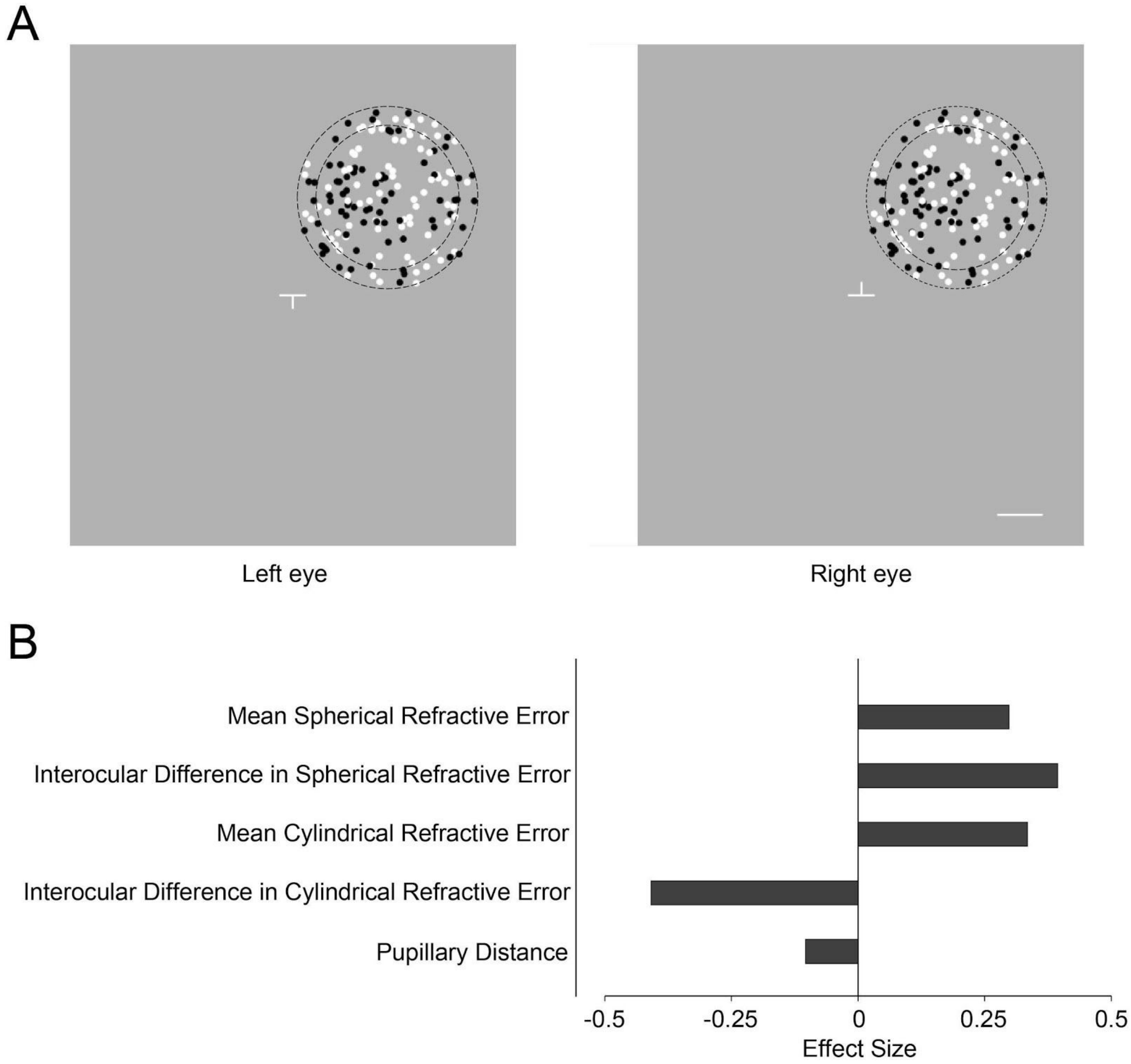

Figure 3.1. Details of stereoacuity experiment. A. Random dot stereogram (RDS) stimulus used to test stereoacuity. Left and right panels show the stimulus in the left and right eyes, respectively. I used a haploscope to present the RDS stimulus. The RDSs consisted of central and surrounding stimuli, which are highlighted as dotted contours (not visible in the experiment). Dots on the central disk had crossed or uncrossed binocular disparities, while dots on the surrounding ring and the fixation target (a cross when properly fused) had zero disparity (See Materials and Methods for more details of stimulus parameters). The white scale bar depicts 1°, which was not visible in the experiment. Participants were asked to judge whether the central disk appeared to be nearer or farther than the surrounding ring. B. Difference in refractive errors and pupillary distance of eyes between good stereoacuity (low disparity-threshold) and poor stereoacuity (high disparity-threshold) groups. The difference in stereoacuity between these two groups was not accompanied by the difference in mean spherical refractive error (d' = 0.30, $t_{17} = 0.65$, p = 0.53, -4.25 ± 2.16 and -4.93 ± 2.41 diopters for good and poor stereoacuity groups), interocular difference in spherical refractive error (d' = 0.39, $t_{17} = 0.86$, p = 0.40, 0.90 ± 0.53 and 0.69 ± 0.51 diopters for good and poor stereoacuity groups), mean cylindrical refractive error (d' = 0.33, $t_{17} = 0.73$, p = 0.48, -0.85 ± SD = 0.74 and -1.07 ± 0.59 diopters for good and poor stereoacuity groups), interocular difference in cylindrical refractive error (d' = -0.41, t_{17} = -0.89, p = 0.39, 0.40 ± 0.38 and 0.64 ± 0.75 diopters for good and poor

stereoacuity groups) and pupillary distance between eyes (d' = -0.10, $t_{17} = -0.23$, $p = 0.82$, 63.3 ± 2.06 and 63.56 ± 2.83 mm for good and poor stereoacuity groups).

Task.

Participants performed a single-interval, two-alternative forced-choice near/far discrimination task. Participants judged whether the central stimulus appeared nearer or farther than the surrounding ring while fixating on the central fixation point (Fig. 3.1A). The stimulus position (Up-Right, Up-Left, Down-Right and Down-Left) was constant within a session of 42 trials (three trials for each disparity condition), and was randomized across sessions. Participants went through 20 sessions in total (5 sessions for each stimulus position). Before the main experiment, the participants practiced the task with longer stimulus presentation (500 ms) and 8 different binocular disparities (±0.24, ±0.96, ±3.84, ±15.36 arcmin). Every participant practiced an identical number of trials (24 trials in total, 3 trials for each disparity condition).

Analysis.

I estimated stereoacuity in each participant by fitting their correct response rate with a cumulative Gaussian psychometric function using a maximum-likelihood estimation (Wichmann and Hill, 2001). The responses were pooled across all four positions and across crossed and uncrossed disparities because there was no systematic difference in performance across positions and depth directions. Hereafter, I defined stereoacuity as the magnitude of binocular disparity corresponding to the 84% correct rate in the task. I identified stereoacuity from 14 participants by using this procedure, however, I could not identify stereoacuity in the other 5 participants whose correct rate was below 84% in all disparity conditions I tested (Fig. 3.2). Note that the five participants were not stereoblind because in the practice session before the main experiment, they could discriminate depth with a longer duration (500 ms) and a larger disparity (15.36 arcmin) with an accuracy (100, 70.8, 83.3, 87.5, 95.8% for 15.36 arcmin) significantly higher than the chance level (95% confidence interval = 42.7 - 63.3% using binomial distribution).

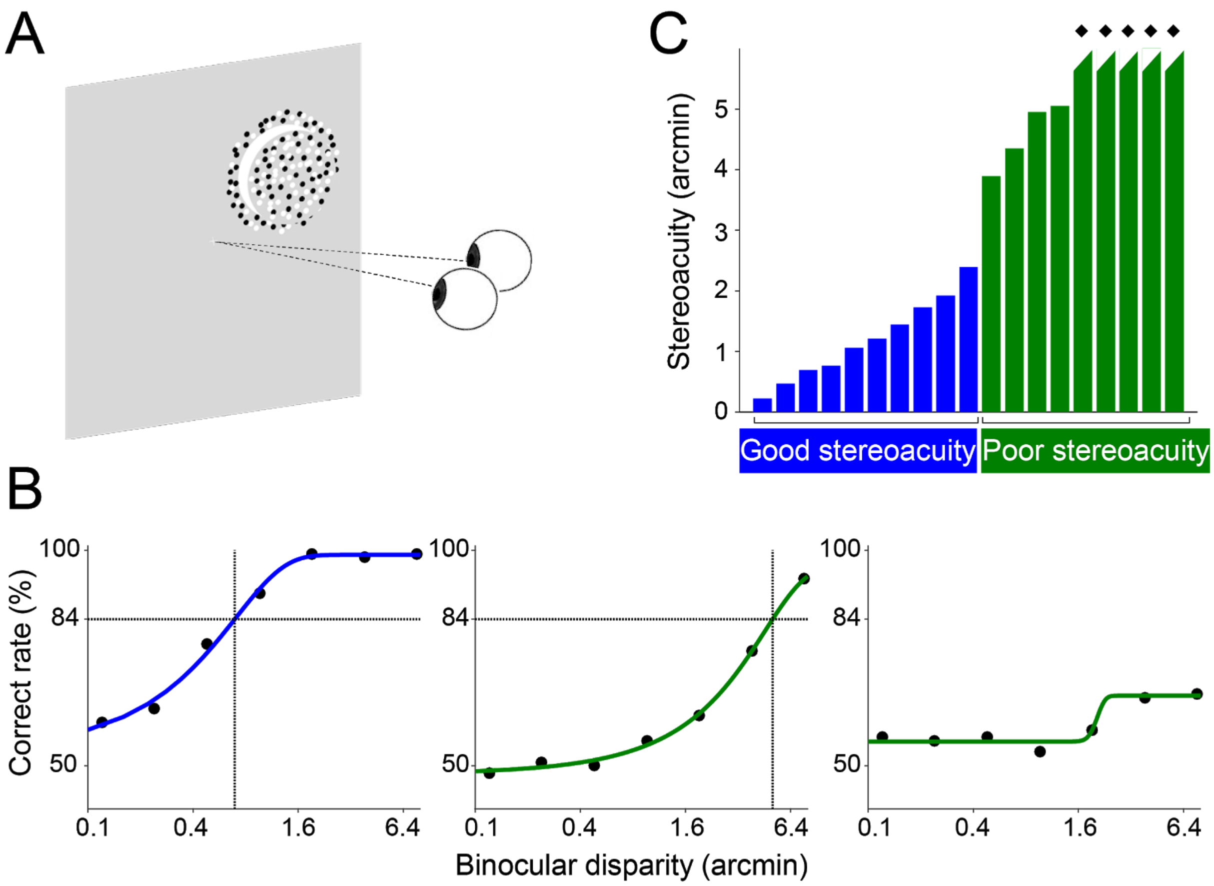

Figure 3.2. Psychophysical experiment on stereoacuity. A. Schematic illustration of depth discrimination task using RDSs. An RDS was concentric-bipartite. Participants were asked to judge whether the central disk was nearer or farther than the surrounding disk. B. Psychometric functions in three representative participants with different performances. Horizontal axis depicts binocular disparity (arcmin; logarithmic scale), while the vertical axis depicts the correct rate. The performance on crossed and uncrossed disparities was averaged. By fitting psychometric function, I estimated stereoacuity as the binocular disparity at which a participant achieved 84% correct rate. For the participant shown in the right panel, the performance was lower than 84% over the tested range of disparities and I could not estimate the stereoacuity using the identical criteria. C. The stereoacuity in all participants (*N* = 19). The vertical axis of bar plot indicates the disparity threshold at which performance reached 84% correct. In the five participants whose stereoacuity could not be estimated (labeled with diamonds), the value of stereoacuity is arbitrary. Note that these five participants were not stereoblind (see Materials and Methods for stereoacuity experiment). I divided participants into good and poor stereoacuity groups using a two-step clustering algorithm and Schwarz's Bayesian criterion.

I used a two-step clustering algorithm applying Schwarz's Bayesian criterion (SPSS Statistics 25, IBM, USA) (Fraley and Raftery, 1998) to identify two subgroups in 14 participants; one with good stereoacuity (*N* = 10; 1.19 ± 0.69 arcmin) and the other with poor stereoacuity (*N* = 4; 4.56 ± 0.55 arcmin). In group comparison analysis (as shown in Fig.

3.3C), the five participants without quantitative stereoacuity estimate were classified into the poor stereoacuity group (N = 9 in total; Fig. 3.2C).

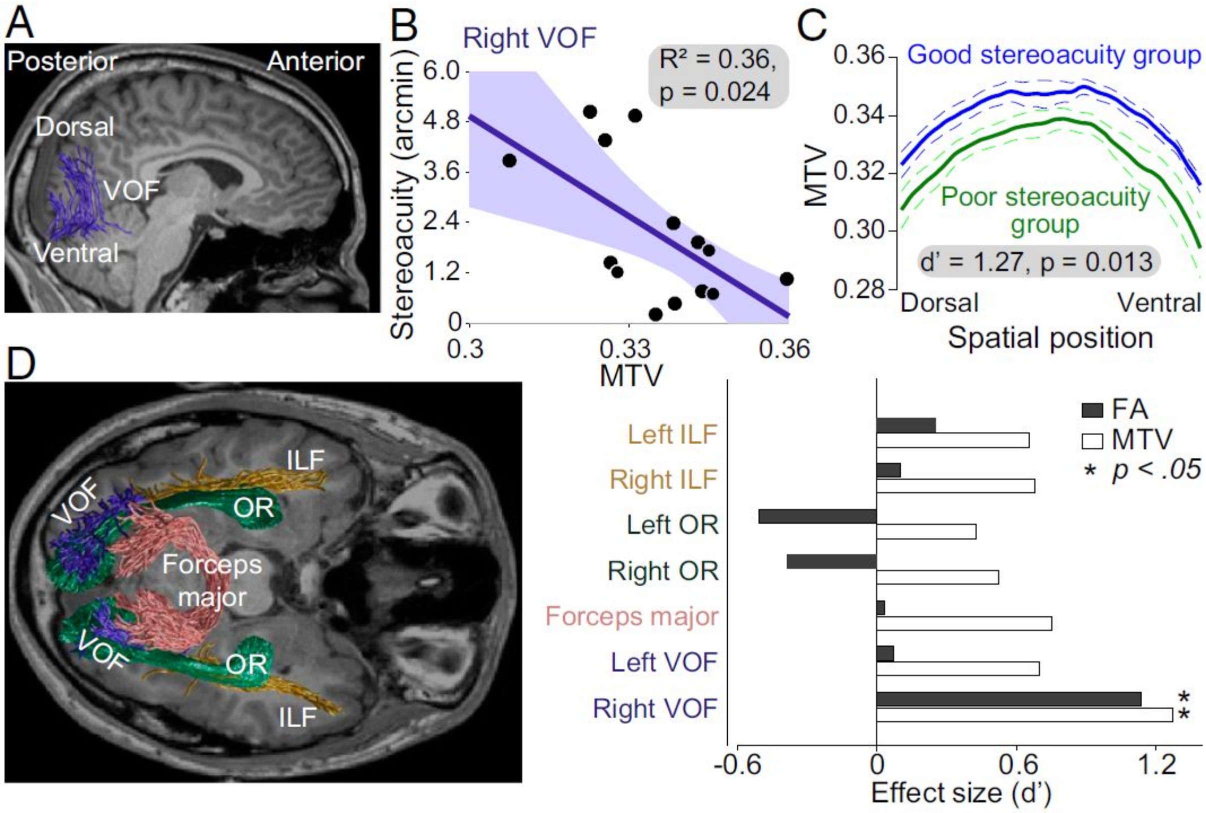

Figure 3.3. Tissue property of the right VOF explains individual differences in human stereoacuity. A.VOF in the right hemisphere identified in a representative participant (participant 9). VOF connects the dorsal and ventral parts of the occipital cortex. B. Correlation between MTV of right VOF and stereoacuity (N = 14; R^2 = 0.36, p =0.024). See Fig. 3.6A for the correlation between FA of the right VOF and stereoacuity. C. Tissue properties along the right VOF in good and poor stereoacuity groups. Vertical axis indicates the MTV along the right VOF, and the horizontal axis indicates the spatial position along the right VOF. Good stereoacuity group (blue, N = 10) showed significantly higher MTV than poor stereoacuity group (green, N = 9) along the entire portion of the right VOF (d' = 1.27, p = 0.013 using two-sample t-test). The solid line indicates the mean in each group, whereas the dotted line indicates ±1 s.e.m. D. No significant statistical support for stereoacuity-dependent difference in FA/MTV of other visual white matter tracts. The left panel depicts the visual white matter tracts estimated by tractography (green, OR; pink, Forceps major; dark yellow, ILF; blue, VOF) in a representative participant (participant 9). In the right panel, the horizontal axis represents the effect sizes (d') of the FA and MTV difference in each visual white matter tract between the good and poor stereoacuity groups. The positive or negative values represent the index values larger or smaller for the good stereoacuity group than for the poor stereoacuity group, respectively. The asterisks in the panel indicate a significant difference between the good and poor stereoacuity groups (p = 0.05, using two-sample t-test). The effect size was largest in the right VOF in a consistent manner across the two independent measurements (FA and MTV).

3.2.3 Psychophysical measurement and analysis of Contrast threshold experiment

Participants.

19 participants underwent a contrast threshold experiment (15 males and 4 females; mean age 26.0 years old), 15 of whom participated in the stereoacuity experiment. For each participant, all procedures in this experiment took around 57 minutes.

Apparatus.

I used a gamma-corrected (Ban and Yamamoto, 2013) (https://github.com/hiroshiban/Mcalibrator2), full-flat 10-bit LCD monitor (sx2262w, Eizo, Japan; spatial resolution, 1920 x 1200 pixels corresponding with 43.4° × 27.4°; frame rate, 60 Hz) to present Gabor patch stimuli. The viewing distance was 60 cm.

Stimuli.

I presented Gabor patch stimuli whose orientation was leftward or rightward tilted by 45° from the vertical (Figure 8B; spatial frequency, 3 cycles/degree; stimulus diameter, 4°; the standard deviation of Gabor filter, 0.8°). The mean luminance of the Gabor patch stimuli and the background were 112.37 cd/m^2. The stimulus positions were identical to those used in the stereoacuity experiment. The stimulus duration was 100 ms.

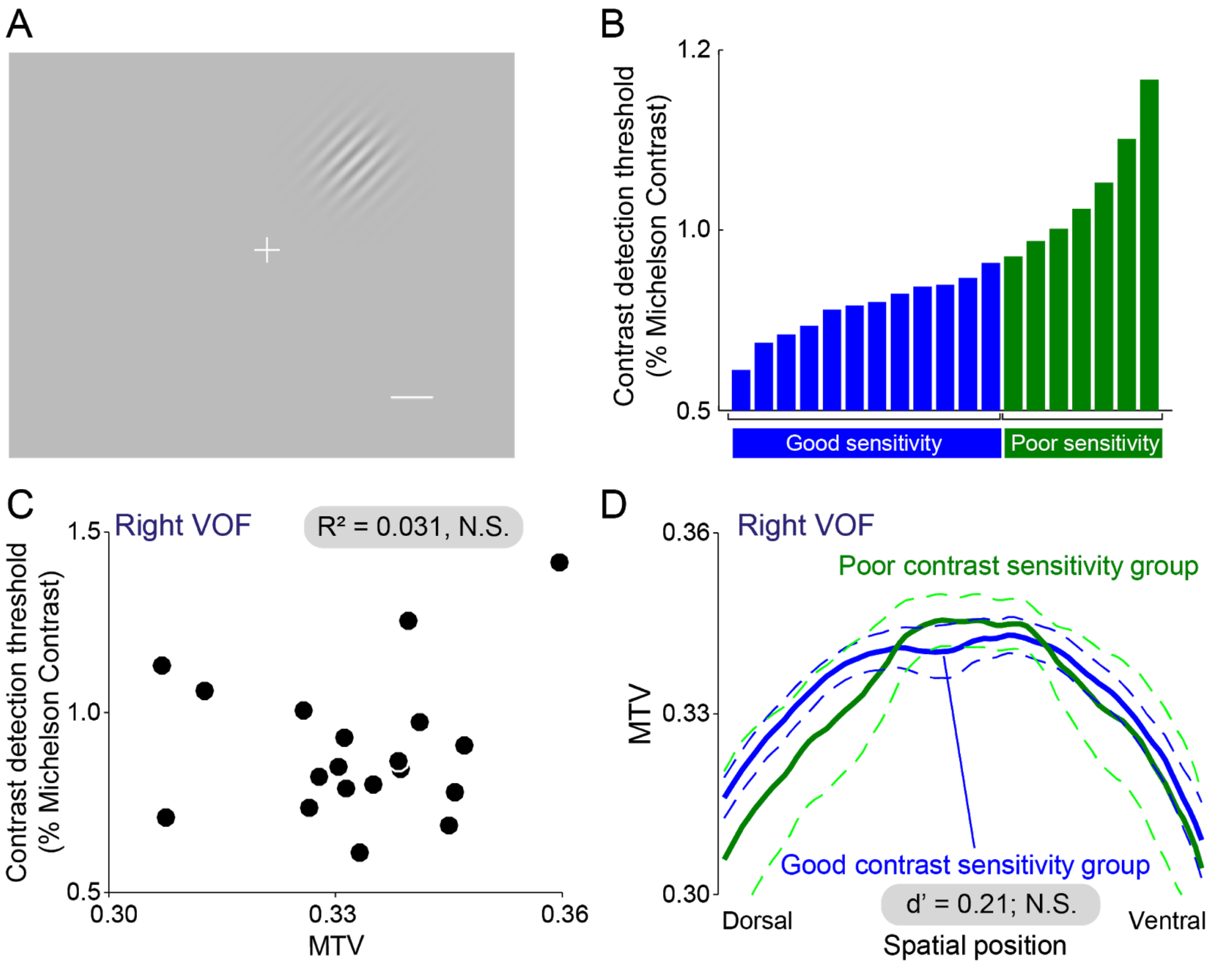

Figure 3.4. Tissue property of the right VOF does not explain individual differences in contrast sensitivity. A. Gabor patch stimulus used for measuring contrast sensitivity (see Materials and Methods). The white scale bar depicts 1°, which was not visible in the experiment. B. Contrast sensitivity of all participants (N = 19). I divided participants into good and poor contrast sensitivity groups using a two-step clustering algorithm and Schwarz's Bayesian criterion. C. Scatter plot of MTV along the right VOF (horizontal axis) and contrast detection threshold in each subject. MTV along the right VOF did not significantly predict contrast detection threshold (R^2 = 0.031, *p* = 0.47). D. The MTV along right VOF in the good and poor contrast sensitivity groups. I did not find a significant difference in MTV between the groups (d' = 0.21, *p* = 0.66). The conventions are identical to those in Fig. 3.3.

Task and analysis.

The experiment consisted of two stages. An approximate threshold was measured in the first stage, which was used to determine the contrast range used at the second stage for estimating a precise threshold. In both stages, participants were asked to judge whether the stimulus orientation was leftward or rightward tilted. In the first stage, I presented Gabor stimuli of six largely different levels of luminance contrast (0.00%, 0.39%, 0.77%, 1.16%, 1.54%, 1.91% Michelson contrast). One session of 18 trials (3 trials for each contrast condition) was performed for each stimulus position. I then pooled the data across four different positions, and roughly estimated the threshold as the contrast corresponding to 84% correct rate by fitting a psychometric function (Wichmann and Hill, 2001). In the second stage, the stimulus contrast was varied at 12 levels between 0% and 1.73% (12 participants), between 0% and 2.1% (6 participants) or between 0% and 2.47% (6 participants), which were around the approximate threshold identified at the first stage. I estimated the contrast detection threshold (84% correct rate) by fitting a cumulative Gaussian function to the correct response rate obtained at the second stage.

I used two-step clustering algorithm and Schwarz's Bayesian criterion to contrast detection threshold to identify two subgroups (Figure 8B): one with good contrast sensitivity ($N = 12$; 0.78 ± 0.085% Michelson contrast) and the other with poor contrast sensitivity ($N = 7$; 1.11 ± 0.17% Michelson contrast).

3.2.4 MRI data acquisition

Anatomical MRI data acquisition and tissue segmentation

I measured T1-weighted MR-RAGE image (1 mm isotropic; TR = 1900 ms, TE = 2.48 ms) from all 23 participants to estimate white/gray matter border. For each participant, acquisition of anatomical MRI image took around 15 minutes. The segmentation was performed using an automated procedure in Freesurfer software (https://surfer.nmr.mgh.harvard.edu/) (Fischl, 2012). The tissue segmentation was used for a subsequent dMRI and fMRI analysis.

Diffusion MRI data acquisition

I measured dMRI data from all 23 participants. DMRI data was acquired at 3T SIEMENS Trio Tim scanner using a 32-channel head coil at Center for Information and Neural Networks (CiNet), National Institute of Information and Communications Technology, and Osaka University. The dMRI data were acquired using dual-spin echo planar imaging (EPI; TR = 5000 ms, TE = 73 ms, multi-band factor = 2, partial fourier = 5/8, and the voxel size of 2 x 2 x 2 mm^3) implemented in multi-band accelerated EPI pulse sequence provided by Center for Magnetic Resonance Research, Department of Radiology, University of Minnesota (Setsompop et al., 2012); https://www.cmrr.umn.edu/multiband/). The diffusion weighting was isotropically distributed along the 64 directions (b-value = 1000 s/mm^2), and a non diffusion-weighted (b = 0) images were acquired at the beginning and end of the dMRI session (total of two b = 0 volumes per image set). To minimize EPI distortion, two image sets were acquired with the reversed phase-encoding directions (A-P and P-A). For each participant, the entire dMRI acquisition took around 20 minutes.

Quantitative MRI data acquisition

I measured qMRI data from all 23 participants. QMRI data was acquired at 3T SIEMENS Trio Tim scanner using 32-channel head coil at Center for Information and Neural Networks (CiNet), National Institute of Information and Communications Technology, and Osaka University. QMRI measurements were obtained from the protocols described in previous publications (Mezer et al., 2013; Gomez et al., 2017). I measured four Fast Low Angle Shot (FLASH) images with flip angles of 4°, 10°, 20°, 30° (TR = 12 ms, TE = 2.41 ms) and a scan resolution of 1 mm isotropic. For the purposes of removing field inhomogeneities, I collected five additional spin echo inversion recovery (SEIR) scans with an echo planar imaging (EPI) readout (TR = 3 s, TE = 49 ms, 2x acceleration). The inversion times were 50, 200, 400, 1200, and 2400 ms. In-plane resolution and a slice thickness of the additional scan was 2 x 2 mm^2 and 4 mm, respectively. For each participant, the entire qMRI acquisition took around 35 min.

Functional MRI data acquisition

I further measured a functional MRI (fMRI) dataset to identify cortical areas selectively activated by visual stimuli with binocular disparity.

Participants.

Eight participants, all of whom participated in the psychophysical experiments on stereoacuity, underwent fMRI experiment (7 males, 1 female; mean age 26.6 years old). I excluded two participants who showed low performances on the fixation task from the subsequent analyses (see Experimental design and task). For each participant, all procedures of fMRI experiment took around 60 min.

fMRI Acquisition protocol.

FMRI data were acquired at a 3T Siemens Trio scanner with a posterior half of 32-channel coil. Functional data were collected with parallel acceleration technique (iPAT; acceleration factor = 2) and a simultaneous multi-slice EPI sequence (multi-band factor = 2) to acquire whole-brain (60 slices) volumes at TR = 2 s, TE = 30 ms; flip angle = 70 deg; FOV = 192 mm^2; acquisition matrix = 96 ×96; slice thickness = 2 mm with no gap, implemented in multi-band accelerated EPI pulse sequence provided by Center for Magnetic Resonance Research, Department of Radiology, University of Minnesota (Moeller et al., 2010); https://www.cmrr.umn.edu/multiband/). Data were acquired at a resolution of 2.0 mm isotropic voxels with interleaved T2＊-weighted gradient echo sequence. The slices were aligned parallel to the AC-PC (anterior commissure-posterior commissure) line.

Apparatus.

Stimulus presentation inside the scanner used a stereoscopic projector system, in which the left and right images were generated by a dual head graphic converter (Matrox DualHead2Go, Matrox) and were projected via polarizing filters on a screen placed in front of the participants. The participants viewed through eye glasses with a pair of polarizing filters that match with those on the projector. Stimuli were presented with a spatial resolution of 1024 × 820 pixels at a frame rate of 85 Hz on a full-flat screen (333 mm × 266 mm). The viewing distance was 97 cm, and the visual angle of the screen was 19.5° × 15.6°.

Experimental design and task.

The participants viewed 12-s blocks of gray background ("Blank"), RDS, or uncorrelated RDS (uRDS), during which the participants performed a fixation task requiring vernier detection (see below). In "Blank" blocks, only a fixation point was presented. In "RDS" blocks, the RDSs identical to those used in the stereoacuity measurement were presented. Binocular disparity of central stimulus was randomly chosen from ±1.92, ±3.84 and ±7.68 arcmin. In "uRDS" blocks, the random dot stimuli presented in the left and right eyes were mutually independent so that participants did not perceive depth. In "RDS" or "uRDS" blocks, the stimulus was simultaneously presented in all four positions used in the psychophysical experiment, and the stimuli for 0.5 s was repeated 12 times with an inter-stimulus-interval of 0.5 s. Each session started from a "Blank" block, followed by 6 repetitions of 3 types of blocks ("RDS" - "Blank" - "uRDS" - "Blank"). Ten sessions were repeated for each participant. During the fMRI experiment, the participants were asked to perform a demanding vernier detection task (Preston et al., 2008) on the fixation point. This ensured proper fusion of the left and right images as well as similar levels of attentional engagement across different stimuli (correlated, uncorrelated, and blank) (Preston et al., 2008). The correct rates of two participants were lower than or close to the chance level (95% binomial proportion confidence interval) when stimuli were presented on the right side. As this result means they were not able to fuse left and right eye image during the experiment, I excluded the two participants from the analysis.

3.2.5 MRI data analysis

<u>*Diffusion MRI data analysis*</u>

Preprocessing.

DMRI images were corrected for susceptibility-induced distortions using FSL TOPUP tools (Andersson et al., 2003). Eddy current distortions and participant motion in the dMRI images were removed by a 14-parameter constrained non-linear co-registration based on the expected pattern of eddy-current distortions given the phase-encode direction of the acquired data (Rohde et al., 2004) using mrDiffusion tools implemented in vistasoft distribution (https://github.com/vistalab/vistasoft).

Tracking.

I used constrained spherical deconvolution (CSD; $L_{max} = 8$; (Tournier et al., 2007) to estimate fiber orientation distribution in each voxel using MRTrix3 (Tournier et al., 2012); http://www.mrtrix.org/). I performed probabilistic tractography implemented in MRTrix to generate 2 million candidate streamlines for each dMRI dataset (step size = 0.2 mm; maximum angle between successive steps = 9 deg; minimum length = 10 mm; maximum length = 250 mm; FOD amplitude stopping criterion = 0.1). The seed voxels for tracking were randomly chosen from the gray-white matter interface region (Smith et al., 2012).

Tractography optimization.

I optimized the estimate of tractography using Linear Fascicle Evaluation (LiFE; (Pestilli et al., 2014; Caiafa and Pestilli, 2017); https://francopestilli.github.io/life/). Briefly, using LiFE, I eliminated streamlines which made no contribution to predict the diffusion signal. Further technical details of LiFE are described in previous publications (Pestilli et al., 2014; Takemura et al., 2016a, 2016b; Uesaki et al., 2017).

<u>*Tract identification from diffusion MRI data*</u>

Except for the optic radiation (see below), I identified major visual white matter tracts from streamlines generated by probabilistic tractography in MrTrix and selected by LiFE.

VOF.

I identified the VOF using open-source MATLAB code distributed with Automated Fiber Quantification (AFQ) toolbox (Yeatman et al., 2012b); https://github.com/yeatmanlab/AFQ). I identified streamlines which traveled in vertical direction and were located posterior to the arcuate fasciculus, and whose ventral endpoints were near the ventral and lateral occipito-temporal cortices defined in Freesurfer atlas (Desikan et al., 2006). The details of the VOF identification method were described in previous papers (Yeatman et al., 2014b; Duan et al., 2015; Takemura et al., 2017).

Forceps major.

I identified the forceps major as streamlines which passed through three ROIs. One ROI was the mid-sagittal plane of the corpus callosum (Huang et al., 2005) which was automatically segmented using AFQ. The other two ROIs in left or right hemispheres were manually defined on the coronal plane located in Y=-65 (ACPC coordinate) because the transformation of these ROIs from MNI152 template did not work properly in some participants, presumably because the morphological differences between the Japanese brains and the MNI152 template.

ILF.

I identified the ILF using automated pipelines implemented in AFQ toolbox (https://github.com/yeatmanlab/AFQ) (Yeatman et al., 2012b). Briefly, AFQ transforms two coronal ROIs (anterior and posterior) in MNI152 template into individual brains, and then selects streamlines passing through both of coronal ROIs (Yeatman et al., 2012b).

Optic radiation.

I identified the optic radiation (OR) using a dedicated method (ConTrack; Sherbondy et al., 2008a), because there are known challenges to estimate human OR using a standard whole-brain tractography, particularly on the tracking of crossing fiber regions around Meyer’s loop (Chamberland et al., 2017). First, I estimated the approximate location of the lateral geniculate nucleus (LGN) on manual inspection of T1-weighted image and deterministic tractography from the optic chiasm (Ogawa et al., 2014). I then placed a 8-mm radius sphere that covered the LGN endpoints of streamlines from the optic chiasm. Second, I identified the location of the primary visual cortex (V1) using a probabilistic atlas of retinotopic visual areas (Wang et al., 2015). Using ConTrack, I then sampled 100,000 candidate streamlines connecting LGN and V1 (angle threshold, 90 deg; step size, 1 mm). Tracking was restricted using the white matter mask generated by tissue segmentation. I selected the top 50,000 streamlines with a higher score in the ConTrack scoring process (Sherbondy et al., 2008b). Further details on the methods to identify the OR using ConTrack are described in previous papers (Sherbondy et al., 2008b; Levin et al., 2010; Ogawa et al., 2014; Duan et al., 2015; Takemura et al., 2017).

Across-session averaging and outlier exclusion.

I identified the tracts (VOF, Forceps Major, ILF and OR) of each participant, separately for two dMRI sessions with reversed phase encoding directions. After merging streamlines of each tract from the two sessions, I excluded outlier streamlines based on a criteria used in previous works (Takemura et al., 2016b, 2017), for subsequent evaluation of tissue properties.

3.2.6 Quantitative MRI data analysis

Both the FLASH and the SEIR scans were processed using the mrQ software package (https://github.com/mezera/mrQ) in MATLAB to produce the MTV maps. The mrQ analysis pipeline corrects for RF coil bias using SEIR-EPI scans, producing accurate proton density (PD) and T1 fits across the brain. Using individual participants' voxels containing cerebrospinal fluid (CSF) within the ventricles, maps of macromolecular tissue volume (MTV) were produced by calculating the fraction of a voxel that is non-water (CSF voxels were taken to be nearly 100% water). The full analysis pipeline and its published description can be found at (https://github.com/mezera/mrQ; Mezer et al., 2013).

3.2.7 Functional MRI data analysis

Functional MRI data were analyzed using MrVista in vistasoft distribution (https://github.com/vistalab/vistasoft). I first corrected slice timing in accord with the multi-slice acquisition order and corrected motions both within and between scans. I fitted a general linear model (GLM) consisting of predictors convolved with hemodynamic response function (two-gamma HRF; (Friston et al., 1998) to the time course of each voxel). I then compared beta-weights of predictors between ”RDS” and “uRDS” blocks, and generated statistical maps of contrasts ($p < 0.05$ using a one-sample *t*-test). I used a probabilistic atlas proposed in a previous study (Wang et al., 2015) to estimate cortical location of visual field maps.

3.2.8 Evaluating tissue properties of tract

I evaluated the tissue properties of each visual white matter tract based on the methods used in previous studies (Levin et al., 2010; Yeatman et al., 2012a; Ogawa et al., 2014; Duan et al., 2015). Briefly, I resampled each streamline to 100 equidistant nodes. Tissue properties were calculated at each node of each streamline using spline interpolation of the tissue properties: fractional anisotropy (FA) and macromolecular tissue volume (MTV). MTV map was registered with dMRI data in each participant and I computed the MTV values along each node of each streamline. Properties at each node were summarized by taking a weighted average of the FA or MTV on each streamline within that node. The weight of each streamline was based on the streamline’s Mahalanobis distance from the tract core. I excluded the first and the last 10 nodes from the tissue property of tract core in order to exclude voxels close to gray/white matter interface where the tract is likely to be heavily intersected with superficial U-fiber system (Ogawa et al., 2014; Duan et al., 2015). I summarized the profile of each tract with a vector of 80 values representing the FA or MTV values sampled at equidistant locations along the central portion of the tract. FA was averaged across two sessions.

I first examined which white matter tracts explain individual differences in stereoacuity by evaluating multiple linear regression models predicting stereoacuity from tract properties. In this analysis, I used the data of 14 participants whose stereoacuity can be estimated. For each participant, MTV or FA values along 80 equidistant nodes in each tract are averaged to obtain a subject-specific single number summary representing tract tissue property. I then generated multiple linear regression models which predict individual differences of stereoacuity by using tract properties as explanatory variables. In each model, explanatory variables are chosen from tract property (either MTV or FA) of seven white matter tracts. I identified (left and right OR, left and right ILF, left and right VOF and forceps major). The explanatory variables were the property of either one tract or combinations of multiple tracts. In total, I tested 127 possible linear regression models for each MTV and FA to predict the stereoacuity. In order to select the best model, I used the Bayesian Information Criterion (BIC), which enables a model comparison by penalizing models with more parameters as a redundant model. I define a model with the smallest BIC as the best models for MTV and FA, separately. I also evaluated a statistical significance of goodness-of-fit for each model by using F-test (Table 1).

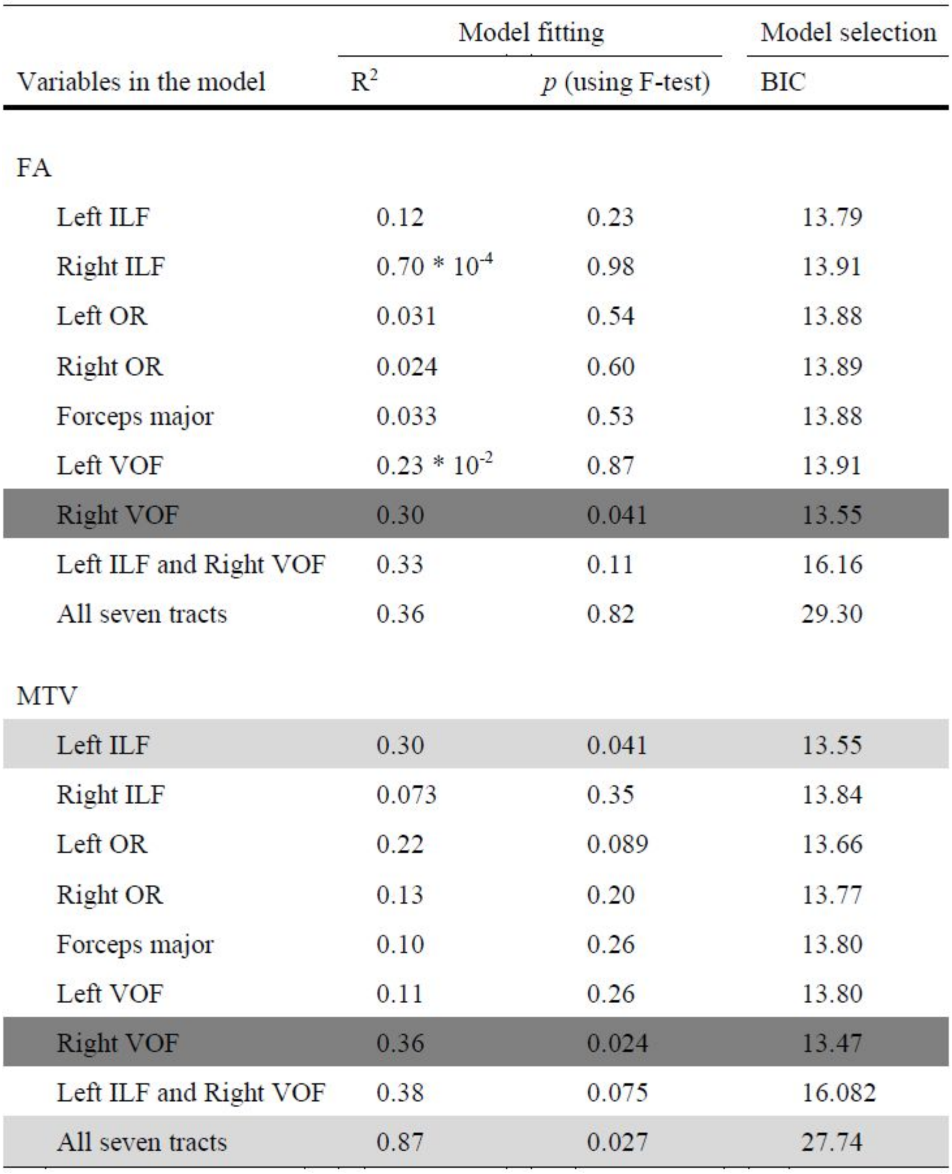

	Model fitting		Model selection
Variables in the model	R^2	*p* (using F-test)	BIC
FA			
Left ILF	0.12	0.23	13.79
Right ILF	$0.70 * 10^{-4}$	0.98	13.91
Left OR	0.031	0.54	13.88
Right OR	0.024	0.60	13.89
Forceps major	0.033	0.53	13.88
Left VOF	$0.23 * 10^{-2}$	0.87	13.91
Right VOF	0.30	0.041	13.55
Left ILF and Right VOF	0.33	0.11	16.16
All seven tracts	0.36	0.82	29.30
MTV			
Left ILF	0.30	0.041	13.55
Right ILF	0.073	0.35	13.84
Left OR	0.22	0.089	13.66
Right OR	0.13	0.20	13.77
Forceps major	0.10	0.26	13.80
Left VOF	0.11	0.26	13.80
Right VOF	0.36	0.024	13.47
Left ILF and Right VOF	0.38	0.075	16.082
All seven tracts	0.87	0.027	27.74

Table 1. The statistical evaluation for linear regression models of stereoacuity using properties of visual tracts. The left column indicates the representative input variables in the models. The middle two columns indicate goodness-of-fit statistics of the regression models (R^2 and p-value of F-test). The right column indicates the Bayesian Information Criterion (BIC) of the regression models (see Material and Methods for Evaluating tissue properties of tract). The dark and light gray rows indicate significant models ($p < 0.05$), and the dark gray rows indicate the best model showing the lowest BIC. The model using only the right VOF showed the lowest BIC in both FA and MTV. While the model using only the left ILF was significant for MTV, the model for FA as well as the group analysis (Fig. 3.3D) did not support the relationship between left ILF and stereoacuity.

I also compared the tract profiles (FA or MTV) between the good and poor performance groups defined in the psychophysical experiments (stereoacuity or contrast sensitivity; see above for grouping participants). For a statistical group comparison, after averaging FA and MTV measurements across all 80 nodes for each participant and tract, I computed the effect size (d’) and statistical significance of inter-group difference using a two-sample t-test. In this analysis, I utilized the data of all 19 participants including 5 participants whose stereoacuity cannot be estimated.

3.2.9 Evaluating the overlap between VOF cortical endpoint and fMRI-based localization

I evaluated overlap between fMRI-based activation maps driven by binocular disparity (see Functional MRI data analysis) and the VOF endpoints. First, I measured the distance between VOF streamline endpoints and gray matter voxels. I defined gray matter voxels within 1.5 mm, 3.0 mm, 4.5 mm, from any of VOF streamline point as voxels covered by the VOF. Second, I calculated the proportion of gray matter voxels near VOF intersecting with fMRI-based activation map for binocular disparity with a specific statistical threshold ($p < 0.05$). I computed the proportion separately for dorsal and ventral VOF endpoints. This overlap analysis was used in several previous publications (Takemura et al., 2016b, 2017; Uesaki et al., 2017).

I note that there is a known limitation in the spatial precision of this analysis originating from the challenges in associating the cortical surface and dMRI-based estimates of tract endpoints (Reveley et al., 2015). This analysis measures only the general proximity between cortical maps and tract endpoints, not a definitive estimate of the fiber projections into cortical gray matter regions.

3.3 Results

3.3.1 Psychophysical experiment on stereoacuity

In a psychophysical experiment, I measured stereoacuity from 19 healthy human participants as a performance to judge perceived depth based on binocular disparity (Fig. 3.2A). Participants viewed a random dot stereogram (RDS; Julesz, 1971) which consisted of a central disk and a surrounding ring (Fig. 3.1A). Whereas the surrounding stimulus was always presented at zero disparity, the central stimulus was presented at a range of disparities across trials. Participants judged the depth of the central disk (“near” or “far”) with respect to the surrounding ring. Stereoacuity was estimated by fitting a psychometric function to each participant's responses (Wichmann and Hill, 2001). Fig. 3.2B shows examples of psychometric functions and estimated stereoacuity discrimination threshold corresponding to 84% correct rate. Stereoacuity thresholds varied by more than an order of magnitude across individuals (Fig. 3.2C), as reported in previous psychophysical studies (Howard and Rogers, 1995; Zaroff et al., 2003; Hess et al., 2015). I succeeded in estimating stereoacuity of 14 participants. In five participants, their correct rate was lower than 84% over the entire range of the tested disparities (±7.68 arcmin), thus not allowing us to determine stereoacuity from their psychometric functions. However, none of the participants were stereoblind because all of them discriminated depth from RDSs with a longer duration (500 ms) and larger disparities (15.36 arcmin) at significantly better than chance level (see Materials and Methods for Stereoacuity experiment).

3.3.2 Microstructural properties of VOF correlated with individual variabilities in stereoacuity

I collected two independent structural MRI datasets, dMRI and qMRI, from these participants. I performed probabilistic tractography and fascicle evaluation on dMRI dataset (Tournier et al., 2012; Pestilli et al., 2014) to identify the trajectory of major visual white matter tracts (left and right optic radiation, left and right inferior longitudinal fasciculus, left and right VOF, and forceps major of the corpus callosum) following the anatomical prescriptions in previous studies (Catani et al., 2002; Wakana et al., 2004; Sherbondy et al., 2008b; Yeatman et al., 2012b, 2014c; Takemura et al., 2017). I evaluated the tissue properties along these visual white matter tracts by utilizing widely used dMRI measure (FA; Basser and Pierpaoli, 1996) and recently proposed qMRI (MTV) measure quantifying the amount of non-proton neural tissue density (Mezer et al., 2013; Berman et al., 2018). Finally, I examined how the variation of FA or MTV in visual white matter tracts correlates with the stereoacuity thresholds in each participant (see Fig. 3.5).

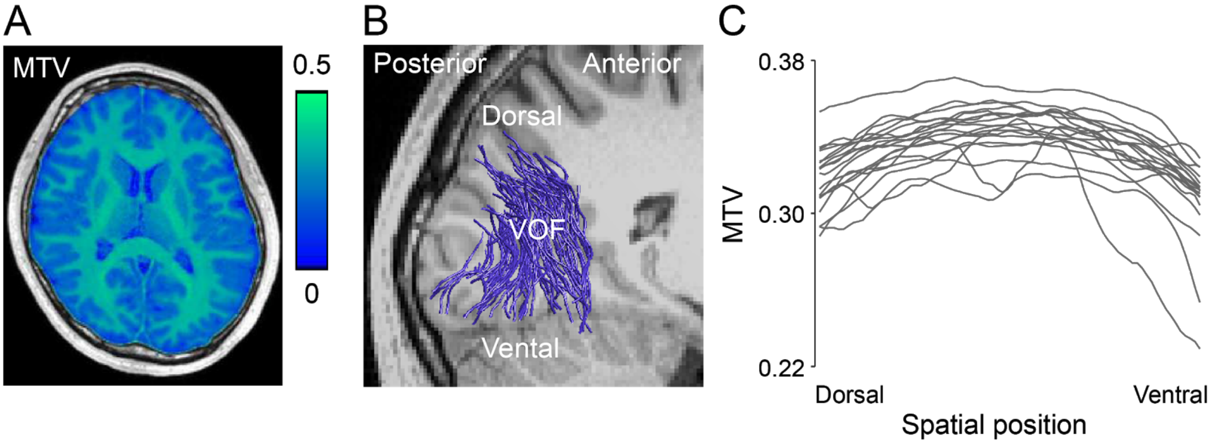

Figure 3.5. Macromolecular tissue volume (MTV; Mezer et al., 2014) along a tract of interest. A. MTV values map in a coronal plane from a representative participant (participant 4). B. VOF identified from dMRI data in the same participant. C. MTV values of all participants (*N* = 19) who participated in the stereoacuity experiment. I divided the VOF in each participant into 100 nodes from dorsal to ventral. I estimated the profile of MTV along the VOF by a coregistration across dMRI dataset and MTV maps in each individual participant, and calculated the MTV values in each node along the VOF. MTV values (vertical axis) from node 11 (dorsal) to 90 (ventral; horizontal axis) were plotted. Each line indicates the MTV profile of individual participants. See Materials and Method for technical details on the estimation of MTV profile along white matter tracts.

First, I examined white matter tracts that explain individual differences in stereoacuity, by comparing a performance of multiple linear regression models which predict stereoacuity from tissue properties (MTV or FA) of examined tracts (see Materials and Methods). This analysis utilized the data of the 14 participants whose stereoacuity was quantitatively estimated (an analysis utilizing all 19 participants data is also presented below). I then selected the best linear regression model by utilizing a Bayesian Information Criterion (BIC). The BIC model selection for the MTV of visual white matter tracts revealed that the regression using a single tract, the right VOF (Fig. 3.3A), is significant and the best model for predicting the stereoacuity (R^2 = 0.36, $F_{(1,12)} = 5.78$, $p = 0.024$ using BIC model selection; Fig. 3.3B, Table 1). The next best model was the one using the left ILF, and also predicted the stereoacuity significantly (R^2 = 0.30, $F_{(1,12)} = 5.22$, $p = 0.041$; Table 1). Models with the other visual tracts or tract combinations did not significantly correlate with the stereoacuity (Table 1). The right VOF is the white matter tract whose microstructural property best predicts the individual variability of stereoacuity.

The BIC model selection for the FA also provided similar results: the best model to explain human stereoacuity used a single tract, the right VOF (R^2 = 0.30, $F_{(1,12)} = 5.22$, $p = 0.041$; see Fig. 3.6 and Table 3.1). None of other models including the model using FA of the left

ILF ($R^2 = 0.12$, $F_{(1,12)} = 1.57$, $p = 0.23$) significantly predicted the stereoacuity (Table 1). The results that the structural-behavioral correlation along the right VOF was replicated across two independent measurements using different pulse sequences (dMRI and qMRI) suggest that the observed correlation will be related to neural tissue volume along the right VOF, rather than the morphological factors specifically affecting FA (e.g., crossing fibers).

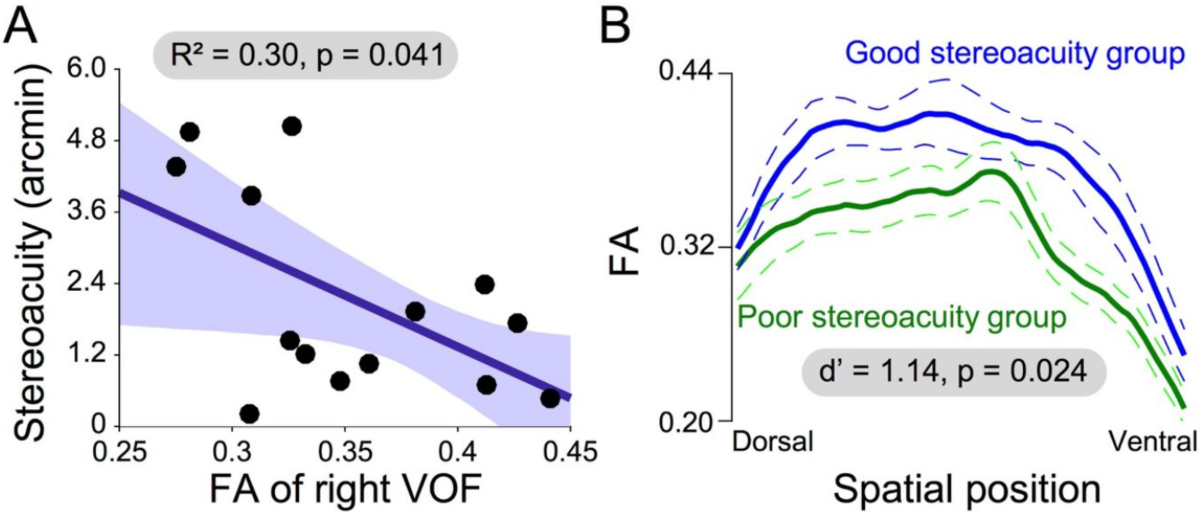

Figure 3.6. Fractional Anisotropy (FA) of the right VOF and individual difference in stereoacuity. A. Correlation between FA of the right VOF and stereoacuity ($N = 14$; $R^2 = 0.30$, $p = 0.041$). B. FA along the right VOF in good stereoacuity (blue, N = 10) and poor stereoacuity group (green, N = 9). Conventions are identical to those in Fig. 3.3.

I further examined how the MTV and FA differ across participants with good stereoacuity (low disparity-threshold) or poor stereoacuity (high disparity-threshold), by incorporating datasets from all participants ($N = 19$) including five poor stereoacuity participants whose stereoacuity cannot be estimated from psychometric function (Fig. 3.2B). To this end, I took a group comparison approach by classifying participants into good ($N = 10$) and poor stereoacuity groups ($N = 9$), which included the five participants without parametric estimates of stereoacuity (Fig. 3.2C; see Materials and Methods for methods to classify participants into good or poor stereoacuity groups). I found that the good stereoacuity group ($N = 10$) showed a significantly higher MTV (Fig. 3.2C; d' = 1.27, $t_{17} = 2.77$, $p = 0.013$) and higher FA (Fig. 3.6B; d' = 1.14; $t_{17} = 2.48$; $p = 0.024$) along the right VOF, further supporting the relationship between microstructural properties of the right VOF and stereoacuity. The spatial profile of tract property suggests that the group difference was present along the entire length of the right VOF from dorsal to ventral (Figs. 3.4C and 3.5B), not at a restricted local region. Thus, it is unlikely that the group difference can be explained by a partial volume effect with other short-range fibers (such as U-fiber). I did not find any significant differences of MTV and FA between the two groups in the other visual white matter tracts (left VOF, the forceps major, the OR and the ILF in both hemispheres; Fig. 3.3D). It should be noted that the difference in stereoacuity between these two groups was not accompanied by differences in refractive power or the pupillary distance of the eyes (Fig. 3.1B) nor by age (t_{17} = 0, p = 1, 25 ± 5.19 and 25 ± 3.31 years old for good and poor stereoacuity groups, respectively).

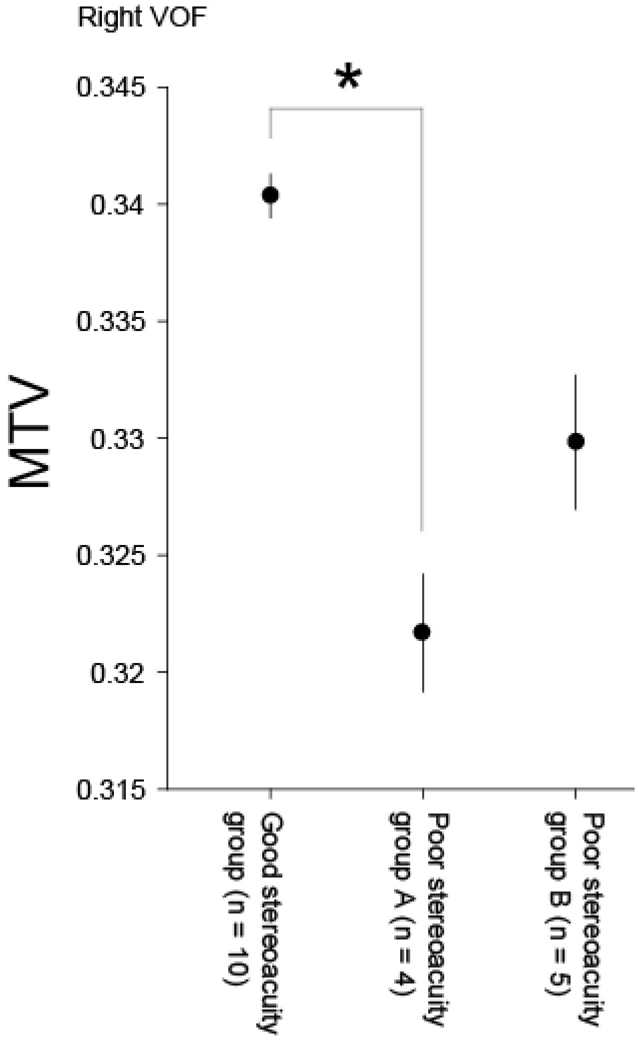

Figure 3.7. MTV differences of right VOF between the good stereoacuity group and the sub-populations of the poor stereoacuity group. I subdivided the poor stereoacuity group into the poor stereoacuity group 1 or 2. The poor stereoacuity group 1 indicates the participants (n = 4) whose stereoacuity I could estimate. The poor stereoacuity group 2 indicates the participants (n = 5) whose stereoacuity I could not quantitatively estimate (Fig. 3.2C). The dots indicate the mean of the MTV of each group. The error bars indicate ±1 S.E.M. MTV was significantly different between good stereoacuity group and poor stereoacuity group 1 (t_{12} = 3.26, p = 0.0068).

While I included the five poor stereoacuity participants whose stereoacuity cannot be estimated among the poor stereoacuity group, one might argue that these participants are distinct from those whose stereoacuity were quantitatively estimated. I thus defined two poor stereoacuity groups, one is whose stereoacuity I could estimate (poor stereoacuity group 1, n = 4) and the other one is not (poor stereoacuity group 2, n = 5). I tested the difference of the MTV among the groups (Fig. 3.7). I found the MTV was significantly different between the good stereoacuity group and poor stereoacuity group 1 ($t_{12} = 3.26$, $p = 0.0068$). This result is consistent with the group comparison between high and poor stereoacuity groups (Fig. 3.3C). However, while the MTV of good stereoacuity group was higher than those of poor stereoacuity group 2, the differences were not significant ($t_{13} = 1.70$, $p = 0.11$). The MTV of poor stereoacuity group 2 was 0.3070, 0.3257, 0.3331, 0.3397, 0.3435. Since the mean of the mtv of the high stereoacuity group was 0.340, one of the five participants in poor stereoacuity group 2 thus showed higher MTV than the mean of the good stereoacuity group. One possibility is the participant's disparity detection performance was not poor. While all the participants could pass the practice session for stereopsis, the differences between stereoacuity experiment and practice session were the disparity magnitude and the stimulus duration (see *analysis* in the section of 3.2.2 Psychophysical measurement and analysis of stereoacuity experiment). This means the poor stereoacuity group 2 includes participants with poor performance for either or both fine disparity and rapid stimulus presentation. The participant in poor stereoacuity group 2 with higher MTV might have been not poor for stereoacuity but poor for the perception of rapid stimulus presentation. However, I can not exclude other possibilities for the not significant difference, including the case that the participants in the poor stereoacuity group 2 were less motivated for the stereoacuity experiment or a lack of the statistical power for the group comparison due to the small population in the poor stereoacuity group 2 (Makin and de Xivry, 2019).

3.3.3 Cortical regions responding to visual stimuli with binocular disparity

In order to test whether the right VOF indeed connects cortical areas involved in binocular disparity processing, I performed fMRI experiments to measure cortical responses activated by the same RDSs as those in the psychophysical experiment (see Materials and Methods for functional MRI data acquisition). I observed significant BOLD responses to the RDSs compared to the uncorrelated RDSs in both dorsal and ventral extrastriate cortices, which are consistent with previous fMRI studies in humans (Fig. 3.8; Tsao et al., 2003; Neri et al., 2004; Preston et al., 2008; Ip et al., 2014). Importantly, both dorsal and ventral VOF endpoints overlapped with disparity-selective regions (Fig. 3.8; see Materials and Methods). The results agree with the idea that discrimination of stereoscopic depth involves an interaction between dorsal and ventral cortices throughout the VOF.

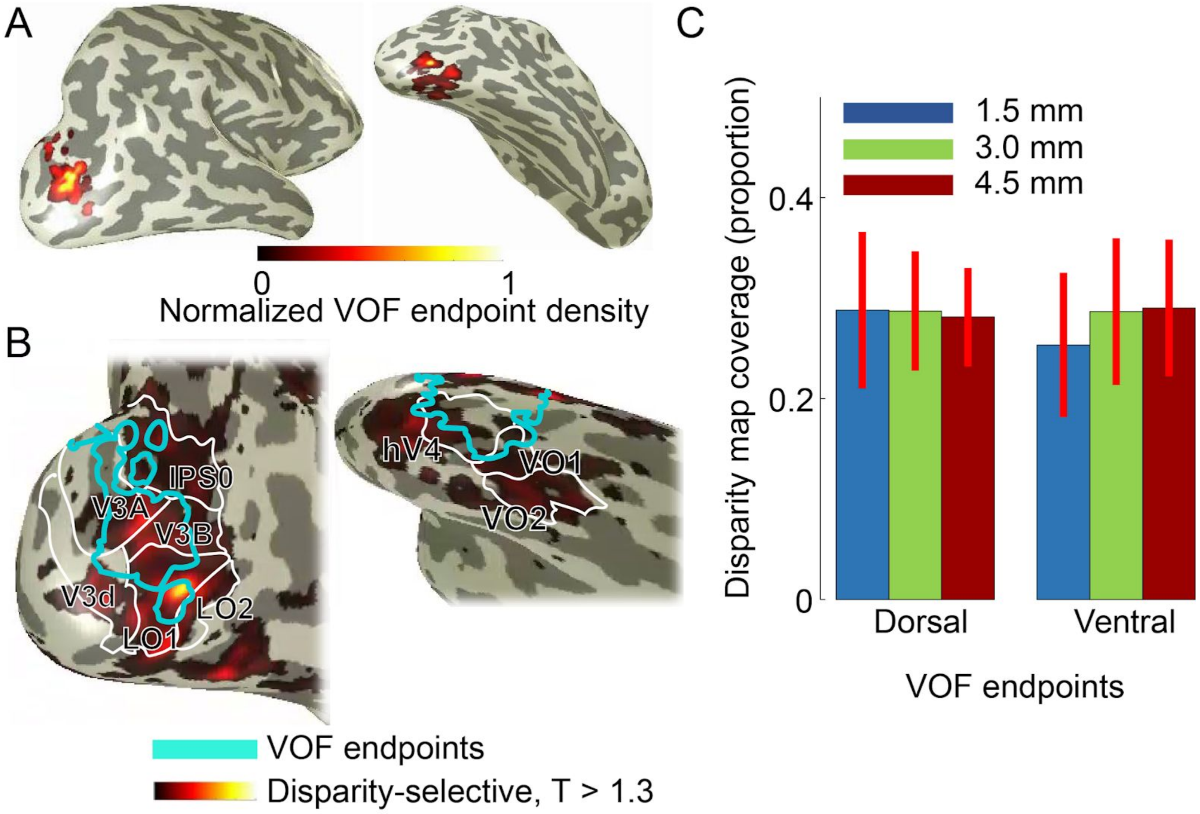

Figure 3.8. Comparison between VOF endpoints and disparity-sensitive regions. A. Cortical coverage of the VOF endpoints in the right hemisphere from a representative participant (Left panel: dorsal view; Right panel: ventral view; both data from participant 8). I estimated the normalized VOF endpoint density on gray matter by counting a number of streamlines which had an endpoint within 3 mm from each gray matter voxel (see Materials and Methods). The left and right panels represent dorsal and ventral VOF endpoints, respectively. B. Disparity selective areas (hot color) which were significantly activated in the "RDS" blocks than in the "uncorrelated RDS" blocks ($p < 0.05$ using a one-sample t-test). The borders of estimated VOF endpoints (cyan, identical in A) as well as the borders of visual areas (white) were overlaid. Cortical coverage of the VOF endpoint and its relation to the retinotopic areas is consistent with a previous study which measured retinotopy using fMRI (Takemura et al., 2016b). C. Overlap between VOF endpoints and disparity selective regions in the right hemisphere. Vertical axis indicates the proportion of the gray matter voxels near VOF endpoints which intersected with binocular disparity activation areas. Left and right three bars represent dorsal and ventral VOF endpoints, respectively. Bars with different colors show the data with varying distance thresholds for selecting the gray matter voxels near the VOF endpoints (1.5 mm, blue; 3.0 mm green; 4.5 mm orange). The proportions were averaged across participants ($N = 6$). Disparity-selective

regions overlap with a similar proportion of VOF endpoints across dorsal and ventral visual cortex. Error bars depict ± 1 s.e.m. across 6 participants.

3.3.4 Psychophysical experiment on contrast detection sensitivity

Finally, I addressed whether the tissue properties of the right VOF is specifically related to stereoacuity or to general sensitivity of the visual system. I measured a contrast detection threshold using Gabor patch stimuli, which does not require binocular integration (Fig. 3.4A; Materials and Methods). The contrast detection thresholds varied across the individuals (Fig. 3.4B), but were not significantly correlated with stereoacuity ($r = 0.08$, $p = 0.82$). A simple linear model on the tissue properties along right VOF did not significantly predict contrast detection threshold ($R^2 = 0.017$, $p = 0.59$ for FA; $R^2 = 0.031$, $p = 0.47$ for MTV, Fig. 3.4C). Group difference analysis also suggests no significant difference in the tissue properties between the good contrast sensitivity (low contrast-threshold) and poor contrast sensitivity (high contrast-threshold) groups (Fig. 3.4D; d’ = 0.21, $t_{17} = 0.44$, $p = 0.66$ for MTV; d’ = 0.16, $t_{17} = 0.34$, $p = 0.74$ for FA; see Material and Methods for methods to classify subjects into two groups). Taken together, the FA and MTV difference in the right VOF between the good and poor stereoacuity groups (Fig. 3.3) does not reflect general visual sensitivity assessed by contrast detection threshold.

3.4 Discussion

In the current study, I examined the neurobiological correlates of the large inter-individual differences in stereoacuity. Advanced non-invasive neuroimaging methods, such as dMRI and qMRI, have a strong advantage to investigate neurobiological origin of individual variabilities of sensory abilities, because neuroanatomical and behavioral measurements collected from the same human participants can be compared (Dougherty et al., 2007; Genç et al., 2011; Thiebaut de Schotten et al., 2011; Yeatman et al., 2012a; Gomez et al., 2015; Wandell, 2016). I took this advantage and compared individual differences in human stereoacuity with white matter properties. Supporting classical and recent theories emphasizing the importance of white matter tracts to understand sensory and cognitive functions (Catani and Ffytche, 2005; Catani and Thiebaut de Schotten, 2012), I found a significant statistical evidence for relationship between stereoacuity and the microstructural properties in a specific white matter tract connecting dorsal and ventral visual cortex (right VOF (Yeatman et al., 2013, 2014b; Takemura et al., 2016b). Behavior-anatomy correlations could be found using two independent microstructural measurements (MTV and FA) and analysis strategies (regression and group comparison). I further confirmed that the VOF had endpoints in disparity responsive regions of dorsal and ventral cortices, suggesting that the VOF is a tract connecting cortical regions involved in disparity processing. Finally, the tissue properties of the right VOF were not related to contrast sensitivity.

3.4.1 Microstructural difference of right VOF between good and poor stereoacuity groups

A number of previous studies used conventional diffusion tensor metrics, such as FA, to examine tissue properties of white matter tracts in relation to behavioral characteristics (Dougherty et al., 2007; Genç et al., 2011; Scherf et al., 2014; Yeatman et al., 2014b). In contrast, only a few recent studies use advanced qMRI metrics such as MTV (Mezer et al., 2013; Berman et al., 2018) in order to further understand microstructural properties of white matter tracts. FA is a reproducible metric with high sensitivity to detect tissue structural difference of white matter tracts (Thomason and Thompson, 2011; Wandell and Yeatman, 2013; Rokem et al., 2017; Wandell and Le, 2017; Assaf et al., 2019). However, microstructural interpretation of a difference in FA is generally challenging because FA is known to detect many biological factors, such as axon diameter, axon density, myelin-sheath thickness, and tightness of fasciculation affected by crossing fibers (Basser and Pierpaoli, 1996; Jones et al., 2013; Assaf et al., 2019). Here, I took the approach of combining dMRI with qMRI, which has been proposed to provide additional information for inferring microstructural properties (Mezer et al., 2013; Stuber et al., 2014; Weiskopf et al., 2015). The MTV is a robust qMRI-based metric to quantify the local tissue volume within the voxel by quantification of the proton density (Mezer et al., 2013). There is converging evidence showing that the MTV is a reliable approximation on the lipid and macromolecular volume fractions (Duval et al., 2017; Berman et al., 2018). Taken together, the difference of both FA and MTV profiles in the right VOF between the good and poor stereoacuity groups suggests that the observed difference may reflect a difference in lipid or macromolecule volume fractions, such as myelin thickness or axon density, rather than the morphological configuration of axons such as the degree of fiber crossings.

3.4.2 The possible causal relationships between stereoacuity and VOF

We consider that the structure-behavioral relationship in the VOF may be explained by either or both of two potential factors: strategy of stereo perception alters white matter; white matter plasticity alters stereo perception. Recent neurobiological studies made a major progress in demonstrating that plasticity in white matter microstructure, such as the degree of myelination, is dependent on neural activity or behavioral experience (Sampaio-Baptista et al., 2013; Fields, 2015). We speculate that the behavioral-structural relationship observed in this study might reflect differences in development such as different levels of usage of binocular disparity as a stereo cue, or cue combination strategies across dorsal and ventral visual areas (Dekker et al., 2015). Alternatively, it is also feasible that development of white matter, which has a significant impact on efficient transmission of neural signals, will affect accuracy of stereo perception. However, it is not yet understood how such modulation in conduction velocity is related to the optimality of neural computation for sensory discrimination (Fields, 2015).

3.4.3 A related study of a binocular visual disorder and white matter tracts

Previously, Duan and colleagues (Duan et al., 2015) investigated the microstructural properties of visual white matter tracts between an amblyopia group and a control group. They observed that there is a difference in diffusion property (mean diffusivity) along right VOF, but the difference is not supported by qMRI measurement. Additionally, Duan and colleagues reported a difference in the diffusion property along the optic radiation, which I did not find in this study. The difference between the current result and the result of the previous study (Duan et al., 2015) suggests that the microstructural basis on individual difference in stereoacuity is distinct from the white matter consequence of the amblyopia.

3.4.4 The communication between dorsal and ventral streams via VOF in processing binocular disparity

Despite a visual processing theory emphasizing the role of “dorsal stream” on stereopsis (Hubel and Livingstone, 1987; Sakata et al., 1997; Gonzalez and Perez, 1998) and experimental evidence on neural correlates of stereoscopic depth perception in dorsal areas (Minini et al., 2010), there are converging lines of evidence showing that both dorsal and ventral visual cortices are involved in binocular disparity processing, including computations of relative disparity and disparity-defined three-dimensional shapes (Cowey and Porter, 1979; Ptito et al., 1991; Janssen et al., 1999; Uka et al., 2000; Tanaka et al., 2001; Tsao et al., 2003; Neri et al., 2004; Orban et al., 2006; Preston et al., 2008; Cottereau et al., 2011; Bridge et al., 2013; Chang et al., 2014). Other lines of studies also suggest that the role of dorsal and ventral stream in stereopsis may be complementary because they are sensitive to different types of disparity information (Neri et al., 2004; Uka and DeAngelis, 2006b; Shiozaki et al., 2012b; Chang et al., 2014; Fujita and Doi, 2016). Additionally, cortical representations which account for perceptually relevant disparity processing are found in higher portions of both of the dorsal and ventral visual streams (Bridge and Parker, 2007; Preston et al., 2008) including cortical areas near the VOF endpoints (Takemura et al., 2016b). Here, I found that the stereoacuity measured using the stimuli with relative disparity (Fig. 3.1A) is correlated with the properties of VOF (Fig. 3.3). I also confirmed that the endpoints of VOF overlapped with relative disparity selective regions (Fig. 3.8). Therefore, the VOF may transmit perceptually relevant relative disparity signals, by connecting dorsal and ventral cortices involved in binocular disparity processing.

3.4.5 Relationship between stereoacuity and white matter tracts connecting early visual areas

Diffusion MRI studies have focused on relatively long-range white matter tracts known to exist from anatomical studies (Catani and Thiebaut de Schotten, 2012). However, one might argue that fibers from other areas, such as V2 or MT, may also explain the variability on human stereoacuity. We indeed cannot exclude this possibility. Measuring such relatively short fibers requires a substantial improvement in data resolution, analysis methods as well as anatomical knowledge of the human visual system. Furthermore, the resolution of our dMRI data does not allow us to reliably identify subcomponents of VOF only terminating in/near specific areas. Testing those questions with improved measurements is an important future research direction.

3.4.6 No significant correlation in left VOF to stereoacuity

While the right VOF showed a significant relationship with stereoacuity, I did not find statistically significant results in the left VOF. The asymmetry is consistent with previous studies reporting the lateralization of disparity processing in the right hemisphere. For example, a number of neuropsychological studies reported that the brain damage causing the loss of stereoscopic depth perception is lateralized to the right hemisphere (Carmon and Bechtoldt, 1969; Benton and Hécaen, 1970; Hamsher, 1978; Ross, 1983; Ptito et al., 1991; Gillebert et al., 2015; Bridge, 2016; Murphy et al., 2016), while the generality of these findings has been debated (Howard and Rogers, 1995). FMRI studies also demonstrated some evidence for the lateralization of cortical response to disparity-defined stimuli to the right hemisphere (Nishida et al., 2001; Tsao et al., 2003; Durand et al., 2009; Georgieva et al., 2009; Ip et al., 2014). The current results showing that stereoacuity correlates more strongly with the right VOF are in line with these previous publications.

3.4.7 Limitations of statistical analysis

In this study, I did the exploratory analysis to find the best model of white matter tract for explaining the stereoacuity. This analysis compared the explanatory accuracies among the regressions of the tissue properties of white matter tracts and found that the model using the right VOF data was the best one for explaining stereoacuity. I then tested the linear regression analysis using the right VOF data and showed the significance of the regression. In these analyses, the same right VOF data was used, which could unfairly inflate the statistical power, called circular analysis (Makin and de Xivry, 2019).

To avoid this problem, I should have planned to conduct only the regression analysis of VOF because I had a hypothesis that the VOF was the candidate for explaining the stereoacuity (3.1 Introduction). Another option was analysing without any hypothesis, which tests regressions of all white matter tracts data. However, this analysis requires a large correction of the significant level due to multiple comparisons, and thus could have overlooked the significance, considering the not much number of the participants in this study.

I conclude that the robust demonstration of the correlation between the right VOF and stereoacuity requires a reliable retest study without circular analysis by increasing the number of participants to a statistically desirable number. Based on the statistics of the regression between the MTV of right VOF and stereoacuity (Fig. 3.3B), forty five participants are desirable (using G Power 3; Faul et al., 2007). The retest study with the appropriate detection power will clarify the structural correlation with the stereoacuity in this study was plausible or not.

Chapter 4.

General discussion and conclusion

4.1 Integrative summary

In this dissertation, I first describe the structural and functional properties of geniculo-cortical and cortical visual pathways including the literature of human and NHP. I then describe the key neuroimaging methods for measuring the properties of the human visual pathway.

In the works of this dissertation, I examined structural and functional properties of the geniculo-cortical and cortical pathways in the human visual pathway. The first study (Chapter 2) tested the structural and functional properties in the geniculo-cortical pathway, primarily using MTV and fMRI. I could identify the M and P subdivisions of LGN in living humans, primarily using MTV. I also showed the visual sensitivity difference of the identified M and P subdivisions, which corresponds to the physiological findings of M and P subdivisions in NHP. The second study (Chapter 3) tested the structural coupling with behavior and function in the cortical pathway, using dMRI, MTV, fMRI and psychological experiment. I revealed the relationship between the stereoacuity and structural properties of the VOF. I also showed the VOF connects the dorsal and ventral visual areas that are sensitive to binocular disparity. Taken together, I showed it is possible to non-invasively quantify the structural properties of nucleus and white matter tract in both geniculo-cortical and cortical pathways, and found that the structural property differences were associated with the functional difference in M and P subdivisions and individual differences in stereoacuity. Since our understanding of the human visual pathway has been mainly based on the analogy of the findings in the research on NHP, this dissertation must be a valuable stepping stone to study the relationship between perception, function and structure in the human visual pathway.

4.2 Comparison of the visual pathway between human and NHP

The comparison across species is an important investigation in cognitive neuroscience, which supports the translation of findings between humans and NHP. High resolution fMRI studies showed that the different functional selectivities in human LGN, which corresponds to the M and P functions of NHP (Denison et al., 2014; Zhang et al., 2015). The first study in this dissertation showed different structural densities in LGN, which corresponds to the M and P structural organizations of NHP. These studies suggest that the structural and functional properties of the M and P subdivisions are preserved across humans and NHP.

In the cortical pathway, the VOF in humans connects dorsal and ventral visual areas, including V3A/B and IPS-0 in dorsal and hV4, VO and LO in ventral (Takemura et al., 2016b). The second study in this dissertation suggested that the depth-related signal is communicated between dorsal and ventral visual areas via VOF. However, while NHP has a white matter tract that connects dorsal and ventral areas, the connection surface locations are different between humans and NHP (Takemura et al., 2017; Kaneko et al., 2020). VOF in NHP is more medial than that in humans. It is thus controversial that the VOF in NHP also communicates depth information via VOF. Combining approach of dMRI and fMRI, which is implemented in the second study will clarify the functional similarity of the VOF between humans and NHP in the future.

These findings suggest that the organization of the geniculo-cortical pathway is relatively similar across humans and NHP while the organization of the cortical pathway is relatively different across humans and NHP.

4.3 Potentiality of the noninvasive quantitative structural imagings

In the works of this dissertation, I measured structural properties of thalamic nuclei and white matter tracts using MTV. Besides the MTV, structural imaging methods on living human brains have been recently developed (quantitative T1 (qT1), quantitative magnetization transfer (qMT), quantitative R2* (qR2*), quantitative susceptibility mapping (qSM), see (Tabelow et al., 2019). However, since these quantitative structural image acquisitions including MTV are relatively new techniques, the use of quantitative structural imaging is still minor in the field of cognitive neuroscience. These measurements including MTV will enable us to quantify variable aspects of structural properties such axon, myelin, iron and water concentration, which will be powerful clues to see the structure of the visual areas in a scale of cortical layers and clusters (Fukunaga et al., 2010; Li et al., 2019).

4.4 Applicability of the noninvasive quantitative structural imagings

MTV enables us to identify the correspondence between a structural property of an area and a specific behavior, as the second study revealed the relationship between MTV of VOF and stereoacuity. Brain structure can be changed not only by diseases such as multiple sclerosis (Mezer et al., 2013) in patients, but also plastically changed by development, learning, training and aging in people including healthy people and some experts (Scholz et al., 2009; Yeatman et al., 2014a; Gomez et al., 2017; Huber et al., 2018a). This suggests that we can predict a variety of structures and related behaviors in individuals by monitoring changes of structural properties over time. I expect this idea can be a foundation of the new innovation in the field of healthcare.

4.5 Concluding remarks

Recent MRI techniques have enabled us to quantitatively measure structural tissue properties of the living human visual pathway. In this dissertation, by combining MTV with fMRI, dMRI and psychophysical experiment, I showed the robust identification of visual areas and the correlation of structure and visual perception. These combinatorial approaches will further elucidate the relationship between perception, function and structure in the human visual pathway.

Chapter 5.

References

Adelson EH, Bergen JR (1985) Spatiotemporal energy models for the perception of motion. J Opt Soc Am A 2:284–299.

Amano K, Wandell BA, Dumoulin SO (2009) Visual field maps, population receptive field sizes, and visual field coverage in the human MT+ complex. J Neurophysiol 102:2704–2718.

Amunts K, Lepage C, Borgeat L, Mohlberg H, Dickscheid T, Rousseau M-É, Bludau S, Bazin P-L, Lewis LB, Oros-Peusquens A-M, Shah NJ, Lippert T, Zilles K, Evans AC (2013) BigBrain: an ultrahigh-resolution 3D human brain model. Science 340:1472–1475.

Amunts K, Zilles K (2015) Architectonic Mapping of the Human Brain beyond Brodmann. Neuron 88:1086–1107.

Andersson JLR, Skare S, Ashburner J (2003) How to correct susceptibility distortions in spin-echo echo-planar images: application to diffusion tensor imaging. Neuroimage 20:870–888.

Andrews TJ, Halpern SD, Purves D (1997) Correlated Size Variations in Human Visual Cortex, Lateral Geniculate Nucleus, and Optic Tract. The Journal of Neuroscience 17:2859–2868 Available at: http://dx.doi.org/10.1523/jneurosci.17-08-02859.1997.

Arshad M, Stanley JA, Raz N (2017) Test-retest reliability and concurrent validity of in vivo myelin content indices: Myelin water fraction and calibrated T1 w/T2 w image ratio. Human Brain Mapping 38:1780–1790 Available at: http://dx.doi.org/10.1002/hbm.23481.

Ashburner J, Friston KJ (2000) Voxel-based morphometry--the methods. Neuroimage 11:805–821.

Assaf Y, Johansen-Berg H, Thiebaut de Schotten M (2019) The role of diffusion MRI in neuroscience. NMR Biomed 32:e3762.

Azzopardi P, Jones KE, Cowey A (1999) Uneven mapping of magnocellular and parvocellular projections from the lateral geniculate nucleus to the striate cortex in the macaque monkey. Vision Res 39:2179–2189.

Ban H, Yamamoto H (2013) A non–device-specific approach to display characterization based on linear, nonlinear, and hybrid search algorithms. J Vis 13:20–20.

Barlow HB, Blakemore C, Pettigrew JD (1967) The neural mechanism of binocular depth discrimination. J Physiol 193:327–342.

Barral JK, Gudmundson E, Stikov N, Etezadi-Amoli M, Stoica P, Nishimura DG (2010) A robust methodology for in vivo T1 mapping. Magn Reson Med 64:1057–1067.

Basser PJ, Mattiello J, LeBihan D (1994a) Estimation of the effective self-diffusion tensor from the NMR spin echo. J Magn Reson B 103:247–254.

Basser PJ, Mattiello J, LeBihan D (1994b) MR diffusion tensor spectroscopy and imaging. Biophys J 66:259–267.

Basser PJ, Pierpaoli C (1996) Microstructural and physiological features of tissues elucidated by quantitative-diffusion-tensor MRI. J Magn Reson B 111:209–219.

Benton AL, Hécaen H (1970) Stereoscopic vision in patients with unilateral cerebral disease. Neurology 20:1084–1084.

Berman S, West KL, Does MD, Yeatman JD, Mezer AA (2018) Evaluating g-ratio weighted changes in the corpus callosum as a function of age and sex. Neuroimage 182:304–313.

Boynton GM, Engel SA, Glover GH, Heeger DJ (1996) Linear systems analysis of functional magnetic resonance imaging in human V1. J Neurosci 16:4207–4221.

Bridge H (2016) Effects of cortical damage on binocular depth perception. Philos Trans R Soc Lond B Biol Sci 371 Available at: http://dx.doi.org/10.1098/rstb.2015.0254.

Bridge H, Parker AJ (2007) Topographical representation of binocular depth in the human visual cortex using fMRI. J Vis 7:15–15.

Bridge H, Thomas OM, Minini L, Cavina-Pratesi C, David Milner A, Parker AJ (2013) Structural and Functional Changes across the Visual Cortex of a Patient with Visual Form Agnosia. J Neurosci 33:12779–12791.

Caan MWA, Bazin P-L, Marques JP, de Hollander G, Dumoulin SO, van der Zwaag W (2019) MP2RAGEME: T , T , and QSM mapping in one sequence at 7 tesla. Hum Brain Mapp 40:1786–1798.

Caiafa CF, Pestilli F (2017) Multidimensional encoding of brain connectomes. Sci Rep 7:11491.

Callaway EM (2005) Structure and function of parallel pathways in the primate early visual system. J Physiol 566:13–19.

Carmon A, Bechtoldt HP (1969) Dominance of the right cerebral hemisphere for stereopsis. Neuropsychologia 7:29–39.

Catani M, Ffytche DH (2005) The rises and falls of disconnection syndromes. Brain 128:2224–2239.

Catani M, Howard RJ, Pajevic S, Jones DK (2002) Virtual in vivo interactive dissection of white matter fasciculi in the human brain. Neuroimage 17:77–94.

Catani M, Thiebaut de Schotten M (2012) Atlas of human brain connections. Oxford University Press.

Cello KE, Nelson-Quigg JM, Johnson CA (2000) Frequency doubling technology perimetry for detection of glaucomatous visual field loss. American Journal of Ophthalmology 129:314–322 Available at: http://dx.doi.org/10.1016/s0002-9394(99)00414-6.

Cercignani M, Dowell NG, Tofts PS (2018) Quantitative MRI of the Brain: Principles of Physical Measurement, Second edition. CRC Press.

Chamberland M, Scherrer B, Prabhu SP, Madsen J, Fortin D, Whittingstall K, Descoteaux M, Warfield SK (2017) Active delineation of Meyer's loop using oriented priors through MAGNEtic tractography (MAGNET). Hum Brain Mapp 38:509–527.

Chang DHF, Mevorach C, Kourtzi Z, Welchman AE (2014) Training transfers the limits on perception from parietal to ventral cortex. Curr Biol 24:2445–2450.

Chase C, Jenner AR (1993) Magnocellular visual deficits affect temporal processing of dyslexics. Ann N Y Acad Sci 682:326–329.

Chopin A, Levi D, Knill D, Bavelier D (2016) The absolute disparity anomaly and the mechanism of relative disparities. J Vis 16:2.

Conway BR (2003) Colour vision: a clue to hue in v2. Curr Biol 13:R308–R310.

Conway BR, Hubel DH, Livingstone MS (2002) Color contrast in macaque V1. Cereb Cortex 12:915–925.

Cottereau BR, McKee SP, Ales JM, Norcia AM (2011) Disparity-tuned population responses from human visual cortex. J Neurosci 31:954–965.

Cowey A, Porter J (1979) Brain damage and global stereopsis. Proc R Soc Lond B Biol Sci 204:399–407.

Csernansky JG, Schindler MK, Splinter NR, Wang L, Gado M, Selemon LD, Rastogi-Cruz D, Posener JA, Thompson PA, Miller MI (2004) Abnormalities of thalamic volume and shape in schizophrenia. Am J Psychiatry 161:896–902.

Cumming BG, Parker AJ (1997) Responses of primary visual cortical neurons to binocular disparity without depth perception. Nature 389:280–283.

Cumming BG, Parker AJ (1999) Binocular neurons in V1 of awake monkeys are selective for absolute, not relative, disparity. J Neurosci 19:5602–5618.

Dejerine J, Dejerine-Klumpke A (1895) Anutomir des cenfres newem. Paris: Rueff et Cie 1:787–788.

Dekker TM, Ban H, van der Velde B, Sereno MI, Welchman AE, Nardini M (2015) Late development of cue integration is linked to sensory fusion in cortex. Curr Biol 25:2856–2861.

Demb JB, Boynton GM, Best M, Heeger DJ (1998) Psychophysical evidence for a magnocellular pathway deficit in dyslexia. Vision Res 38:1555–1559.

De Moraes CG (2013) Anatomy of the visual pathways. J Glaucoma 22 Suppl 5:S2–S7.

Denison RN, Vu AT, Yacoub E, Feinberg DA, Silver MA (2014) Functional mapping of the magnocellular and parvocellular subdivisions of human LGN. Neuroimage 102 Pt 2:358–369.

Derrington AM, Lennie P (1984) Spatial and temporal contrast sensitivities of neurones in lateral geniculate nucleus of macaque. J Physiol 357:219–240.

Desikan RS, Ségonne F, Fischl B, Quinn BT, Dickerson BC, Blacker D, Buckner RL, Dale AM, Maguire RP, Hyman BT, Albert MS, Killiany RJ (2006) An automated labeling system for subdividing the human cerebral cortex on MRI scans into gyral based regions of interest. Neuroimage 31:968–980.

Doi T, Tanabe S, Fujita I (2011) Matching and correlation computations in stereoscopic depth perception. J Vis 11:1.

Dougherty RF, Ben-Shachar M, Deutsch GK, Hernandez A, Fox GR, Wandell BA (2007)

Temporal-callosal pathway diffusivity predicts phonological skills in children. Proc Natl Acad Sci U S A 104:8556–8561.

Duan Y, Norcia AM, Yeatman JD, Mezer A (2015) The Structural Properties of Major White Matter Tracts in Strabismic AmblyopiaMajor White Matter Tracts in Strabismic Amblyopia. Invest Ophthalmol Vis Sci 56:5152–5160.

Dumoulin SO, Wandell BA (2008) Population receptive field estimates in human visual cortex. Neuroimage 39:647–660.

Durand J-B, Peeters R, Norman JF, Todd JT, Orban GA (2009) Parietal regions processing visual 3D shape extracted from disparity. Neuroimage 46:1114–1126.

Duval T, Le Vy S, Stikov N, Campbell J, Mezer A, Witzel T, Keil B, Smith V, Wald LL, Klawiter E, Cohen-Adad J (2017) g-Ratio weighted imaging of the human spinal cord in vivo. Neuroimage 145:11–23.

Eggert GH (1977) Wernicke’s works on aphasia: A sourcebook and review. Mouton de Gruyter.

Farivar R (2009) Dorsal-ventral integration in object recognition. Brain Res Rev 61:144–153.

Faul F, Erdfelder E, Lang A-G, Buchner A (2007) G*Power 3: a flexible statistical power analysis program for the social, behavioral, and biomedical sciences. Behav Res Methods 39:175–191.

Felleman DJ, Van Essen DC (1991) Distributed hierarchical processing in the primate cerebral cortex. Cereb Cortex 1:1–47.

Felmingham KL, Jakobson LS (1995) Visual and visuomotor performance in dyslexic children. Exp Brain Res 106:467–474.

Fields RD (2015) A new mechanism of nervous system plasticity: activity-dependent myelination. Nat Rev Neurosci 16:756–767.

Filo S, Shtangel O, Salamon N, Kol A, Weisinger B, Shifman S, Mezer AA (2019) Disentangling molecular alterations from water-content changes in the aging human brain using quantitative MRI. Nature Communications 10 Available at: http://dx.doi.org/10.1038/s41467-019-11319-1.

Fischl B (2012) FreeSurfer. Neuroimage 62:774–781.

Fischl B, Dale AM (2000) Measuring the thickness of the human cerebral cortex from magnetic resonance images. Proc Natl Acad Sci U S A 97:11050–11055.

Fonov V, Evans AC, Botteron K, Almli CR, McKinstry RC, Collins DL, Brain Development Cooperative Group (2011) Unbiased average age-appropriate atlases for pediatric studies. Neuroimage 54:313–327.

Fonov VS, Evans AC, McKinstry RC, Almli CR, Collins DL (2009) Unbiased nonlinear average age-appropriate brain templates from birth to adulthood. NeuroImage 47:S102 Available at: http://dx.doi.org/10.1016/s1053-8119(09)70884-5.

Forstmann BU, de Hollander G, van Maanen L, Alkemade A, Keuken MC (2016) Towards a mechanistic understanding of the human subcortex. Nat Rev Neurosci 18:57.

Fraley C, Raftery AE (1998) How Many Clusters? Which Clustering Method? Answers Via

Model-Based Cluster Analysis. Comput J 41:578–588.

Friston KJ, Fletcher P, Josephs O, Holmes A, Rugg MD, Turner R (1998) Event-related fMRI: characterizing differential responses. Neuroimage 7:30–40.

Fujita I, Doi T (2016) Weighted parallel contributions of binocular correlation and match signals to conscious perception of depth. Philos Trans R Soc Lond B Biol Sci 371 Available at: http://dx.doi.org/10.1098/rstb.2015.0257.

Fukunaga M, Li T-Q, van Gelderen P, de Zwart JA, Shmueli K, Yao B, Lee J, Maric D, Aronova MA, Zhang G, Leapman RD, Schenck JF, Merkle H, Duyn JH (2010) Layer-specific variation of iron content in cerebral cortex as a source of MRI contrast. Proc Natl Acad Sci U S A 107:3834–3839.

Genç E, Bergmann J, Singer W, Kohler A (2011) Interhemispheric connections shape subjective experience of bistable motion. Curr Biol 21:1494–1499.

Georgieva S, Peeters R, Kolster H, Todd JT, Orban GA (2009) The processing of three-dimensional shape from disparity in the human brain. J Neurosci 29:727–742.

Gillebert CR, Schaeverbeke J, Bastin C, Neyens V, Bruffaerts R, De Weer A-S, Seghers A, Sunaert S, Van Laere K, Versijpt J, Vandenbulcke M, Salmon E, Todd JT, Orban GA, Vandenberghe R (2015) 3D Shape Perception in Posterior Cortical Atrophy: A Visual Neuroscience Perspective. J Neurosci 35:12673–12692.

Giraldo-Chica M, Hegarty JP 2nd, Schneider KA (2015) Morphological differences in the lateral geniculate nucleus associated with dyslexia. Neuroimage Clin 7:830–836.

Giraldo-Chica M, Schneider KA (2018) Hemispheric asymmetries in the orientation and location of the lateral geniculate nucleus in dyslexia. Dyslexia 24:197–203.

Glasser MF, Coalson TS, Robinson EC, Hacker CD, Harwell J, Yacoub E, Ugurbil K, Andersson J, Beckmann CF, Jenkinson M, Smith SM, Van Essen DC (2016) A multi-modal parcellation of human cerebral cortex. Nature 536:171–178.

Glasser MF, Sotiropoulos SN, Wilson JA, Coalson TS, Fischl B, Andersson JL, Xu J, Jbabdi S, Webster M, Polimeni JR, Van Essen DC, Jenkinson M, Consortium, W. U-Minn HCP (2013) The minimal preprocessing pipelines for the Human Connectome Project. Neuroimage 80:105–124.

Glasser MF, Van Essen DC (2011) Mapping human cortical areas in vivo based on myelin content as revealed by T1- and T2-weighted MRI. J Neurosci 31:11597–11616.

Gomez J, Barnett MA, Natu V, Mezer A, Palomero-Gallagher N, Weiner KS, Amunts K, Zilles K, Grill-Spector K (2017) Microstructural proliferation in human cortex is coupled with the development of face processing. Science 355:68–71.

Gomez J, Pestilli F, Witthoft N, Golarai G, Liberman A, Poltoratski S, Yoon J, Grill-Spector K (2015) Functionally Defined White Matter Reveals Segregated Pathways in Human Ventral Temporal Cortex Associated with Category-Specific Processing. Neuron 85:216–227.

Gonzalez F, Perez R (1998) Neural mechanisms underlying stereoscopic vision. Prog Neurobiol 55:191–224.

Goodale MA, Milner AD (1992) Separate visual pathways for perception and action. Trends Neurosci 15:20–25.

Goodale MA, Milner AD, Jakobson LS, Carey DP (1991) A neurological dissociation between perceiving objects and grasping them. Nature 349:154–156.

Guillery RW, Colonnier M (1970) Synaptic patterns in the dorsal lateral geniculate nucleus of the monkey. Z Zellforsch Mikrosk Anat 103:90–108.

Hagiwara A, Hori M, Kamagata K, Warntjes M, Matsuyoshi D, Nakazawa M, Ueda R, Andica C, Koshino S, Maekawa T, Irie R, Takamura T, Kumamaru KK, Abe O, Aoki S (2018) Myelin Measurement: Comparison Between Simultaneous Tissue Relaxometry, Magnetization Transfer Saturation Index, and Tw/Tw Ratio Methods. Sci Rep 8:10554.

Hamsher KD (1978) Stereopsis and unilateral brain disease. Invest Ophthalmol Vis Sci 17:336–343.

Hassler R (1966) Comparative Anatomy of the Central Visual Systems in Day- and Night-active Primates. Evolution of the Forebrain:419–434 Available at: http://dx.doi.org/10.1007/978-1-4899-6527-1_40.

Haynes J-D, Deichmann R, Rees G (2005) Eye-specific effects of binocular rivalry in the human lateral geniculate nucleus. Nature 438:496–499.

Heeger DJ (1999) Linking visual perception with human brain activity. Curr Opin Neurobiol 9:474–479.

Hendry SHC, Clay Reid R (2000) The Koniocellular Pathway in Primate Vision. Annual Review of Neuroscience 23:127–153 Available at: http://dx.doi.org/10.1146/annurev.neuro.23.1.127.

Hess RF, To L, Zhou J, Wang G, Cooperstock JR (2015) Stereo Vision: The Haves and Have-Nots. Iperception 6:2041669515593028.

Heywood CA, Cowey A (1987) On the role of cortical area V4 in the discrimination of hue and pattern in macaque monkeys. J Neurosci 7:2601–2617.

Hibbard PB, Scott-Brown KC, Haigh EC, Adrain M (2014) Depth Perception Not Found in Human Observers for Static or Dynamic Anti-Correlated Random Dot Stereograms. PLoS ONE 9:e84087 Available at: http://dx.doi.org/10.1371/journal.pone.0084087.

Hickey TL, Guillery RW (1979) Variability of laminar patterns in the human lateral geniculate nucleus. J Comp Neurol 183:221–246.

Howard IP, Rogers BJ (1995) Binocular Vision and Stereopsis. Oxford University Press.

Huang H, Zhang J, Jiang H, Wakana S, Poetscher L, Miller MI, van Zijl PCM, Hillis AE, Wytik R, Mori S (2005) DTI tractography based parcellation of white matter: Application to the mid-sagittal morphology of corpus callosum. Neuroimage 26:195–205.

Hubel DH, Livingstone MS (1987) Segregation of form, color, and stereopsis in primate area 18. J Neurosci 7:3378–3415.

Hubel DH, Wiesel TN (1959) Receptive fields of single neurones in the cat’s striate cortex. J Physiol 148:574–591.

Hubel DH, Wiesel TN (1962) Receptive fields, binocular interaction and functional architecture in the cat’s visual cortex. J Physiol 160:106–154.

Huber E, Donnelly PM, Rokem A, Yeatman JD (2018a) Rapid and widespread white matter plasticity during an intensive reading intervention. Nature Communications 9 Available at: http://dx.doi.org/10.1038/s41467-018-04627-5.

Huber L, Ivanov D, Handwerker DA, Marrett S, Guidi M, Uludağ K, Bandettini PA, Poser BA (2018b) Techniques for blood volume fMRI with VASO: From low-resolution mapping towards sub-millimeter layer-dependent applications. Neuroimage 164:131–143.

Huber L, Ivanov D, Krieger SN, Streicher MN, Mildner T, Poser BA, Möller HE, Turner R (2014) Slab-selective, BOLD-corrected VASO at 7 Tesla provides measures of cerebral blood volume reactivity with high signal-to-noise ratio. Magn Reson Med 72:137–148.

Hughes SW, Lörincz M, Cope DW, Blethyn KL, Kékesi KA, Parri HR, Juhász G, Crunelli V (2004) Synchronized oscillations at alpha and theta frequencies in the lateral geniculate nucleus. Neuron 42:253–268.

Ip IB, Minini L, Dow J, Parker AJ, Bridge H (2014) Responses to interocular disparity correlation in the human cerebral cortex. Ophthalmic Physiol Opt 34:186–198.

Ives HE (1912) XII. Studies in the photometry of lights of different colours. The London, Edinburgh, and Dublin Philosophical Magazine and Journal of Science 24:149–188 Available at: http://dx.doi.org/10.1080/14786440708637317.

Janssen P, Vogels R, Liu Y, Orban GA (2003) At least at the level of inferior temporal cortex, the stereo correspondence problem is solved. Neuron 37:693–701.

Janssen P, Vogels R, Orban GA (1999) Macaque inferior temporal neurons are selective for disparity-defined three-dimensional shapes. Proc Natl Acad Sci U S A 96:8217–8222.

Jenkinson M, Bannister P, Brady M, Smith S (2002) Improved optimization for the robust and accurate linear registration and motion correction of brain images. Neuroimage 17:825–841.

Joffe KM, Raymond JE, Chrichton A (1997) Motion coherence perimetry in glaucoma and suspected glaucoma. Vision Res 37:955–964.

Jones DK, Knosche TR, Turner R (2013) White matter integrity, fiber count, and other fallacies: the do’s and don'ts of diffusion MRI. Neuroimage 73:239–254.

Julesz B (1960) Binocular depth perception of computer-generated patterns. Bell Syst tech j 39:1125–1162.

Julesz B (1971) Foundations of cyclopean perception. University of Chicago Press.

Kanai R, Rees G (2011) The structural basis of inter-individual differences in human behaviour and cognition. Nat Rev Neurosci 12:231–242.

Kaneko T, Takemura H, Pestilli F, Silva AC, Ye FQ, Leopold DA (2020) Spatial organization of occipital white matter tracts in the common marmoset. Brain Struct Funct 225:1313–1326.

Kay K, Jamison KW, Vizioli L, Zhang R, Margalit E, Ugurbil K (2019) A critical assessment of data quality and venous effects in sub-millimeter fMRI. Neuroimage 189:847–869.

Kay K, Jamison KW, Zhang R-Y, Uğurbil K (2020) A temporal decomposition method for identifying venous effects in task-based fMRI. Nat Methods 17:1033–1039.

Keuken MC, Bazin P-L, Backhouse K, Beekhuizen S, Himmer L, Kandola A, Lafeber JJ, Prochazkova L, Trutti A, Schäfer A, Turner R, Forstmann BU (2017) Effects of aging on $T_1 T 1 , T_2^*$ T 2 ∗ , and QSM MRI values in the subcortex. Brain Structure and Function 222:2487–2505 Available at: http://dx.doi.org/10.1007/s00429-016-1352-4.

Kornblith S, Cheng X, Ohayon S, Tsao DY (2013) A network for scene processing in the macaque temporal lobe. Neuron 79:766–781.

Levin N, Dumoulin SO, Winawer J, Dougherty RF, Wandell BA (2010) Cortical maps and white matter tracts following long period of visual deprivation and retinal image restoration. Neuron 65:21–31.

Ling S, Pratte MS, Tong F (2015) Attention alters orientation processing in the human lateral geniculate nucleus. Nature Neuroscience 18:496–498 Available at: http://dx.doi.org/10.1038/nn.3967.

Liu Z, de Zwart JA, Yao B, van Gelderen P, Kuo L-W, Duyn JH (2012) Finding thalamic BOLD correlates to posterior alpha EEG. Neuroimage 63:1060–1069.

Livingstone M, Hubel D (1988) Segregation of form, color, movement, and depth: anatomy, physiology, and perception. Science 240:740–749.

Li X, Zhu Q, Janssens T, Arsenault JT, Vanduffel W (2019) In vivo identification of thick, thin, and pale stripes of macaque area V2 using submillimeter resolution (f) MRI at 3 T. Cereb Cortex 29:544–560.

Lutti A, Dick F, Sereno MI, Weiskopf N (2014) Using high-resolution quantitative mapping of R1 as an index of cortical myelination. Neuroimage 93 Pt 2:176–188.

Maddess TL, Henry GH, Others (1992) Performance of nonlinear visual units in ocular hypertension and glaucoma. Available at: https://openresearch-repository.anu.edu.au/handle/1885/11562.

Ma D, Gulani V, Seiberlich N, Liu K, Sunshine JL, Duerk JL, Griswold MA (2013) Magnetic resonance fingerprinting. Nature 495:187–192.

Main KL, Pestilli F, Mezer A, Yeatman J, Martin R, Phipps S, Wandell B (2014) Speed discrimination predicts word but not pseudo-word reading rate in adults and children. Brain Lang 138:27–37.

Makin TR, de Xivry J-JO (2019) Science Forum: Ten common statistical mistakes to watch out for when writing or reviewing a manuscript. Elife 8:e48175.

Mante V, Frazor RA, Bonin V, Geisler WS, Carandini M (2005) Independence of luminance and contrast in natural scenes and in the early visual system. Nat Neurosci 8:1690–1697.

Marques JP, Kober T, Krueger G, van der Zwaag W, Van de Moortele P-F, Gruetter R (2010) MP2RAGE, a self bias-field corrected sequence for improved segmentation and T1-mapping at high field. Neuroimage 49:1271–1281.

Martino J, García-Porrero JA (2013) Wernicke perpendicular fasciculus and vertical portion of the superior longitudinal fasciculus: in reply. Neurosurgery 73:E382–E383.

Masson GS, Busettini C, Miles FA (1997) Vergence eye movements in response to binocular disparity without depth perception. Nature 389:283–286.

Maunsell JH, Ghose GM, Assad JA, McAdams CJ, Boudreau CE, Noerager BD (1999)

Visual response latencies of magnocellular and parvocellular LGN neurons in macaque monkeys. Vis Neurosci 16:1–14.

Mcketton L, Kelly KR, Schneider KA (2014) Abnormal lateral geniculate nucleus and optic chiasm in human albinism. Journal of Comparative Neurology 522:2680–2687 Available at: http://dx.doi.org/10.1002/cne.23565.

Mezer A, Rokem A, Berman S, Hastie T, Wandell BA (2016) Evaluating quantitative proton-density-mapping methods. Hum Brain Mapp 37:3623–3635.

Mezer A, Yeatman JD, Stikov N, Kay KN, Cho NJ, Dougherty RF, Perry ML, Parvizi J, Hua le H, Butts-Pauly K, Wandell BA (2013) Quantifying the local tissue volume and composition in individual brains with magnetic resonance imaging. Nat Med 19:1667–1672.

Minami S, Amano K (2017) Illusory Jitter Perceived at the Frequency of Alpha Oscillations. Curr Biol 27:2344–2351.e4.

Minami S, Oishi H, Takemura H, Amano K (2020) Inter-individual Differences in Occipital Alpha Oscillations Correlate with White Matter Tissue Properties of the Optic Radiation. eNeuro 7 Available at: http://dx.doi.org/10.1523/ENEURO.0224-19.2020.

Minini L, Parker AJ, Bridge H (2010) Neural modulation by binocular disparity greatest in human dorsal visual stream. J Neurophysiol 104:169–178.

Moeller S, Yacoub E, Olman CA, Auerbach E, Strupp J, Harel N, Uğurbil K (2010) Multiband multislice GE-EPI at 7 tesla, with 16-fold acceleration using partial parallel imaging with application to high spatial and temporal whole-brain fMRI. Magn Reson Med 63:1144–1153.

Mori S, Crain BJ, Chacko VP, van Zijl PC (1999) Three-dimensional tracking of axonal projections in the brain by magnetic resonance imaging. Ann Neurol 45:265–269.

Movshon JA, Chambers BE, Blakemore C (1972) Interocular transfer in normal humans, and those who lack stereopsis. Perception 1:483–490.

Müller-Axt C, Eichner C, Rusch H, Kauffmann L, Bazin P-L, Anwander A, Morawski M, von Kriegstein K (n.d.) Mapping the Human Visual Thalamus and its Cytoarchitectonic Subdivisions Using Quantitative MRI. Available at: http://dx.doi.org/10.1101/2020.08.14.250779.

Murphy AP, Leopold DA, Humphreys GW, Welchman AE (2016) Lesions to right posterior parietal cortex impair visual depth perception from disparity but not motion cues. Philos Trans R Soc Lond B Biol Sci 371 Available at: http://dx.doi.org/10.1098/rstb.2015.0263.

Nassi JJ, Callaway EM (2009) Parallel processing strategies of the primate visual system. Nat Rev Neurosci 10:360–372.

Neri P, Bridge H, Heeger DJ (2004) Stereoscopic processing of absolute and relative disparity in human visual cortex. J Neurophysiol 92:1880–1891.

Nishida Y, Hayashi O, Iwami T, Kimura M, Kani K, Ito R, Shiino A, Suzuki M (2001) Stereopsis-processing regions in the human parieto-occipital cortex. Neuroreport 12:2259.

O’Connor DH, Fukui MM, Pinsk MA, Kastner S (2002) Attention modulates responses in the human lateral geniculate nucleus. Nat Neurosci 5:1203–1209.

Ogawa S, Takemura H, Horiguchi H, Terao M, Haji T, Pestilli F, Yeatman JD, Tsuneoka H, Wandell BA, Masuda Y (2014) White matter consequences of retinal receptor and ganglion cell damage. Invest Ophthalmol Vis Sci 55:6976–6986.

Ohzawa I, DeAngelis GC, Freeman RD (1990) Stereoscopic depth discrimination in the visual cortex: neurons ideally suited as disparity detectors. Science 249:1037–1041.

Ohzawa I, DeAngelis GC, Freeman RD (1997) Encoding of binocular disparity by complex cells in the cat's visual cortex. J Neurophysiol 77:2879–2909.

Oishi H, Takemura H, Aoki SC, Fujita I, Amano K (2018) Microstructural properties of the vertical occipital fasciculus explain the variability in human stereoacuity. Proc Natl Acad Sci U S A 115:12289–12294.

Okazawa G, Tajima S, Komatsu H (2015) Image statistics underlying natural texture selectivity of neurons in macaque V4. Proc Natl Acad Sci U S A 112:E351–E360.

Orban GA, Janssen P, Vogels R (2006) Extracting 3D structure from disparity. Trends Neurosci 29:466–473.

Parker AJ (2007) Binocular depth perception and the cerebral cortex. Nat Rev Neurosci 8:379–391.

Pestilli F, Yeatman JD, Rokem A, Kay KN, Wandell BA (2014) Evaluation and statistical inference for human connectomes. Nat Methods 11:1058–1063.

Pistorio AL, Hendry SH, Wang X (2006) A modified technique for high-resolution staining of myelin. J Neurosci Methods 153:135–146.

Preston TJ, Li S, Kourtzi Z, Welchman AE (2008) Multivoxel pattern selectivity for perceptually relevant binocular disparities in the human brain. J Neurosci 28:11315–11327.

Ptito A, Zatorre RJ, Larson WL, Tosoni C (1991) Stereopsis after unilateral anterior temporal lobectomy. Dissociation between local and global measures. Brain 114 (Pt 3):1323–1333.

Qian N, Zhu Y (1997) Physiological computation of binocular disparity. Vision Res 37:1811–1827.

Read JCA, Phillipson GP, Serrano-Pedraza I, Milner AD, Parker AJ (2010) Stereoscopic vision in the absence of the lateral occipital cortex. PLoS One 5:e12608.

Reveley C, Seth AK, Pierpaoli C, Silva AC, Yu D, Saunders RC, Leopold DA, Ye FQ (2015) Superficial white matter fiber systems impede detection of long-range cortical connections in diffusion MR tractography. Proc Natl Acad Sci U S A 112:E2820–E2828.

Richards W (1970) Stereopsis and stereoblindness. Experimental Brain Research 10:380–388 Available at: http://dx.doi.org/10.1007/bf02324765.

Rohde GK, Barnett AS, Basser PJ, Marenco S, Pierpaoli C (2004) Comprehensive approach for correction of motion and distortion in diffusion-weighted MRI. Magn Reson Med 51:103–114.

Rokem A, Takemura H, Bock AS, Scherf KS, Behrmann M, Wandell BA, Fine I, Bridge H, Pestilli F (2017) The visual white matter: The application of diffusion MRI and fiber tractography to vision science. J Vis 17:4.

Ross JE (1983) Disturbance of stereoscopic vision in patients with unilateral stroke. Behav Brain Res 7:99–112.

Sachs H (1892) Das Hemisphärenmark des menschlichen Grosshirns: Der Hinterhauptlappen/von Heinrich Sachs.

Sakata H, Taira M, Kusunoki M, Murata A, Tanaka Y (1997) The TINS Lecture. The parietal association cortex in depth perception and visual control of hand action. Trends Neurosci 20:350–357.

Sampaio-Baptista C, Johansen-Berg H (2017) White Matter Plasticity in the Adult Brain. Neuron 96:1239–1251.

Sampaio-Baptista C, Khrapitchev AA, Foxley S, Schlagheck T, Scholz J, Jbabdi S, DeLuca GC, Miller KL, Taylor A, Thomas N, Kleim J, Sibson NR, Bannerman D, Johansen-Berg H (2013) Motor skill learning induces changes in white matter microstructure and myelination. J Neurosci 33:19499–19503.

Scherf KS, Thomas C, Doyle J, Behrmann M (2014) Emerging structure-function relations in the developing face processing system. Cereb Cortex 24:2964–2980.

Schiller PH, Logothetis NK, Charles ER (1990) Functions of the colour-opponent and broad-band channels of the visual system. Nature 343:68–70.

Schneider KA, Kastner S (2009) Effects of sustained spatial attention in the human lateral geniculate nucleus and superior colliculus. J Neurosci 29:1784–1795.

Schneider KA, Richter MC, Kastner S (2004) Retinotopic organization and functional subdivisions of the human lateral geniculate nucleus: a high-resolution functional magnetic resonance imaging study. J Neurosci 24:8975–8985.

Scholz J, Klein MC, Behrens TEJ, Johansen-Berg H (2009) Training induces changes in white-matter architecture. Nat Neurosci 12:1370–1371.

Selemon LD, Begovic A (2007) Stereologic analysis of the lateral geniculate nucleus of the thalamus in normal and schizophrenic subjects. Psychiatry Res 151:1–10.

Sereno MI, Lutti A, Weiskopf N, Dick F (2013) Mapping the human cortical surface by combining quantitative T(1) with retinotopy. Cereb Cortex 23:2261–2268.

Setsompop K, Cohen-Adad J, Gagoski BA, Raij T, Yendiki A, Keil B, Wedeen VJ, Wald LL (2012) Improving diffusion MRI using simultaneous multi-slice echo planar imaging. Neuroimage 63:569–580.

Shams Z, Norris DG, Marques JP (2019) A comparison of in vivo MRI based cortical myelin mapping using T1w/T2w and R1 mapping at 3T. PLoS One 14:e0218089.

Shapley R, Hawken MJ (2011) Color in the cortex: single- and double-opponent cells. Vision Res 51:701–717.

Sherbondy AJ, Dougherty RF, Ben-Shachar M, Napel S, Wandell BA (2008a) ConTrack: finding the most likely pathways between brain regions using diffusion tractography. J Vis 8:15 1–16.

Sherbondy AJ, Dougherty RF, Napel S, Wandell BA (2008b) Identifying the human optic radiation using diffusion imaging and fiber tractography. J Vis 8.

Shiozaki HM, Tanabe S, Doi T, Fujita I (2012a) Neural activity in cortical area V4 underlies fine disparity discrimination. J Neurosci 32:3830–3841.

Shiozaki HM, Tanabe S, Doi T, Fujita I (2012b) Neural Activity in Cortical Area V4 Underlies Fine Disparity Discrimination. J Neurosci 32:3830–3841.

Shtangel O, Mezer AA (2020) A phantom system for assessing the effects of membrane lipids on water proton relaxation. NMR Biomed 33:e4209.

Simoncelli EP, Heeger DJ (1998) A model of neuronal responses in visual area MT. Vision Res 38:743–761.

Smith RE, Tournier JD, Calamante F, Connelly A (2012) Anatomically-constrained tractography: improved diffusion MRI streamlines tractography through effective use of anatomical information. Neuroimage 62:1924–1938.

Stein J (2001) The magnocellular theory of developmental dyslexia. Dyslexia 7:12–36 Available at: http://dx.doi.org/10.1002/dys.186.

Stuber C, Morawski M, Schafer A, Labadie C, Wahnert M, Leuze C, Streicher M, Barapatre N, Reimann K, Geyer S, Spemann D, Turner R (2014) Myelin and iron concentration in the human brain: a quantitative study of MRI contrast. Neuroimage 93 Pt 1:95–106.

Tabelow K, Balteau E, Ashburner J, Callaghan MF, Draganski B, Helms G, Kherif F, Leutritz T, Lutti A, Phillips C, Reimer E, Ruthotto L, Seif M, Weiskopf N, Ziegler G, Mohammadi S (2019) hMRI - A toolbox for quantitative MRI in neuroscience and clinical research. Neuroimage 194:191–210.

Takemura H, Caiafa CF, Wandell BA, Pestilli F (2016a) Ensemble Tractography. PLoS Comput Biol 12:e1004692.

Takemura H, Ogawa S, Mezer AA, Horiguchi H, Miyazaki A, Matsumoto K, Shikishima K, Nakano T, Masuda Y (2019) Diffusivity and quantitative T1 profile of human visual white matter tracts after retinal ganglion cell damage. Neuroimage Clin 23:101826.

Takemura H, Pestilli F, Weiner KS, Keliris GA, Landi SM, Sliwa J, Ye FQ, Barnett MA, Leopold DA, Freiwald WA, Logothetis NK, Wandell BA (2017) Occipital White Matter Tracts in Human and Macaque. Cereb Cortex 27:3346–3359.

Takemura H, Rokem A, Winawer J, Yeatman JD, Wandell BA, Pestilli F (2016b) A major human white-matter pathway between dorsal and ventral visual cortex. Cereb Cortex 26:2205–2214.

Takemura H, Rokem A, Winawer J, Yeatman JD, Wandell BA, Pestilli F (2016c) A Major Human White Matter Pathway Between Dorsal and Ventral Visual Cortex. Cereb Cortex 26:2205–2214.

Takemura H, Yuasa K, Amano K (2020) Predicting Neural Response Latency of the Human Early Visual Cortex from MRI-Based Tissue Measurements of the Optic Radiation. eNeuro 7 Available at: http://dx.doi.org/10.1523/ENEURO.0545-19.2020.

Tanabe S, Umeda K, Fujita I (2004) Rejection of false matches for binocular correspondence in macaque visual cortical area V4. J Neurosci 24:8170–8180.

Tanabe S, Yasuoka S, Fujita I (2008) Disparity-energy signals in perceived stereoscopic depth. J Vis 8:22.1–10.

Tanaka H, Uka T, Yoshiyama K, Kato M, Fujita I (2001) Processing of shape defined by disparity in monkey inferior temporal cortex. J Neurophysiol 85:735–744.

Tavor I, Yablonski M, Mezer A, Rom S, Assaf Y, Yovel G (2014) Separate parts of occipito-temporal white matter fibers are associated with recognition of faces and places. Neuroimage 86:123–130.

Thiebaut de Schotten M, Dell'Acqua F, Forkel SJ, Simmons A, Vergani F, Murphy DG, Catani M (2011) A lateralized brain network for visuospatial attention. Nat Neurosci 14:1245–1246.

Thomason ME, Thompson PM (2011) Diffusion imaging, white matter, and psychopathology. Annu Rev Clin Psychol 7:63–85.

Tournier JD, Calamante F, Connelly A (2007) Robust determination of the fibre orientation distribution in diffusion MRI: non-negativity constrained super-resolved spherical deconvolution. Neuroimage 35:1459–1472.

Tournier JD, Calamante F, Connelly A (2012) MRtrix: Diffusion tractography in crossing fiber regions. Int J Imaging Syst Technol 22:53–66.

Tournier J-D, Calamante F, Gadian DG, Connelly A (2004) Direct estimation of the fiber orientation density function from diffusion-weighted MRI data using spherical deconvolution. Neuroimage 23:1176–1185.

Tsao DY, Vanduffel W, Sasaki Y, Fize D, Knutsen TA, Mandeville JB, Wald LL, Dale AM, Rosen BR, Van Essen DC, Livingstone MS, Orban GA, Tootell RB (2003) Stereopsis activates V3A and caudal intraparietal areas in macaques and humans. Neuron 39:555–568.

Uddin MN, Figley TD, Marrie RA, Figley CR, CCOMS Study Group (2018) Can T w/T w ratio be used as a myelin-specific measure in subcortical structures? Comparisons between FSE-based T w/T w ratios, GRASE-based T w/T w ratios and multi-echo GRASE-based myelin water fractions. NMR Biomed 31 Available at: http://dx.doi.org/10.1002/nbm.3868.

Uesaki M, Takemura H, Ashida H (2017) Computational neuroanatomy of human stratum proprium of interparietal sulcus. Brain Struct Funct Available at: http://dx.doi.org/10.1007/s00429-017-1492-1.

Uka T, DeAngelis GC (2006a) Linking neural representation to function in stereoscopic depth perception: roles of the middle temporal area in coarse versus fine disparity discrimination. J Neurosci 26:6791–6802.

Uka T, DeAngelis GC (2006b) Linking neural representation to function in stereoscopic depth perception: roles of the middle temporal area in coarse versus fine disparity discrimination. J Neurosci 26:6791–6802.

Uka T, Tanabe S, Watanabe M, Fujita I (2005) Neural correlates of fine depth discrimination in monkey inferior temporal cortex. J Neurosci 25:10796–10802.

Uka T, Tanaka H, Yoshiyama K, Kato M, Fujita I (2000) Disparity selectivity of neurons in monkey inferior temporal cortex. J Neurophysiol 84:120–132.

Uludağ K, Blinder P (2018) Linking brain vascular physiology to hemodynamic response in ultra-high field MRI. Neuroimage 168:279–295.

Ungerleider LG, Galkin TW, Desimone R, Gattass R (2008) Cortical connections of area V4 in the macaque. Cereb Cortex 18:477–499.

Usrey WM, Reid RC (2000) Visual physiology of the lateral geniculate nucleus in two species of new world monkey: Saimiri sciureus and Aotus trivirgatis. J Physiol 523 Pt 3:755–769.

Van Essen DC, Anderson CH, Felleman DJ (1992) Information processing in the primate visual system: an integrated systems perspective. Science 255:419–423.

Viviano JD, Schneider KA (2015) Interhemispheric interactions of the human thalamic reticular nucleus. J Neurosci 35:2026–2032.

Wakana S, Jiang H, Nagae-Poetscher LM, van Zijl PCM, Mori S (2004) Fiber tract-based atlas of human white matter anatomy. Radiology 230:77–87.

Wandell BA (2016) Clarifying Human White Matter. Annu Rev Neurosci 39:103–128.

Wandell BA, Dumoulin SO, Brewer AA (2007) Visual field maps in human cortex. Neuron 56:366–383.

Wandell BA, Le RK (2017) Diagnosing the Neural Circuitry of Reading. Neuron 96:298–311.

Wandell BA, Yeatman JD (2013) Biological development of reading circuits. Curr Opin Neurobiol 23:261–268.

Wang L, Mruczek REB, Arcaro MJ, Kastner S (2015) Probabilistic Maps of Visual Topography in Human Cortex. Cereb Cortex 25:3911–3931.

Warntjes JBM, Leinhard OD, West J, Lundberg P (2008) Rapid magnetic resonance quantification on the brain: Optimization for clinical usage. Magn Reson Med 60:320–329.

Weiskopf N, Mohammadi S, Lutti A, Callaghan MF (2015) Advances in MRI-based computational neuroanatomy: from morphometry to in-vivo histology. Curr Opin Neurol 28:313–322.

Welchman AE (2016) The human brain in depth: How we see in 3D. Annu Rev Vis Sci 2:345–376.

Wernicke C (1881) Lehrbuch der Gehirnkrankheiten für Aerzte und Studirende. Fischer.

Westheimer G (1979) Cooperative neural processes involved in stereoscopic acuity. Exp Brain Res 36:585–597.

Wheatstone C (1843) Contributions to the physiology of vision.—Part the first. On some remarkable and hitherto unobserved phenomena of binocular vision. Abstracts of the Papers Printed in the Philosophical Transactions of the Royal Society of London 4:76–77.

Wichmann FA, Hill NJ (2001) The psychometric function: I. Fitting, sampling, and goodness of fit. Percept Psychophys 63:1293–1313.

Williams RW, Rakic P (1988) Elimination of neurons from the rhesus monkey’s lateral geniculate nucleus during development. J Comp Neurol 272:424–436.

Xiao Y, Wang Y, Felleman DJ (2003) A spatially organized representation of colour in macaque cortical area V2. Nature 421:535–539.

Yeatman JD, Dougherty RF, Ben-Shachar M, Wandell BA (2012a) Development of white matter and reading skills. Proc Natl Acad Sci U S A 109:E3045–E3053.

Yeatman JD, Dougherty RF, Myall NJ, Wandell BA, Feldman HM (2012b) Tract profiles of white matter properties: automating fiber-tract quantification. PLoS One 7:e49790.

Yeatman JD, Dougherty RF, Rykhlevskaia E, Sherbondy AJ, Deutsch GK, Wandell BA, Ben-Shachar M (2011) Anatomical properties of the arcuate fasciculus predict phonological and reading skills in children. J Cogn Neurosci 23:3304–3317.

Yeatman JD, Rauschecker AM, Wandell BA (2013) Anatomy of the visual word form area: adjacent cortical circuits and long-range white matter connections. Brain Lang 125:146–155.

Yeatman JD, Wandell BA, Mezer AA (2014a) Lifespan maturation and degeneration of human brain white matter. Nat Commun 5:4932.

Yeatman JD, Weiner KS, Pestilli F, Rokem A, Mezer A, Wandell BA (2014b) The vertical occipital fasciculus: a century of controversy resolved by in vivo measurements. Proc Natl Acad Sci U S A 111:E5214–E5223.

Yeatman JD, Weiner KS, Pestilli F, Rokem A, Mezer A, Wandell BA (2014c) The Vertical Occipital Fasciculus: A Lost Highway. Proc Natl Acad Sci U S A.

Yeshurun Y, Levy L (2003) Transient spatial attention degrades temporal resolution. Psychol Sci 14:225–231.

Yoonessi A, Yoonessi A (2011) Functional assessment of magno, parvo and konio-cellular pathways; current state and future clinical applications. J Ophthalmic Vis Res 6:119–126.

Yücel YH, Zhang Q, Gupta N, Kaufman PL, Weinreb RN (2000) Loss of neurons in magnocellular and parvocellular layers of the lateral geniculate nucleus in glaucoma. Arch Ophthalmol 118:378–384.

Yücel YH, Zhang Q, Weinreb RN, Kaufman PL, Gupta N (2003) Effects of retinal ganglion cell loss on magno-, parvo-, koniocellular pathways in the lateral geniculate nucleus and visual cortex in glaucoma. Prog Retin Eye Res 22:465–481.

Yu Q, Zhang P, Qiu J, Fang F (2016) Perceptual Learning of Contrast Detection in the Human Lateral Geniculate Nucleus. Curr Biol 26:3176–3182.

Zalta EN, Nodelman U, Allen C, Perry J (1995) Stanford encyclopedia of philosophy. Available at: http://ruccs.rutgers.edu/images/personal-zenon-pylyshyn/class-info/Consciousness_2014/StanfordEncyclopedia/consciousness-temporal_sc.pdf.

Zaroff CM, Knutelska M, Frumkes TE (2003) Variation in Stereoacuity: Normative Description, Fixation Disparity, and the Roles of Aging and Gender. Invest Ophthalmol Vis Sci 44:891–900.

Zhang P, Wen W, Sun X, He S (2016) Selective reduction of fMRI responses to transient achromatic stimuli in the magnocellular layers of the LGN and the superficial layer of the SC of early glaucoma patients. Hum Brain Mapp 37:558–569.

Zhang P, Zhou H, Wen W, He S (2015) Layer-specific response properties of the human lateral geniculate nucleus and superior colliculus. Neuroimage 111:159–166.

Chapter 6.

Acknowledgement

I am indebted to Dr. Kaoru Amano for his comprehensive support and guiding the works in this dissertation. He is a great advisor not only for research but also for my life. Conversations with him in and out of the lab gave me great inspiration. He lectured me about how to do shrewd research.

I am also thankful to Dr. Toshio Yanagida for making a good research environment at CiNet.

Many thanks to Dr. Hiromasa Takemura for always providing suitable advice. He lectured me about the basis of the most of the current dissertation works, including MRI analysis.

I would like to thank Dr. Ichiro Fujita. The work written in the current dissertation is a product collaborating with him. But the most important thing is his exciting lecture led me into the field of cognitive neuroscience. I realised cognitive neuroscience is interesting by his lecture.

I am grateful to Dr. Shuntaro C. Aoki. I learned how to set up and do a psychophysical experiment from him. I enjoyed break time by chatting with him on occasion.

I am thankful to Dr. Hiroshi Ban. He told me essential tips about how to set up MRI and psychophysical experiments. His research toolbox is sophisticated and always helpful for me. I could learn many neuroscience knowledge by talking with him.

I would like to thank my lecturers. I learned computational visual neuroscience from Dr. Izumi Ohzawa and other fields of sensory neuroscience including tactile perception from Dr. Shigeru Kitazawa. I learned how beautiful our human brain structure is from Dr. Karl Zilles.

I thank all of my prior and current colleagues of my lab and CiNet, especially: Dr. Masamichi Hayashi, Dr. Tomoya Kawashima, Dr. Nobuhiro Hagura, Dr. Ai Koizumi, Dr. Kenichi Yuasa, Dr. Sorato Minami, Alexander Vostriakov, Shuka Shibusawa, and Ikko Kimura chatted with me about scientific topics and daily things.

Finally, I thank my old friends and family for a lot of support.

Chapter 7.

Achievements

7.1 Related to this dissertation

Peer-REVIEW JOURNAL ARTICLES

Oishi, H., Takemura, H., Aoki, SC., Fujita, I., Amano, K. Microstructural properties of the vertical occipital fasciculus explain the variability in human stereoacuity. *Proceedings of National Academy of Sciences of the United States of America*, National Academy of Sciences, 115 (48), 12289-12294, 2018.

International conferences

Oral presentation

Oishi, H., Takemura, H., Aoki, SC., Fujita, I., Amano, K. Human white matter structural properties correlate with individual difference in stereoacuity. Vision Sciences Society Annual Meeting, Journal of Vision August 2017 Vol.17 759, St. Peet Beach, USA. (2017, May)

Poster presentation

Oishi, H., Takemura, H., Aoki, SC., Fujita, I., Amano, K. Diffusion properties of human visual white matter correlate with stereoacuity. Society for Neuroscience Annual Meeting, 796.11, San Diego, USA. (2016, November)

Oishi, H., Takemura, H., Amano, K. Using macromolecular tissue volume mapping to identify subdivisions in human lateral geniculate nucleus. Asia-Pacific Conference on Vision, PR0067, Ibaraki, Japan. (2019, July)

Oishi, H., Takemura, H., Amano, K. Using quantitative MRI to identify the magnocellular and parvocellular subdivisions in the human lateral geniculate nucleus. Society for Neuroscience Annual Meeting, 577.11, Chicago, USA. (2019, October)

Domestic conferences

Oral presentation

大石浩輝, 竹村浩昌, 青木俊太郎, 藤田一郎, 天野薫. ヒト立体視力の個人差と白質線維構造の関係. 日本視覚学会 2017 年冬季大会, 2o02, 東京. (2017, 1月)

大石浩輝, 竹村浩昌, 天野薫. 定量的MRIを用いたヒト外側膝状体の大細胞層と小細胞層の同定. 日本視覚学会2020年冬季大会, 1o01, 東京. (2020, 1月)

Poster presentation

大石浩輝, 竹村浩昌, 青木俊太郎, 藤田一郎, 天野薫. 両眼立体視機能の個人差と白質線維構造の関係. 第39回日本神経科学大会, P1-133, 横浜. (2016, 7月)

大石浩輝, 竹村浩昌, 青木俊太郎, 藤田一郎, 天野薫. ヒト立体視力とVertical Occipital Fasciculusの組織構造の関連. 第1回ヒト脳イメージング研究会, P5, 東京. (2017, 9月)

大石浩輝, 竹村浩昌, 青木俊太郎, 藤田一郎, 天野薫. Vertical Occipital Fasciculusの微小構造特性がヒト立体視力の個人差を説明する. 第41回日本神経科学大会, 1P-168, 神戸. (2018, 7月)

大石浩輝, 竹村浩昌, 天野薫. A parcellation method of human lateral geniculate nucleus subdivisions using structural MRI. 第3回ヒト脳イメージング研究会, P35, 神戸. (2019, 9月)

AWARDS

奨励賞, 第1回ヒト脳イメージング研究会. (2017, 9月)

若手奨励賞, 第9回脳情報通信融合研究センター全体会議. (2019, 11月)

ベストプレゼンテーション賞, 日本視覚学会2020年冬季大会. (2020, 1月)

7.2 Other achievements

Peer-REVIEW JOURNAL ARTICLES

Minami, S., Oishi, H., Takemura, H., Amano, K. Inter-individual differences in occipital alpha oscillations correlate with white matter tissue properties of the optic radiation. *eNeuro*, Society for Neuroscience, 7(2), 0224-19.2020, 2020.

International conferences

Poster presentation

Minami, S., Oishi, H., Takemura, H., Amano, K. Functional roles of alpha oscillations underlying the communication between dorsal and ventral visual areas. Vision Sciences Society Annual Meeting, Journal of Vision August 2017 Vol.17 1138, St. Peet Beach, USA. (2017, May)

I contributed to the design, investigation, analysis and writing in all of the achievements.